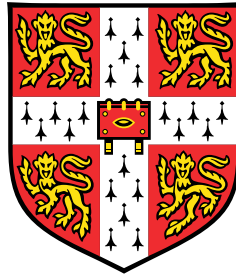


Control of the buffer and logarithmic layers in wall-bounded turbulent flows



Joseph I. Ibrahim

Department of Engineering
University of Cambridge

This thesis is submitted for the degree of
Doctor of Philosophy

Declaration

This thesis is the result of my own work and includes nothing which is the outcome of work done in collaboration except as declared in the Preface and specified in the text. I further state that no substantial part of my thesis has already been submitted, or, is being concurrently submitted for any such degree, diploma or other qualification at the University of Cambridge or any other University or similar institution except as declared in the Preface and specified in the text. It does not exceed the prescribed word limit for the relevant Degree Committee.

Joseph I. Ibrahim
August 2021

Acknowledgements

First and foremost, I would like to express my sincere gratitude to my supervisor, Dr Ricardo García-Mayoral, for his support and guidance throughout my PhD. I have learnt so much under his supervision, not only about fluid mechanics, and it has been a pleasure to be part of his research group over the last four years.

I am also grateful to Prof Daniel Chung and Dr Anna Guseva for discussions on various aspects of this thesis, and to Dr Yongyun Hwang for his support during my undergraduate degree at Imperial College London and beyond.

I would like to thank everyone in the Fluids Group Office, past and present, for the countless (sometimes endless) coffee breaks, and for always helping me when I needed it. I feel lucky to have shared this experience with you all, virtually or otherwise. In particular, I would like to mention the members of Ricardo's research group, Chris, Nabil, Akshath, Garazi, Wenxiong, Dharma, Ziyin, Mel, Zishen, Ruta and Zengrong, as well as the other 'usual suspects', Kshitij, Andrea, Pascal, Alex, Ignacio, Connor, Rhys, Tom, Jamie and Alice.

I would also like to thank my parents, Hassan and Louise, and my sister, Ameerah, for always supporting and encouraging me unconditionally in all my endeavours. I would not be here without them.

A special mention must go to my partner, Sophie, for her unwavering love, support and resolve over the last four years, during which we spent many days and weeks apart. I would not have finished this thesis without her.

Finally, I would like to acknowledge the Engineering and Physical Sciences Research Council for their financial support under a Doctoral Training Account, grant number EP/M506485/1. This work was also partly supported by the European Research Council through the 2nd Coturb Madrid Summer Workshop. Computational resources were provided by the 'Cambridge Service for Data Driven Discovery' operated by the University of Cambridge Research Computing Service and funded by EPSRC Tier-2 grant EP/P020259/1, and by the DECI resource Cartesius, based in the Netherlands at SURFSara, with support from PRACE.

Abstract

This thesis studies the effect of controlling separately the buffer and logarithmic layers in wall-bounded turbulent flows.

In the case of buffer-layer control, we examine the effect on near-wall turbulence of displacing the apparent, virtual origins perceived by different components of the overlying flow. This mechanism is commonly reported for drag-altering textured surfaces of small size. For the particular case of riblets, it has been proposed that their effect on the overlying flow could be reduced to an offset between the origins perceived by the streamwise and spanwise velocities, with the latter being the origin perceived by turbulence. Later results, particularly in the context of superhydrophobic surfaces, suggest that this effect is not determined by the apparent origins of the tangential velocities alone, but also by the one for the wall-normal velocity. To investigate this, we conduct direct simulations of turbulent channels imposing different virtual origins for all three velocity components using Robin, slip-like boundary conditions. The results of our simulations support the idea that the relevant parameter is the offset between the virtual origins perceived by the mean flow and turbulence. When using Robin, slip-like boundary conditions, the virtual origin for the mean flow is determined by the streamwise slip length. Meanwhile, the virtual origin for turbulence results from the combined effect of the wall-normal and spanwise slip lengths. The slip experienced by the streamwise velocity fluctuations, in turn, has a negligible effect on the virtual origin for turbulence, and hence the drag, at least in the regime of drag reduction. This suggests that the origin perceived by the quasi-streamwise vortices, which induce the cross-flow velocities at the surface, is key in determining the virtual origin for turbulence, while that perceived by the near-wall streaks, which are associated with the streamwise velocity fluctuations, plays a secondary role. In this framework, the changes in turbulent quantities typically reported in the flow-control literature are shown to be merely a result of the choice of origin, and are absent when using as origin the one experienced by turbulence. Other than this shift in origin, we demonstrate that turbulence thus remains essentially smooth-wall-like. A simple expression can predict the virtual origin for turbulence in this regime. The effect can also be reproduced a priori by introducing the virtual origins into a smooth-wall eddy-viscosity framework. We also present exploratory results that suggest that the effect on the flow of opposition control, an active flow-control technique, can also be interpreted in terms of virtual origins.

In the second part of this thesis, we investigate the effect of controlling the flow within the logarithmic layer alone, without directly modifying the flow elsewhere, and assess how this effect varies with Reynolds number. In contrast to buffer-layer control strategies, controlling the logarithmic layer has the potential to provide a reduction in turbulent drag that does not diminish with increasing Reynolds number. We first consider the effect of an idealised, hypothetical control strategy that is able to remove all of the Reynolds shear stress in all or part of the logarithmic layer, while leaving the rest of the flow unaltered. The idea is that this would serve as a theoretical prediction for the maximum turbulent drag reduction achievable by strategies that target the logarithmic layer alone. We quantify the effect of this control strategy on the flow and find that by relaminarising the whole logarithmic layer or a fixed portion of it in outer units, it is theoretically possible to produce a reduction in drag that improves with increasing Reynolds number. We also conduct a series of direct numerical simulations of turbulent channel flows at friction Reynolds numbers in the range $360 \lesssim Re_\tau \lesssim 2000$, and artificially remove certain streamwise and spanwise wavelengths of the wall-normal velocity across a range of heights primarily within the logarithmic layer. The aim is to inhibit the dynamics of the self-similar, wall-attached sweep and ejection motions and their associated vortex clusters that reside in the logarithmic layer, while modifying the near-wall dynamics as little as possible. When these wavelengths are removed, we observe a positive, outward shift in the mean velocity profile, due to a local reduction in Reynolds shear stress, and subsequent increase in viscous stress, within the controlled region. When a fixed proportion of the uncontrolled Reynolds shear stress is removed across the whole logarithmic layer in our simulations, we show that it is possible to generate a reduction in drag that improves with Reynolds number, although the idealised control strategy grossly over-predicts the actual performance. This occurs because the majority of the energy originally contained in the removed scales in the control region is redistributed to even larger scales, rather than eradicated. This suggests that the flow in the logarithmic layer is very robust, even to this kind of targeted control strategy. Therefore, even though controlling the logarithmic layer has significant potential in theory, our results suggest that actual performance may be limited.

Table of contents

| | |
|--|-----------|
| Nomenclature | xi |
| 1 Introduction | 1 |
| 1.1 The buffer layer | 3 |
| 1.2 Surface texture, drag and virtual origins | 4 |
| 1.2.1 The change in drag due to surface texture | 5 |
| 1.2.2 Virtual origins and ΔU^+ | 7 |
| 1.2.3 Opposition control and virtual origins | 11 |
| 1.3 The logarithmic layer | 11 |
| 1.3.1 Variation of the mean velocity profile and logarithmic layer with Re_τ . . | 12 |
| 1.3.2 Self-similar, attached eddies in wall-bounded turbulence | 14 |
| 1.4 Objectives | 19 |
| 1.5 Organisation of the thesis | 21 |
| 2 Numerical methods | 23 |
| 2.1 DNS of turbulent channel flows | 23 |
| 2.2 Robin, slip-length-like boundary conditions | 24 |
| 2.3 Opposition control | 27 |
| 2.4 Artificially removing length scales from the wall-normal velocity | 28 |
| 3 A unifying virtual-origin framework for turbulence over drag-altering surfaces | 31 |
| 3.1 The origin for turbulence | 31 |
| 3.2 Separating the effects of the virtual origins for the mean flow and the fluctuations | 40 |
| 3.3 Predicting the origin for turbulence | 43 |
| 3.4 Scaling with Reynolds number and domain size | 46 |
| 3.5 Departure from smooth-wall-like turbulence | 47 |
| 3.6 Active opposition control interpreted in a virtual-origin framework | 52 |
| 3.7 An eddy-viscosity model | 55 |

| | | |
|----------|---|------------|
| 4 | An idealised logarithmic-layer control strategy: theoretical predictions | 61 |
| 4.1 | Relaminarising the logarithmic layer | 61 |
| 4.2 | Effect of Reynolds number | 64 |
| 4.3 | Effect of removing only some of the Reynolds shear stress | 68 |
| 4.4 | Summary | 69 |
| 5 | Selective control of the logarithmic layer: results from DNS | 71 |
| 5.1 | Simulations with block forcing | 72 |
| 5.1.1 | Effect of the control on the mean velocity and turbulence | 74 |
| 5.1.2 | Comparison of cases at different Re_τ | 85 |
| 5.2 | Simulations with hierarchical forcing | 88 |
| 5.2.1 | Effect of Reynolds number and comparison to theoretical predictions | 96 |
| 5.3 | Robustness of the logarithmic layer to the control | 100 |
| 6 | Conclusions and outlook | 107 |
| | References | 113 |
| | Appendix A Additional results | 119 |
| A.1 | Results of Choi et al. (1994) interpreted in the virtual-origin framework | 119 |

Nomenclature

Roman Symbols

| | |
|-------------|---|
| A | y -intercept of the log law |
| A_d | damping coefficient in the definition of the eddy viscosity, ν_T^+ (3.9) |
| B | function containing the y -intercept and wake function of the log law |
| c_f | skin friction coefficient |
| c_i | coefficients used to define the limits of the control region, $i = 1, 2, 3, 4$ |
| d | diameter of buffer-layer vortices |
| DR | drag reduction |
| E_{uu} | spectrum of u^2 in (k_x, k_z) space |
| E_{uv} | spectrum of uv in (k_x, k_z) space |
| E_{vv} | spectrum of v^2 in (k_x, k_z) space |
| E_{ww} | spectrum of w^2 in (k_x, k_z) space |
| f | viscous shear stress in the eddy-viscosity model, defined by (3.8) |
| h | height of roughness elements |
| k_x | streamwise Fourier wavenumber |
| $k_{x,l}$ | wavenumbers of streamwise scales with $\lambda_x/\delta \geq 1$, see (5.3) |
| k_z | spanwise Fourier wavenumber |
| $k_{z,l}$ | wavenumbers of spanwise scales with $\lambda_z/\delta \geq 1$, see (5.3) |
| L | characteristic texture length scale |
| ℓ_{sm} | intermediate variable for finding ℓ_v from ℓ_y , due to curvature of v'^+ profile |

| | |
|--------------------|--|
| ℓ_T | depth of the virtual origin perceived by turbulence |
| $\ell_{T,pred}$ | predicted depth of the virtual origin perceived by turbulence, from (3.6) |
| ℓ_U | depth of the virtual origin perceived by the mean flow |
| ℓ_u | depth of the virtual origin perceived by the streamwise velocity |
| ℓ_v | depth of the virtual origin perceived by the wall-normal velocity |
| ℓ_w | depth of the virtual origin perceived by the spanwise velocity |
| $\ell_{w,eff}$ | depth of effective virtual origin perceived by w , in the absence of transpiration |
| ℓ_x | streamwise slip length |
| $\ell_{x,m}$ | slip length applied to the mean flow |
| ℓ_y | wall-normal ‘slip length’ |
| ℓ_z | spanwise slip length |
| $\ell_{z,eff}$ | effective spanwise slip length |
| L_x | streamwise domain size |
| L_y | wall-normal domain size |
| L_z | spanwise domain size |
| p | kinematic pressure |
| Re | bulk Reynolds number |
| Re_τ | friction Reynolds number, equivalent to the flow thickness expressed in wall units |
| t | time |
| T_E | largest-eddy turnover time |
| t_s | time-window over which statistics are collected |
| \mathcal{T}_{uv} | integral of uncontrolled Reynolds shear stress, defined by (4.3) |
| \mathbf{u} | velocity vector, with components u , v and w |
| U | mean streamwise velocity |
| u | streamwise velocity |

| | |
|--------------|---|
| U_b | bulk velocity |
| U_c | controlled mean velocity profile |
| U_δ | reference velocity, e.g. free-stream, centreline or bulk velocity |
| U_{log} | mean velocity profile in the logarithmic layer, as defined by the logarithmic law (1.9) |
| U_p | parabolic, laminar mean velocity profile in control region |
| U_r | mean velocity profile above a textured wall, from eddy-viscosity model |
| U_s | streamwise slip velocity |
| U_{sm} | smooth-wall mean profile from eddy-viscosity model |
| u_τ | friction velocity |
| $u_{\tau,0}$ | friction velocity measured with respect to the plane $y = 0$ |
| v | wall-normal velocity |
| w | spanwise velocity |
| x | streamwise coordinate |
| y | wall-normal coordinate, distance from the wall |
| y_c | mid-height of logarithmic-layer vortex cluster |
| y_d | detection plane for opposition control |
| y_f | forcing region |
| $y_{f,max}$ | maximum height of forcing region |
| $y'_{f,max}$ | maximum height of ‘extended’ forcing region, see (5.2) |
| $y_{f,min}$ | minimum height of forcing region |
| $y'_{f,min}$ | minimum height of ‘extended’ forcing region, see (5.2) |
| y_{max} | maximum height of control region |
| y_{min} | minimum height of control region |
| y_t | target height of self-similar vortex clusters |
| z | spanwise coordinate |

Greek Symbols

| | |
|-------------------|--|
| α_k | Runge–Kutta coefficient, $k = 1, 2, 3$ |
| β_k | Runge–Kutta coefficient, $k = 1, 2, 3$ |
| Δ | change with respect to reference value |
| δ | flow thickness, e.g. channel half-height, boundary layer thickness, pipe radius, etc. |
| ΔE_{uv} | difference between the energy contained in a given mode (k_x, k_z) in the controlled and uncontrolled flows, see (5.3) |
| Δt | time step |
| ΔU | shift of the mean velocity profile, relative to the uncontrolled (smooth-wall) flow |
| ΔU_p | difference between controlled, parabolic mean velocity profile and the uncontrolled one |
| Δx | streamwise grid resolution |
| Δy_{min} | minimum wall-normal grid resolution, due to the grid stretching |
| Δy_{max} | maximum wall-normal grid resolution, due to the grid stretching |
| Δy_f | thickness of forcing region |
| $\Delta y'_f$ | thickness of ‘extended’ forcing region, see (5.2) |
| Δy_{log} | thickness of the logarithmic layer |
| Δz | spanwise grid resolution |
| ϵ | wall-normal shift of eddy viscosity with respect to $y = 0$ |
| γ_k | Runge–Kutta coefficient, $k = 1, 2, 3$ |
| κ | the von Kármán constant |
| λ_x | wavelength of streamwise Fourier mode |
| $\lambda_{x,max}$ | largest removed streamwise wavelength |
| $\lambda_{x,min}$ | smallest removed streamwise wavelength |
| $\lambda_{x,t}$ | target streamwise length scale or wavelength |
| λ_z | wavelength of spanwise Fourier mode |
| $\lambda_{z,max}$ | largest removed spanwise wavelength |

| | |
|-------------------|---|
| $\lambda_{z,min}$ | smallest removed spanwise wavelength |
| $\lambda_{z,t}$ | target spanwise length scale or wavelength |
| ν | kinematic viscosity |
| ν_T | eddy viscosity |
| ϕ | proportion of Reynolds shear stress targeted by control strategy |
| ϕ_c | average, relative proportion of Reynolds shear stress removed in the forcing region, defined by (5.1) |
| ϕ'_c | alternative measure of the average, relative proportion of Reynolds shear stress removed by the control, defined by (5.2) |
| ϕ_l | proportion of the uncontrolled Reynolds shear stress contained in large length scales with $\lambda_x/\delta, \lambda_z/\delta \geq 1$, defined by (5.3) |
| Φ_{uv} | premultiplied spectrum of uv , $-k_x k_z E_{uv}(k_x, k_z)$ |
| ρ | density |
| τ | total fluid stress |
| τ_w | wall shear stress |
| ξ | integration variable (surrogate for y) |

Superscripts

| | |
|----------------------|---|
| $(\cdot)^+$ | wall units or viscous units |
| $(\hat{\cdot})$ | variable in Fourier space |
| $(\overline{\cdot})$ | variable averaged in time and in the homogeneous (wall-parallel) directions |
| $(\cdot)'$ | fluctuating component |

Subscripts

| | |
|------------------|---|
| $(\cdot)_0$ | reference smooth-wall or uncontrolled value |
| $(\cdot)_\delta$ | variable evaluated at the channel centre, boundary layer edge, etc. |

Acronyms / Abbreviations

| | |
|-----|---|
| B | in block-forcing simulation names, indicates forcing across a band of wall-normal heights |
| CFL | Courant–Friedrichs–Lewy number |

| | |
|--------|--|
| D | in virtual-origin simulation case names, signifies larger wall-parallel domain size |
| DNS | direct numerical simulation |
| H | in virtual-origin simulation case names, signifies higher Reynolds number |
| L | in hierarchical-forcing simulation names, denotes forcing across the whole logarithmic layer |
| L | in virtual-origin simulation case names, signifies large slip lengths |
| min | minimum |
| M | in virtual-origin simulation case names, signifies $\ell_x \neq \ell_{x,m}$ |
| O | in hierarchical-forcing simulation names, denotes forcing region consistent with case L550-30 in outer units |
| P | in block-forcing simulation names, denotes forcing at one plane only |
| r.m.s. | root mean square |
| U | in virtual-origin simulation case names, denotes $\ell_x > 0$ |
| V | in virtual-origin simulation case names, denotes $\ell_y > 0$ |
| W | in block-forcing simulation names, indicates forcing extends down to the wall |
| W | in virtual-origin simulation case names, denotes $\ell_z > 0$ |

Chapter 1

Introduction

The control of wall-bounded turbulent flows, which are prevalent in many engineering applications, has been the subject of a great deal of research over the past few decades. Strategies that aim to reduce turbulent skin-friction drag have been of particular interest, since it can account for up to 50% of the total drag of a typical airliner (Spalart and McLean, 2011). To date, the focus has been predominantly on techniques that aim to control the near-wall turbulence cycle within the buffer layer, due to its key role in the generation of turbulent skin friction (Orlandi and Jiménez, 1994; Hamilton et al., 1995; Waleffe, 1997; Jiménez and Pinelli, 1999). A popular method is the use of surface texturing to manipulate the flow and modify the turbulent skin-friction drag compared to a smooth surface (see e.g. García-Mayoral et al., 2019). Examples of these kinds of surfaces include riblets (Walsh and Lindemann, 1984), superhydrophobic surfaces (Rothstein, 2010) and anisotropic permeable substrates (Gómez-de-Segura and García-Mayoral, 2019). In their pioneering work, Luchini et al. (1991) and Luchini (1996) proposed that when the texture size is small, i.e. smaller than the overlying near-wall turbulent eddies, the effect of the texture on the flow can be reduced to an offset between the virtual origins perceived by the mean flow and turbulence.¹ The general idea is that the texture ‘pushes’ the turbulent eddies away from the wall with respect to the mean flow (Jiménez, 1994; Luchini, 1996), which reduces the local turbulent mixing of streamwise momentum and, therefore, the skin-friction drag (Orlandi and Jiménez, 1994).

Luchini (1996) postulated that the dynamics of turbulence would be displaced ‘rigidly’ by the texture, and therefore would be unaltered compared to the flow over smooth wall. However, it has often been reported in the literature that the structure and dynamics of turbulence are somehow modified by the presence of small-scale surface texture. This has been discussed in studies on riblets (see e.g. Choi et al., 1993; Chu and Karniadakis, 1993; El-Samni et al., 2007) and also superhydrophobic surfaces (see e.g. Min and Kim, 2004; Busse and Sandham, 2012; Park et al., 2013; Jelly et al., 2014). The results of these studies seem to suggest that

¹The concept of virtual origins will be explained in detail section 1.2.2, but a virtual origin can be described as the depth at which a given component of the flow perceives an apparent, no-slip wall.

turbulence is no longer as it would be over a smooth wall, which would be at odds with the ideas posed by [Luchini \(1996\)](#).

One of the aims of this thesis is to consolidate these seemingly contradictory ideas, by investigating the effect of displacing the virtual origins perceived by different components of the flow. It was originally suggested that the virtual origin perceived by turbulence would be equivalent to the virtual origin perceived by the spanwise velocity ([Luchini et al., 1991](#); [Jiménez, 1994](#)). However, recent results suggest that it is also necessary to consider a virtual origin for the wall-normal velocity to fully describe the effect of the texture on the flow ([Gómez-de-Segura et al., 2018a](#); [Gómez-de-Segura and García-Mayoral, 2020](#)). To this end, we aim to develop a unifying virtual-origin framework in which the effect of the surface texture or flow-control strategy can be reduced to a relative offset between the virtual origins perceived by different components of the flow, and determine which components those would be. This effect has been observed in direct numerical simulations (DNSs) of certain textured surfaces ([Gómez-de-Segura et al., 2018b](#)), and also in DNSs with active opposition control ([Choi et al., 1994](#)). Within this virtual-origin framework, we also aim to assess to what extent the dynamics of turbulence remain the same as over smooth walls, as originally proposed by [Luchini \(1996\)](#).

Beyond the study of virtual origins, this thesis will also investigate methods for controlling the logarithmic layer. The motivation for this is that buffer-layer control strategies, like the use of surface texturing, produce a change in the flow that scales in wall (or viscous) units. The thickness of the buffer layer is fixed in wall units, but in outer units diminishes with increasing Reynolds number. Therefore, the drag reduction generated by buffer-layer control strategies typically degrades logarithmically with increasing Reynolds number ([Spalart and McLean, 2011](#); [García-Mayoral et al., 2019](#)). As a result, control strategies that show promise when tested at modest Reynolds numbers in experiments and direct simulations can become considerably less effective at the high Reynolds numbers of applications.

This has led to a growing research interest in control techniques that manipulate the larger scales of the flow, whose characteristic size scales in outer units, rather than in wall units. It might then be possible to produce a reduction in drag that does not degrade with increasing Reynolds number. One option is to target the flow in the logarithmic layer, since the size of the eddies in this region is known to scale essentially with distance from the wall.² As discussed by [Jiménez \(2018\)](#), at Reynolds numbers of industrial relevance, a significant proportion of the turbulent dissipation takes place in the logarithmic layer of the flow, which could make controlling it worthwhile. It has been shown experimentally that it is possible to reduce the skin-friction drag in a turbulent boundary layer by targeting the large-scale motions in the logarithmic layer with wall-normal jets that originate from the wall ([Abbassi et al., 2017](#); [Ruan et al., 2018, 2019](#)). While control strategies of this kind show promise, they are particularly intrusive to the flow below the logarithmic layer and thus can significantly modify the flow in the

²The structure of the flow in the logarithmic layer will be discussed in more detail in section 1.3.2.

buffer layer. This makes it difficult to separate the effect on drag of controlling the logarithmic layer from the effect caused by changes in the underlying flow. In light of this, we investigate the effect of controlling the flow within the logarithmic layer only, without directly modifying the flow elsewhere, and consider how this effect might change as the Reynolds number varies. Ultimately, we hope to gain a better understanding of the potential drag reduction achievable by manipulating the flow in the logarithmic layer only, which could have implications for the design of future control strategies.

Throughout this thesis, we use x , y and z as the streamwise, wall-normal and spanwise coordinates, respectively, and u , v and w as their corresponding velocity components. We also use δ to refer to the flow thickness, which, depending on the application, would correspond to the channel half-height, boundary layer thickness or pipe radius. The superscript ‘+’ indicates scaling in wall units, i.e. normalisation by the friction velocity $u_\tau = \sqrt{\tau_w/\rho}$ and the kinematic viscosity ν , where τ_w is the wall shear stress and ρ is the density. The friction Reynolds number is equivalent to the flow thickness expressed in wall units, $Re_\tau = \delta^+$. Physically, this represents the separation of scales between the size of the smallest eddies in the flow, $\mathcal{O}(\nu/u_\tau)$, and the size of the largest ones, $\mathcal{O}(\delta)$.

The remainder of this chapter is organised as follows. In section 1.1, we briefly review the structure and dynamics of the flow in the buffer layer. In section 1.2, we present and discuss the current understanding of how small-textured surfaces modify the drag compared to a smooth surface by imposing virtual origins on the flow velocity components. Section 1.3 provides context for the investigation on logarithmic-layer control: we first consider the variation of the mean velocity profile and logarithmic layer with Reynolds number; then we discuss the structure of the flow in logarithmic layer, focussing on the concept of attached eddies. In section 1.4, we define the specific aims and objectives of the thesis. Finally, we summarise the content of the remaining chapters in section 1.5.

1.1 The buffer layer

Before discussing the effect of small-surface texture on the flow, we first review the nature of the flow within the buffer layer, which is typically defined as $y^+ \lesssim 80$. In the buffer layer, velocities scale with u_τ and lengths scale with the viscous length scale ν/u_τ . The layer very close to the wall, $y^+ \lesssim 5$, is often referred to as the viscous sublayer, where the viscous stress dominates. Above the viscous sublayer, $5 \lesssim y^+ \lesssim 80$, both the viscous and Reynolds stresses are important. The structure and dynamics of the buffer layer is relatively well understood. The flow is dominated by coherent structures that take the form of streaks and quasi-streamwise vortices (Kline et al., 1967; Cantwell, 1981; Smith and Metzler, 1983; Kim et al., 1987; Robinson, 1991). The streaks are long streamwise structures of high- and low-speed fluid that are flanked by pairs of counter-rotating quasi-streamwise vortices, as sketched in figure 1.1. The streaks are of order $x^+ \approx 1000$ long (Blackwelder and Eckelmann, 1979), and streaks of the same sign have

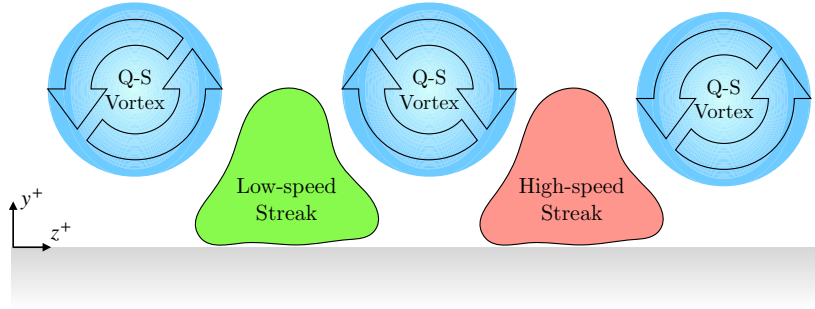


Figure 1.1 Schematic of the streak and quasi-streamwise (Q-S) vortices of the buffer-layer cycle. The shaded grey region indicates the wall. Adapted from [Gómez-de-Segura \(2019\)](#).

an average spanwise spacing of $z^+ \approx 100$ ([Kline et al., 1967](#); [Kim et al., 1971](#)). The vortices have a diameter of $d^+ \approx 15$ ([Blackwelder and Eckelmann, 1979](#)), and the spanwise spacing between vortices of the same sign is also $z^+ \approx 100$ ([Kim et al., 1971](#)). Each vortex resides in the near-wall region for a streamwise distance $x^+ \approx 200$, but there are several vortices associated with each streak ([Jeong et al., 1997](#)). As discussed by [Jiménez \(2013\)](#), the streaks contain most of the turbulent kinetic energy, while the vortices organise both the dissipation and Reynolds stress in the buffer layer. Since the approximate size of the streaks and vortices is comparable, $\mathcal{O}(100\nu/u_\tau)$, we can conclude that there is effectively no separation of scales between energy and dissipation in the buffer layer. This is contrast to the flow in logarithmic region, which will be discussed in section 1.3.

The buffer-layer structures interact in a process that has been dubbed the ‘regeneration mechanism’ ([Hamilton et al., 1995](#)) or the ‘self-sustaining process’ ([Waleffe, 1997](#)), since it occurs independently of the flow in the outer region of the flow ([Jiménez and Moin, 1991](#)). In simple terms, the quasi-streamwise vortices generate the streaks by bringing higher momentum fluid closer to the wall (sweeps) and pushing lower momentum fluid away from it (ejections). The vortices themselves are formed by an instability of the streaks, which eventually breakdown, and the cycle starts again ([Jiménez and Pinelli, 1999](#); [Schoppa and Hussain, 2002](#)). While this process can exist independently of the dynamics in the outer regions of the flow, it should be noted that the near-wall flow is modulated by the presence of the large-scale motions in the logarithmic layer and above ([Hutchins and Marusic, 2007](#)).

1.2 Surface texture, drag and virtual origins

We mentioned above the idea that the effect of small-scale surface texture can be reduced to an offset between the virtual origins perceived by different components of the flow. In this section, we discuss this concept in detail, but first we summarise the general effect of the texture on the mean velocity profile and the drag.

1.2.1 The change in drag due to surface texture

Provided that the direct effect of the texture is confined to the near-wall region, the classical theory of wall turbulence postulates that the change in drag is manifested as a constant shift in the mean velocity profile, ΔU^+ , experienced by the flow above the near-wall region (Clauser, 1956; Spalart and McLean, 2011; García-Mayoral et al., 2019). In this thesis, we choose $\Delta U^+ > 0$ to denote drag reduction. However, we note that in the roughness community, the sign is typically reversed and ΔU^+ , referred to as the roughness function, is positive when drag increases (Jiménez, 2004). When a surface produces such a shift in the mean velocity profile, in the logarithmic and outer regions of the flow, we would have (Clauser, 1956)

$$U^+ = \frac{1}{\kappa} \log y^+ + B + \Delta U^+, \quad (1.1)$$

where U is the mean streamwise velocity and y is the distance from the wall. The von Kármán constant, κ , remains unchanged, and so does the function B , which contains both the y -intercept of the log law and the wake function. An example mean velocity profile for a drag-reducing, small-textured surface with $\Delta U^+ \approx 1.4$ is shown in figure 1.2 for reference. If the texture size remains constant in wall units and the effect of the texture is confined to the near-wall region, the consensus is that ΔU^+ is essentially independent of the friction Reynolds number, as discussed by García-Mayoral and Jiménez (2011a) and Spalart and McLean (2011) in the context of riblets. The shift ΔU^+ produced by some other flow-control strategies, such as spanwise wall oscillation, has also been reported to be essentially independent of the Reynolds number, so long as the parameters that describe the control remain constant in wall units (Gatti and Quadrio, 2016). However, regardless of the control strategy, ΔU^+ is weakly affected by the modulation of the local viscous length scale by the intensity of the large scales in the flow, an effect that becomes more significant at larger Reynolds numbers (Mathis et al., 2009; Zhang and Chernyshenko, 2016). This effect is typically of the order of a few per cent at the Reynolds numbers of engineering applications (Hutchins, 2015; Chernyshenko and Zhang, 2019), so we will neglect it here.

In turn, the change in drag is strictly dependent on the Reynolds number. The skin friction coefficient can be defined as

$$c_f = \frac{2\tau_w}{\rho U_\delta^2} = \frac{2}{U_\delta^{+2}}, \quad (1.2)$$

where U_δ is the reference velocity. The choice of U_δ depends on the type of flow considered. Typically for external flows, U_δ would be the free-stream velocity, while for internal flows it would be the bulk velocity. For internal flows, U_δ can also be the centreline velocity, for comparison with external flows of interest (García-Mayoral and Jiménez, 2011b). Using the subscript ‘0’ to denote reference smooth-wall values, the drag reduction, DR , can then be

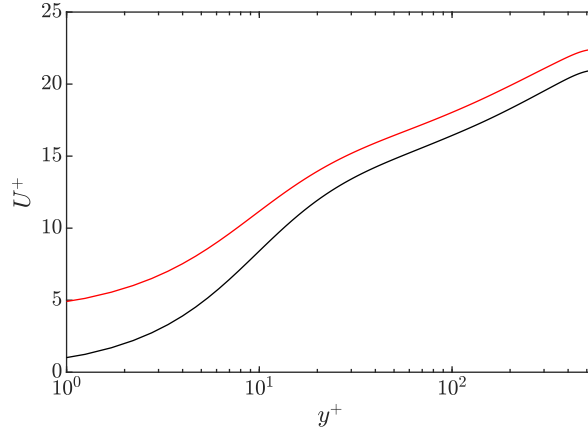


Figure 1.2 Example mean velocity profile for a drag-reducing, small-textured surface (red line), compared to reference smooth-wall profile (black line). $Re_\tau = 550$. $\Delta U^+ \approx 1.4$ in the logarithmic layer and above, $y^+ \gtrsim 80$.

expressed as the relative decrease in c_f compared to that for a smooth wall, c_{f_0} ,

$$DR = -\frac{\Delta c_f}{c_{f_0}}, \quad (1.3)$$

where $\Delta c_f = c_f - c_{f_0}$. As discussed by [García-Mayoral et al. \(2019\)](#), care must be taken when quoting values of drag reduction achieved by textured surfaces. For example, the corresponding position of the reference smooth wall, particularly in the case of internal flows, can imply a potentially significant change in the hydraulic radius between experiments and applications, resulting in values of DR not directly attributable to the texture.

From (1.3) and the definition of c_f (1.2), DR can be given in terms of ΔU^+ as follows. Provided the Reynolds number is large enough that outer-layer similarity is observed and (1.1) holds, it follows from (1.1) that $U_\delta^+ = U_{\delta_0}^+ + \Delta U^+$, which is strictly valid so long as Re_τ remains fixed. Then (1.3) can be written as ([García-Mayoral et al., 2019](#))

$$DR = 1 - \left(\frac{1}{1 + \Delta U^+ / U_{\delta_0}^+} \right)^2. \quad (1.4)$$

Since $U_{\delta_0}^+$ depends on the Reynolds number, so too will the drag, for ΔU^+ fixed. This leaves ΔU^+ as the only Reynolds-number independent means of quantifying the change in drag and extrapolating laboratory results to applications ([Spalart and McLean, 2011](#); [García-Mayoral et al., 2019](#)). Figure 1.3 portrays the variation of DR with Re_τ for fixed ΔU^+ , where we see that DR degrades as Re_τ increases. The figure demonstrates that buffer-layer control techniques that show promise at low Reynolds numbers in experiments and simulations ($Re_\tau \gtrsim 10^2$) can be considerably less effective at the high Reynolds numbers of industrial relevance ($Re_\tau \gtrsim 10^4$), as mentioned above.

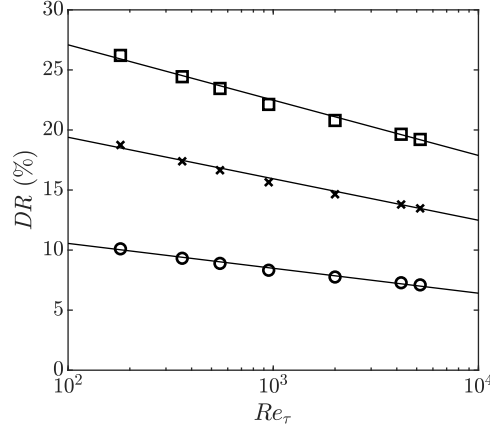


Figure 1.3 Degradation of DR with Re_τ for fixed ΔU^+ , as defined by (1.4). Circles, $\Delta U^+ = 1$; crosses, $\Delta U^+ = 2$; squares, $\Delta U^+ = 3$. The black lines denote the approximate logarithmic fit to the data points in each case. Here, the reference velocity, $U_{\delta_0}^+$, is the channel centreline velocity, taken from direct numerical simulations of turbulent channels. The centreline velocities at $Re_\tau = 4200$ and 5200 are from [Lozano-Durán and Jiménez \(2014\)](#) and [Lee and Moser \(2015\)](#), respectively. The centreline velocities for the lower Reynolds numbers are from the present study. Adapted from [García-Mayoral et al. \(2019\)](#).

1.2.2 Virtual origins and ΔU^+

We now discuss the way in which surfaces with small texture produce a shift in the mean velocity profile, ΔU^+ , and hence modify the drag. The early studies focused on the drag reduction mechanism in riblets, but the analysis can easily be extended to other surfaces. [Bechert and Bartenwerfer \(1989\)](#) originally suggested that, for riblets, the streamwise velocity experiences an apparent, no-slip wall, or virtual origin, at a depth ℓ_x below the riblet tips, which they called the ‘protrusion height’. This concept is depicted in figure 1.4(a). Note that, in the superhydrophobic-surface community, ℓ_x is often referred to as the streamwise slip length, and, in this thesis, we will use the term ‘slip length’ instead of ‘protrusion height’. Defining for convenience the reference plane $y = 0$ to be located at the riblet tips, and noting that the velocity profile is essentially linear in the viscous sublayer, this is equivalent to a Navier slip condition at $y = 0$ of the form

$$u = \ell_x \frac{\partial u}{\partial y}. \quad (1.5)$$

The virtual origin for the streamwise velocity is then at $y = -\ell_x$. The streamwise flow thus perceives an apparent, no-slip wall at a distance ℓ_x below the riblet tips, $y = 0$. In wall units, the mean streamwise shear $dU^+/dy^+ = 1$ very near the wall, and so (1.5) becomes $U^+(y^+ = 0) = \ell_x^+$. In other words, the slip velocity experienced by the mean flow is equal to the streamwise slip length expressed in wall units, so the concept of the slip length ℓ_x^+ is often used interchangeably with that of the slip velocity $U_s^+(y^+ = 0) = \ell_x^+$.

The above implies that the spanwise velocity, generated by the quasi-streamwise vortices of the near-wall cycle, would perceive an origin at the riblet tips $y = 0$. In general, this is not

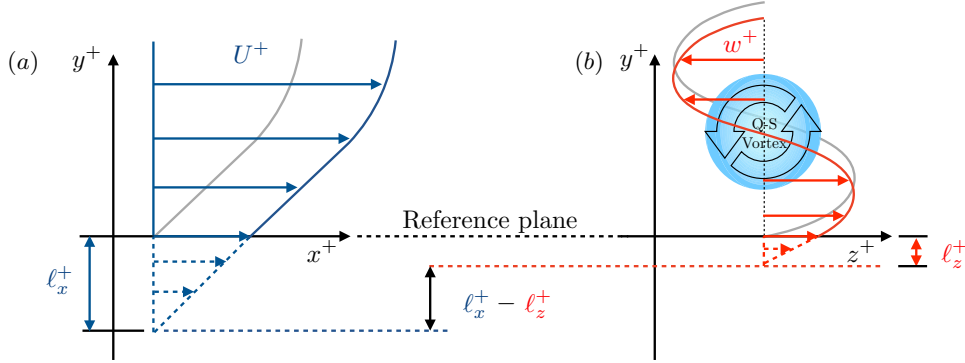


Figure 1.4 Schematic of (a) streamwise and (b) spanwise slip lengths, ℓ_x^+ and ℓ_z^+ , and the corresponding virtual origins at $y^+ = -\ell_x^+$ and $y^+ = -\ell_z^+$. A quasi-streamwise (Q-S) vortex, inducing a spanwise velocity w^+ , is sketched in (b). Grey profiles indicate smooth-wall behaviour with the wall located at the reference plane. Adapted from Gómez-de-Segura and García-Mayoral (2020).

the case, and the vortices would instead perceive an origin at some distance below the plane $y = 0$. Luchini et al. (1991) proposed, therefore, that it would also be necessary to consider a spanwise slip length, ℓ_z , to properly describe the effect of riblets on the flow with respect to the reference plane $y = 0$. Again, this would be equivalent to a Navier slip condition at $y = 0$ on the spanwise velocity,

$$w = \ell_z \frac{\partial w}{\partial y}, \quad (1.6)$$

where $y = -\ell_z$ would be the location of the virtual origin for the spanwise turbulent fluctuations generated primarily by the quasi-streamwise vortices, as portrayed in figure 1.4(b). Luchini et al. (1991) concluded that the only important parameter in determining the drag reduction due to riblets would be the difference between these two virtual origins, i.e. $\ell_x - \ell_z$. The physical justification for this is that the origin perceived by the quasi-streamwise vortices would likely set the origin perceived by the whole turbulence dynamics, as proposed by Luchini (1996). In other words, the dynamics of turbulence would be displaced ‘rigidly’ with the vortices and they would both perceive a virtual origin at the same depth, which would be at $y = -\ell_z$ in the above framework. Note that even though this analysis was conducted in the context of riblets, it is also valid for any small-textured surface that generates different virtual origins for the streamwise and spanwise velocities. The relationship between ΔU^+ and $\ell_x - \ell_z$ was studied further by Luchini (1996), for riblets, and by Jiménez (1994), in a texture-independent framework, and they concluded that $\Delta U^+ \propto \ell_x^+ - \ell_z^+$ for $\ell_x^+, \ell_z^+ \lesssim 1$, with a constant of proportionality of order 1. García-Mayoral et al. (2019) argued recently that the constant of proportionality must necessarily be 1, i.e. $\Delta U^+ = \ell_x^+ - \ell_z^+$. In practice, the requirement $\ell_x^+, \ell_z^+ \lesssim 1$ can be somewhat relaxed, provided that the overlying flow perceives only the homogenised effect of the texture. This would require the texture to be smaller than the overlying turbulent eddies in the flow.

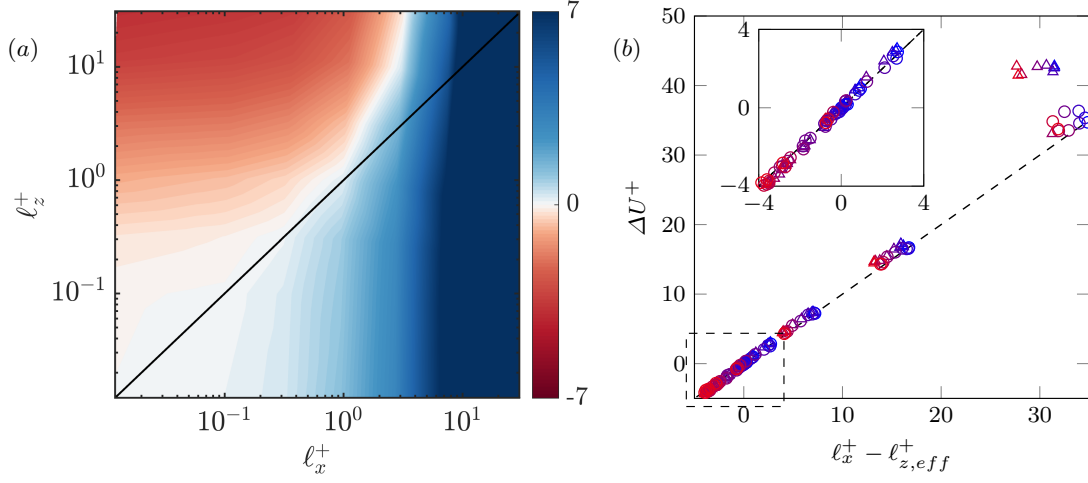


Figure 1.5 (a) Map of ΔU^+ for different slip lengths, ℓ_x^+ and ℓ_z^+ , from Busse and Sandham (2012) starting from a smooth-wall friction Reynolds number $Re_{\tau,0} = 180$. Black solid line, $\ell_x^+ = \ell_z^+$. (b) ΔU^+ as a function of $\ell_x^+ - \ell_{z,eff}^+$, using the same data as in (a). Triangles, simulations at $Re_{\tau,0} = 180$; circles, simulations at $Re_{\tau,0} = 360$. From blue to red, the spanwise slip length increases. Dashed line, $\Delta U^+ = \ell_x^+ - \ell_{z,eff}^+$. Adapted from Fairhall and García-Mayoral (2018).

However, when the spanwise slip length generated by a surface becomes larger than a few wall units, the effect of ℓ_z^+ on ΔU^+ starts to saturate (Min and Kim, 2004; Fukagata et al., 2006). Busse and Sandham (2012) conducted a parametric study for a wide range of streamwise and spanwise slip lengths and showed that, for $\ell_x^+ \gtrsim 4$, drag is reduced for all values of ℓ_z^+ , as shown in figure 1.5(a). In this regime, ΔU^+ is no longer simply proportional to the difference between the streamwise and spanwise slip lengths. If it were, the contours in figure 1.5(a) would be symmetric about the diagonal line. Fairhall and García-Mayoral (2018) have since shown that this saturation can be accounted for with an ‘effective’ spanwise slip length, $\ell_{z,eff}^+$, which is empirically observed to be

$$\ell_{z,eff}^+ \approx \frac{\ell_z^+}{1 + \ell_z^+/4}. \quad (1.7)$$

The change in drag would then be $\Delta U^+ = \ell_x^+ - \ell_{z,eff}^+$. For $\ell_z^+ \lesssim 1$, $\ell_{z,eff}^+ \approx \ell_z^+$, recovering the above expression that $\Delta U^+ = \ell_x^+ - \ell_z^+$, while for large values of ℓ_z^+ , $\ell_{z,eff}^+$ asymptotes to 4. From (1.7), if the spanwise slip length was $\ell_z^+ = 1$, the effective spanwise slip length would be a similar $\ell_{z,eff}^+ = 0.8$. However, $\ell_z^+ = 2$ would only yield $\ell_{z,eff}^+ = 1.3$, a reduction of more than 30%. The two-dimensional parametric space (ℓ_x^+, ℓ_z^+) in figure 1.5(a) can be fitted to a single curve using (1.7), as shown in figure 1.5(b). Note that the figure demonstrates that we can extend the validity of (1.7) from $\ell_x^+, \ell_z^+ \sim 1$ to $\ell_x^+, \ell_z^+ \sim 30$ at least, so long as the flow only perceived the underlying texture in a homogenised fashion. There is some deviation for the cases at the lower smooth-wall friction Reynolds number, $Re_{\tau,0} = 180$, when the streamwise slip length is large, $\ell_x^+ \sim 100$. This was likely a low-Reynolds-number effect associated with the

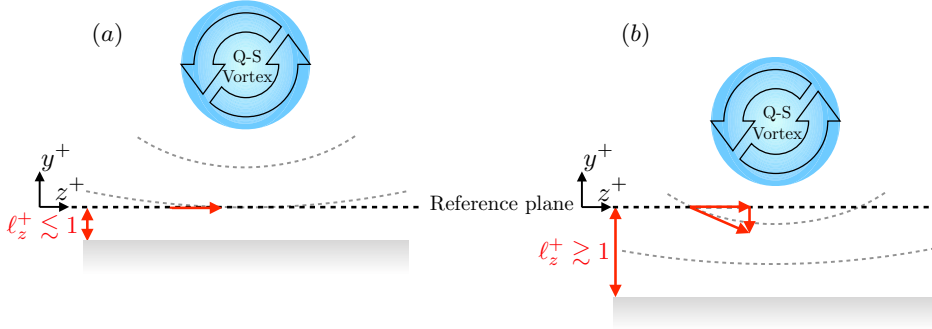


Figure 1.6 Schematic of spanwise and wall-normal velocities induced by quasi-streamwise (Q-S) vortices at the reference plane for (a) virtual origins $\ell_z^+ \lesssim 1$ and (b) larger virtual origins. Shaded grey regions indicate the apparent smooth wall perceived by the vortex. Adapted from [Gómez-de-Segura and García-Mayoral \(2020\)](#).

flow relaminarising, since the simulations were conducted at constant mass flow rate, so that a large drag reduction resulted in a significant decrease in Re_τ .

[Gómez-de-Segura et al. \(2018a\)](#) have recently investigated the cause for this saturation in the effect of ℓ_z^+ (1.7). The underlying assumption of the linear law, $\Delta U^+ = \ell_x^+ - \ell_z^+$, is that the only effect of the quasi-streamwise vortices is to induce a Couette-like, transverse shear at the reference plane $y = 0$, but no wall-normal velocity, as portrayed in figure 1.6(a). This is valid as long as $\ell_z^+ \lesssim 1$, since w is linear just above the wall, whereas v is quadratic, and hence vanishes more rapidly with y . In this regime, the effect of the surface on the flow would be captured by the conditions $u = \ell_x \partial u / \partial y$, $w = \ell_z \partial w / \partial y$ and $v = 0$ at $y = 0$. This is the regime contemplated by the pioneering work of [Luchini et al. \(1991\)](#), which is consistent with the ‘homogenisation’ approaches of [Lauga and Stone \(2003\)](#), [Kamrin et al. \(2010\)](#), [Luchini \(2013\)](#) and [Lācis and Bagheri \(2017\)](#), in which homogeneous, equivalent boundary conditions are derived from a mathematical analysis of the effect of the texture on the overlying flow. However, as ℓ_z^+ increases and the vortices further approach the reference plane, the assumption of impermeability is no longer valid, since, for the vortices to continue to approach the reference plane unimpeded, they would require a non-negligible wall-normal velocity at $y = 0$. This concept is depicted in figure 1.6(b). [Gómez-de-Segura et al. \(2018a\)](#) argue, therefore, that the displacement, on average, of the vortices towards the reference plane would necessarily saturate eventually, unless the shift of the origin perceived by w was also accompanied by a corresponding shift of the origin perceived by v . They conducted preliminary simulations to find a suitable method to impose a virtual origin on v and to test this hypothesis. Amongst the several methods studied by [Gómez-de-Segura et al. \(2018a\)](#), it was later concluded by [Gómez-de-Segura and García-Mayoral \(2020\)](#) that a Robin boundary condition at $y = 0$, $v = \ell_y \partial v / \partial y$, was a simple yet suitable one. The inclusion of a wall-normal ‘slip length’ ℓ_y , sometimes referred to as a ‘transpiration length’, can be introduced in a homogenisation framework using second-or-higher order expansion ([Bottaro, 2019](#); [Lācis et al., 2020](#); [Bottaro and Naqvi, 2020](#)). Irrespective of the

texture, and focussing solely on the overlying flow, if the origin perceived by the spanwise and wall-normal velocity fluctuations is the same, Gómez-de-Segura et al. (2018a) observed that the saturation in the effect of ℓ_z^+ no longer occurred. This suggests that, in general, to fully describe the effects of a small-textured surface on the flow, it may be necessary to consider virtual origins for all three velocity components, because the virtual origin for v can also play an important role in setting the apparent origin for the quasi-streamwise vortices. This implies that, when the virtual origins perceived by v and w differ, the quasi-streamwise vortices, and hence the overlying turbulence, might perceive a virtual origin at some intermediate plane between the two (Gómez-de-Segura et al., 2018a; García-Mayoral et al., 2019). This is extensively investigated in chapter 3.

1.2.3 Opposition control and virtual origins

As well as textured surfaces that passively impose virtual origins on the three velocity components, Gómez-de-Segura et al. (2018a) discussed the possibility that the effect of active opposition control (Choi et al., 1994) could also be interpreted in terms of virtual origins. This idea stems from the observation that opposition control, when applied to the wall-normal velocity alone, would establish a ‘virtual wall’ approximately halfway between the detection plane, $y^+ = y_d^+$, and the physical wall, $y^+ = 0$ (Hammond et al., 1998). Gómez-de-Segura et al. (2018a) extended this concept to the general case where all three velocity components could be opposed, which would, in principle, result in each velocity component perceiving a different virtual origin at a plane above the physical wall. Choi et al. (1994) explored several active control strategies, including opposition control of the wall-normal velocity alone (v control), of the spanwise velocity alone (w control), and of both w and v (w - v control). Schematics of these three strategies are shown in figure 1.7. In each case, the velocity components imposed at the wall, $y^+ = 0$, were opposite to those measured at $y^+ \approx 10$. Choi et al. (1994) reported that the control caused an upward shift of the log law and an outward shift of the turbulence intensities, compared to the uncontrolled flow. These findings are consistent with the reduction in skin friction being a result of an outward shift of the origin perceived by turbulence with respect to the mean flow, which is the same mechanism by which many textured surfaces are understood to reduce drag. In section 3.6, we explore this idea further by analysing the effect of opposition control on the turbulence statistics in terms of the apparent virtual origins perceived by each velocity component.

1.3 The logarithmic layer

We refer to the intermediate region between the buffer and outer layers as the logarithmic layer. In the buffer layer the relevant length scale is ν/u_τ , but in the outer layer the length scale is set by δ . In the logarithmic layer, $y^+ \gg 1$ and $y/\delta \ll 1$, and so the relevant length scale is neither

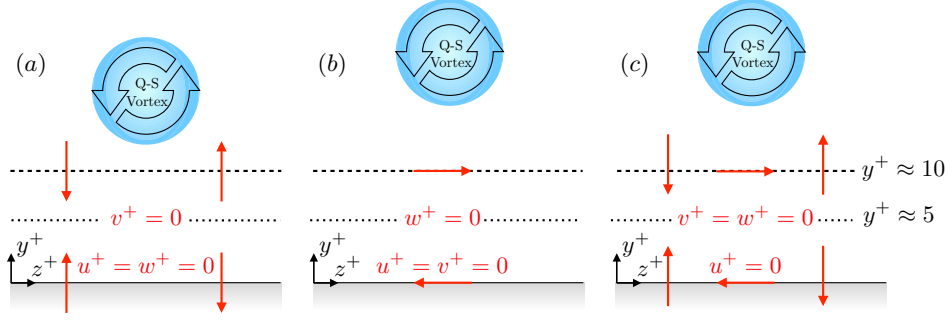


Figure 1.7 Schematics of the different control strategies studied by Choi et al. (1994). Opposition control applied on (a) v , (b) w , (c) both v and w . Shaded grey regions denote the physical wall, where the control is applied. Adapted from Gómez-de-Segura et al. (2018a).

ν/u_τ nor δ . The classical understanding is that this leaves the distance from the wall, y , as the only remaining length scale for the flow in this region. In this thesis, we focus on channels flows, for which we define the limits of the logarithmic layer approximately as (Sillero et al., 2013)

$$80\nu/u_\tau \lesssim y \lesssim 0.3\delta. \quad (1.8)$$

As mentioned above, one of the aims of this thesis is to investigate the effect of controlling the flow within the logarithmic layer, without directly controlling the flow elsewhere, and assess how this effect changes as the Reynolds number varies. To provide some context, in this section we first consider the variation of the mean velocity profile and logarithmic layer with friction Reynolds number $Re_\tau = \delta^+$. This could have implications on the effect of a given logarithmic-layer control strategy as the Reynolds number varies. We then discuss the structure of the flow in the logarithmic layer, focussing on the concept of attached eddies.

1.3.1 Variation of the mean velocity profile and logarithmic layer with Re_τ

From the above limits of the logarithmic layer (1.8), we see that its thickness, both in inner and outer units, varies with Reynolds number. Mean velocity profiles for canonical, smooth-wall turbulent channel flows are shown in figure 1.8 for four friction Reynolds numbers in the range $360 \leq Re_\tau \leq 2000$, in both outer and inner units. For comparison, the upper and lower bounds of the logarithmic layer are included for each Reynolds number. In the logarithmic layer, we assume that the mean velocity in wall units depends only on the distance from the wall, such that

$$U^+(y^+) = \frac{1}{\kappa} \log y^+ + A. \quad (1.9)$$

Here, the constant $A \approx 5$ is the y -intercept of the logarithmic law. Note the collapse in figure 1.8(b) of the profiles in wall units within the buffer and logarithmic layers. As the Reynolds number increases, we also observe an approximate logarithmic increase in the channel

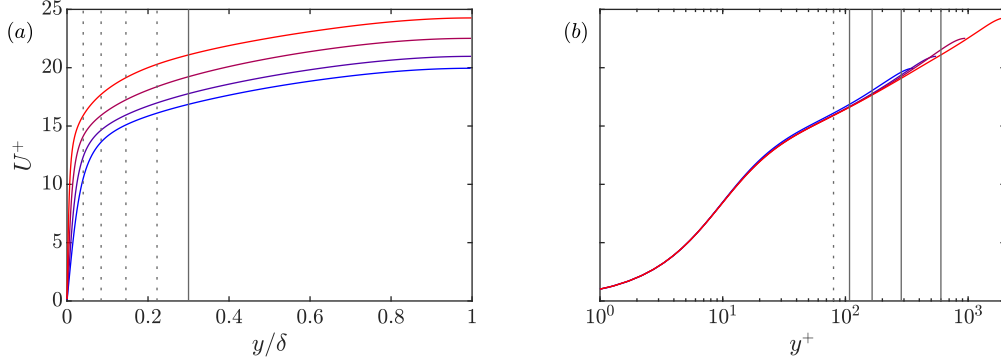


Figure 1.8 Mean velocity profiles U^+ for $Re_\tau = 360, 550, 950$ and 2000 (blue to red lines) against (a) y/δ and (b) y^+ . In each panel, the lower bound of the logarithmic layer is denoted by the dotted vertical lines, and the upper bound by the solid vertical lines. Note that the upper bound of the logarithmic layer is fixed in outer units, y/δ , while the lower bound is fixed in wall units, y^+ .

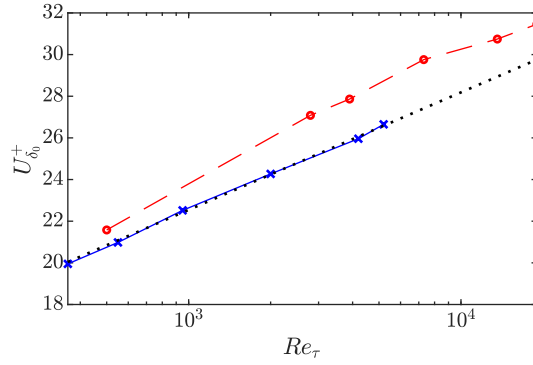


Figure 1.9 Variation of centreline velocity in wall units with Re_τ for channel flows, blue line with crosses, and zero pressure gradient boundary layers, red dashed line with circles. The black dotted line denotes an approximate logarithmic fit, $U_{\delta_0}^+ = 2.45 \log Re_\tau + 5.62$, for the channel data. The boundary layer data are from [Marusic et al. \(2010\)](#). The channel data at $Re_\tau = 4200$ and 5200 are from [Lozano-Durán and Jiménez \(2014\)](#) and [Lee and Moser \(2015\)](#), respectively. The lower Reynolds number channel data are from the present study.

centreline velocity in wall units, $U_{\delta_0}^+$, as portrayed in figure 1.9. This is expected, since the mean velocity at upper limit of the logarithmic layer, $U^+(y^+ = 0.3Re_\tau)$, increases logarithmically with Re_τ , from (1.9), and the variation in the mean velocity profile above the logarithmic layer is approximately universal in outer units y/δ . Therefore, the variation of $U_{\delta_0}^+$ with Re_τ comes primarily from the increase in mean velocity at the upper limit of the logarithmic layer.

From (1.8), it is easy to show that the thickness of the logarithmic layer in wall units varies linearly with Re_τ ,

$$\Delta y_{log}^+ = 0.3Re_\tau - 80. \quad (1.10)$$

The thickness of the logarithmic layer in outer units, however, varies with $1/Re_\tau$,

$$\frac{\Delta y_{log}}{\delta} = 0.3 - \frac{80}{Re_\tau}, \quad (1.11)$$

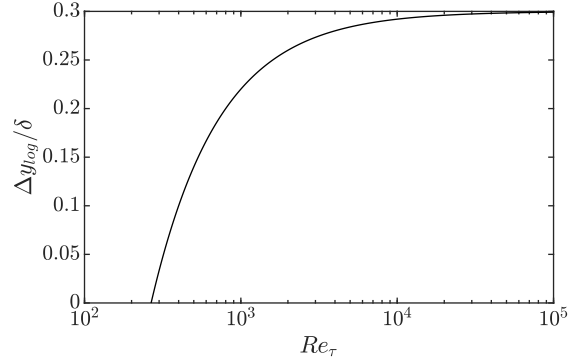


Figure 1.10 Variation of logarithmic layer thickness in outer units, $\Delta y_{log}/\delta$, with Re_τ , defined by (1.11).

which is also derived directly from (1.8). Equation (1.11) is portrayed in figure 1.10, where we see that the thickness of the logarithmic layer saturates by $Re_\tau \simeq 2 \times 10^4$. In other words, for $Re_\tau \gtrsim 2 \times 10^4$, the thickness of the buffer layer becomes negligible in outer units, and the logarithmic layer essentially spans the region $0 \lesssim y/\delta \leq 0.3$. It is typically considered that $Re_\tau \gtrsim 10^4$ is the range of industrial relevance (Jiménez, 2018), and this therefore highlights the limitations of control strategies that target the buffer layer alone. However, it is important to note that the mean velocity at the edge of the buffer layer is $U^+(y^+ = 80) \approx 16$ for all Reynolds numbers, as shown in figure 1.8(b). Therefore, while the thickness of the buffer layer becomes negligible in outer units, the velocity jump within it remains significant, even for large Re_τ . Figure 1.10 also emphasises that Δy_{log} is strictly positive only when $Re_\tau \gtrsim 270$. Therefore, care should be taken when discussing concepts such as the logarithmic layer in the context of results at low Re_τ .

1.3.2 Self-similar, attached eddies in wall-bounded turbulence

In contrast to the relatively simple structure of the flow in buffer layer discussed in section 1.1, the flow in the logarithmic layer is much more complex and its dynamics occur across a wide range of scales. In order to better understand the dynamics of the flow in the logarithmic layer, various attempts have been made to describe the flow in this region in terms of coherent structures or eddies. One of the first, and arguably most famous, is the attached eddy hypothesis proposed by Townsend (1961, 1976). This is based on the assumption that the flow within the logarithmic layer is dominated by a family of self-similar eddies that extend down to, or close to, the wall, and that their length and velocity scales are set only by their distance from the wall and the friction velocity, respectively. Townsend (1976) demonstrated that a population density of attached eddies that varies inversely with their size, and hence with distance from the wall, results in the logarithmic law (1.9) for the mean profile, as well as expressions for the streamwise and spanwise mean-squared velocity fluctuations that decrease logarithmically with distance from the wall. Townsend (1961) also proposed that these attached eddies in the

logarithmic layer would either be ‘active’ or ‘inactive’, in terms of their contribution to the mean shear. The idea is that, at a given height, active motions are responsible for generating the local Reynolds shear stress, whereas inactive ones are larger and contribute to the Reynolds shear stress much further from the wall. In a sense, the inactive motions in the logarithmic layer are determined by the turbulence in the outer layer [Bradshaw \(1967\)](#), and hence this can account for the differences in outer-layer turbulence statistics across different types of wall-bounded flows, e.g. boundary layers or channel flows.

Several works have been dedicated to extending the attached eddy hypothesis into a model for the flow using specific eddy geometries. Indeed, [Townsend \(1976\)](#) himself suggested streamwise vortices in the form of a double-cone roller, although in the end this did not satisfy the underlying assumptions of the model. [Perry and Chong \(1982\)](#) proposed a hierarchy of self-similar wall-attached ‘ λ -vortices’, inspired by the early work that advocated horseshoe vortices as the key coherent structure in wall-bounded turbulent flows ([Theodorsen, 1952](#)). [Adrian et al. \(2000\)](#) later proposed a model consisting of packets of hairpin vortices that grow from the wall into the outer region of the flow. While these models are able to reproduce well the first- and second-order statistic in the logarithmic layer, there is limited experimental evidence that these kinds of vortical structures exist above the buffer layer ([Jiménez, 2012](#)). For a comprehensive review on the attached eddy model and its various refinements, the reader is referred to the review of [Marusic and Monty \(2019\)](#).

A key point raised in that review is that the specific geometry of the eddies is not important, as long as they obey the assumptions of the attached eddy hypothesis. This is problematic because any predictions beyond low-order statistics, e.g. the distribution of energy among length scales, are dependent on eddy shape. Therefore, the kinds of attached eddies just described may not be representative of the eddies observed in real flows. Another interesting question is whether it is necessary for the eddies to be physically attached to the wall. The work of [Davidson and Krogstad \(2009\)](#), which builds on [Davidson et al. \(2006\)](#), provides a simplified model that does not require the eddies to be attached to the wall, only that their kinetic energy scales with distance from the wall. In this framework, [Davidson and Krogstad \(2009\)](#) are able to reproduce the logarithmic variation with y of the streamwise mean-squared velocity fluctuations in the logarithmic layer. [Mizuno and Jiménez \(2013\)](#) and [Encinar et al. \(2014\)](#) also demonstrate, using direct numerical simulations with off-wall boundary conditions, that it is possible to recover the logarithmic mean velocity profile without resolving the dynamics of the buffer layer, i.e. without the direct effect of the wall, although they note that some knowledge of the wall is required. Further, [Kwon and Jiménez \(2021\)](#) show that it is possible to reproduce the essential dynamics of the logarithmic layer in the absence of both a buffer and an outer layer, although they emphasise that this is not to say that the flow in the logarithmic layer is not influenced by the flow elsewhere. The idea that the dynamics of the logarithmic layer can be recovered without resolving the flow in the buffer layer suggests that it is not essential for the logarithmic-layer eddies to extend all the way down to the wall, as proposed by the

attached eddy model. A further extension to the attached eddy model was proposed recently by [Lozano-Durán and Bae \(2019\)](#), who postulated that the scales of flow in the logarithmic layer need not necessarily be set by the friction at and the distance to the wall, and that the traditional no-slip and impermeability conditions are not needed to recover canonical wall-bounded turbulence far from the wall.

The attached eddy model could provide a useful tool for describing the hierarchy of structures in wall-bounded turbulence, but it should be emphasised that it is based on a hypothesis, as discussed above, and therefore should be treated with caution. However, thanks to recent advances in computing power and the availability of fully-resolved data from direct numerical simulations of turbulent flows at higher Reynolds numbers, more evidence has emerged that supports the existence of self-similar attached eddies in wall-bounded turbulent flows. For instance, [del Álamo et al. \(2006\)](#) analysed vortex clusters in DNSs of turbulent channel flows, and observed that the logarithmic region is populated by both small detached and tall attached clusters. The small detached clusters are essentially dissipative objects, while the tall attached ones can be described as shells of disorganised vorticity extending from below $y^+ \approx 20$ into the logarithmic layer. They found that the lengths and widths of these attached clusters were proportional to their height, forming a self-similar family in the logarithmic layer with aspect ratio 3:1:1.5 in the streamwise, wall-normal and spanwise directions, respectively. They also observed that the clusters grow self-similarly with time and originate from different heights within the logarithmic layer. [Del Álamo et al. \(2006\)](#) concluded that these clusters were associated with sweeps of low-speed fluid away from the wall, which generates a long low-velocity streak, and found that the dimensions of the clusters agreed well with the dominant length scales in the energy spectrum of the wall-normal velocity. [Flores and Jiménez \(2010\)](#) later demonstrated that the minimum domain size required to sustain healthy turbulence in the logarithmic layer at a height y is $L_x \times L_z = 6y \times 3y$, which respects the same aspect ratio as the vortex clusters of [del Álamo et al. \(2006\)](#).

The large-scale sweeps observed by [del Álamo et al. \(2006\)](#) were investigated further by [Lozano-Durán et al. \(2012\)](#). They studied three-dimensional Reynolds-stress structures in turbulent channels by conducting a quadrant analysis, in which every point in the flow is classified in terms its location in the parameter plane of the streamwise and wall-normal velocity, $u-v$. These structures are referred to as ‘Qs’. [Lozano-Durán et al. \(2012\)](#) define Q1 events (outward interactions) as regions with $u > 0$ and $v > 0$, Q2 events (ejections) as regions with $u < 0$ and $v > 0$, Q3 events (inward interactions) as regions with $u < 0$ and $v < 0$ and Q4 events (sweeps) as regions with $u > 0$ and $v < 0$. Q2 and Q4 (‘gradient’) events are grouped together as Q^- , while Q1 and Q3 (‘counter-gradient’) events are grouped together as Q^+ . They found that detached Q’s are typically small and are representative of the background fluctuations of the tangential Reynolds stress. In contrast, wall-attached Qs are larger and consist mostly of Q^- events, which are responsible for approximately 60% of the total Reynolds stress in the logarithmic layer and above. The majority of these attached Q^- s form a self-similar family

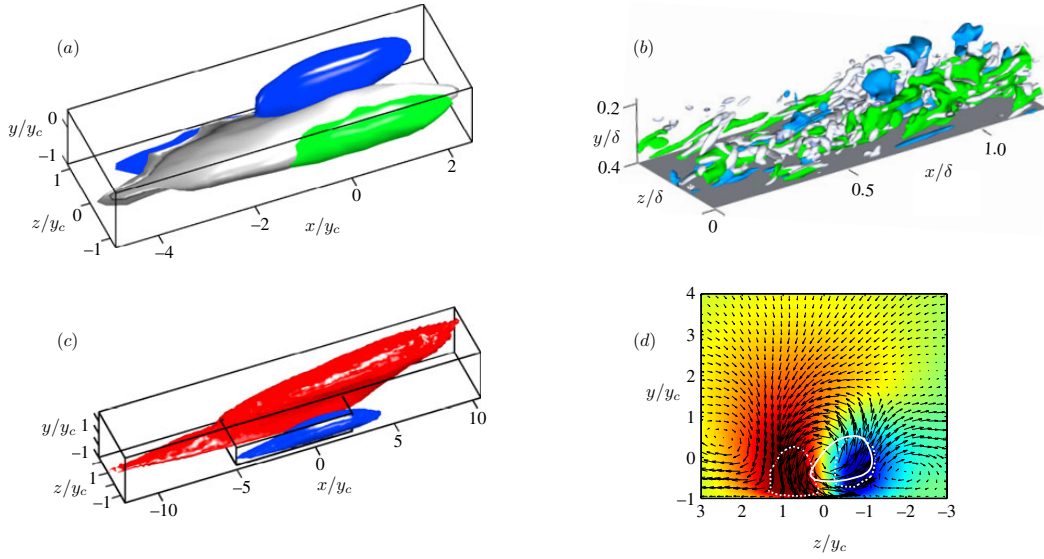


Figure 1.11 Flow fields conditions to attached Q2-Q4 pairs in the logarithmic layer, reproduced with permission from [Lozano-Durán et al. \(2012\)](#), © 2012 Cambridge University Press. Note that the axis labels have been modified to be consistent with the nomenclature in this thesis. Here, y_c is the height of the centre of gravity of the conditional Q^- pair. (a) P.d.f.s of the points belonging to the Q2 (green), Q4 (blue) and vortex clusters (grey). (b) Example of an instantaneous Q2-Q4 pair, with vortex cluster. Colour code as in (a). (c) Conditional streamwise perturbation velocity. The blue object is the low-speed isosurface, and the red one is the high-speed isosurface. (d) Cross-section of the conditional flow field at $x/y_c = 0$. The arrows are the cross-flow (v, w), and the shaded map is the streamwise velocity, with colours as in (c). The white dotted lines represent the p.d.f. of the points belonging to the Q2-Q4 pair, and the white solid line represents the vortex cluster.

with aspect ratio 3:1:1 in the streamwise, wall-normal and spanwise directions. This aspect ratio agrees well with the dimensions of the uv cospectrum and is similar to that of the vortex clusters found by [del Álamo et al. \(2006\)](#).

[Lozano-Durán et al. \(2012\)](#) also observed that adjacent Q^- events of the same sign, e.g. a Q2 and its nearest Q2, are preferentially aligned streamwise, while Q^- events of the opposite sign, e.g. Q2 and Q4, form spanwise pairs. Figure 1.11 shows the averaged flow field conditioned around pairs of attached Q^- in the logarithmic layer. Since the Q^- pairs come in all sizes with self-similar aspect ratios, the conditional average is compiled after rescaling each pair to a common size and centring it on the centre of gravity of the pair, located at y_c . Figure 1.11(a) shows the average shape of the Q^- pair and its associated cluster, where we see that the cluster is located between the two Q's, but closer to the Q2 ejection. The aspect ratio of the conditional object in figure 1.11(a) is approximately 4:1:1.5 in the three coordinate directions. As a result of this sweep-ejection pair, the conditional flow field contains a pair of high- and low-speed streamwise streaks, as shown in figure 1.11(c). These streaks are reinforced by the presence of a streamwise-aligned roller, which can be observed in the y - z cross-section of the flow field in figure 1.11(d).

It should be emphasised that the instantaneous flow is not as smooth as the conditionally averaged flow fields in figure 1.11(*a, c, d*). A snapshot of a typical sweep-ejection pair is shown in figure 1.11(*b*) for comparison, where we observe that the Q structures are themselves turbulent and are made up of smaller eddies. In section 1.1, we discussed the nature of the flow in the buffer layer, where $y^+ \lesssim 80$. The flow in that region is dominated by streaks and quasi-streamwise vortices, and there is essentially no scale separation between energy and dissipation (Jiménez, 2013). If y is the distance to the wall, y^+ can be viewed as a characteristic Reynolds number for the size of the structures at that height. In the buffer layer, y^+ is never large, which implies that the eddies in that region are relatively smooth and well-defined. In contrast, $y^+ \gg 1$ in the logarithmic layer, and so the structure and dynamics of the flow are much more complex, and a large range of scales are present. It is therefore expected that the large eddies observed in the logarithmic layer are themselves intrinsically turbulent, consisting of smaller and smaller eddies, and there will be significant scale separation between energy and dissipation (Jiménez, 2012, 2013).

As well as the observations from DNSs discussed above, there has been growing experimental evidence in recent years that supports the existence of self-similar, wall-attached structures in the logarithmic layer of turbulent boundary layers. For instance, Baars et al. (2017) observed self-similar, wall-attached eddies in the form of long streamwise streaks from two-point streamwise velocity signals, and Baidya et al. (2017) demonstrated that the size of the dominant v^2 and wv motions in the logarithmic layer exhibit a distance-from-the-wall scaling. Recently, Baidya et al. (2021) showed over a wide range of Reynolds numbers that the variance of the spanwise velocity fluctuations varies logarithmically with distance from the wall within the logarithmic layer. These findings provide further support for the attached eddy hypothesis of Townsend (1976).

Various reduced-order descriptions of the flow within the logarithmic layer have also started to emerge that are consistent with the attached eddy hypothesis. Along similar lines to the study of Flores and Jiménez (2010), Hwang and Bengana (2016) carried out over-damped large-eddy simulations in restricted domains and identified self-sustaining turbulent solutions to the Navier–Stokes equations in the form of attached logarithmic-layer eddies that exhibit similar dynamics to the buffer layer cycle discussed in section 1.1. This analysis was later extended by Yang et al. (2019), who found exact (invariant) solutions of the Navier–Stokes equations that consist of self-similar, attached travelling waves within the logarithmic layer. Taking a different approach, McKeon (2019) demonstrated that a self-similar hierarchy of attached eddies can also be obtained using resolvent analysis, and showed that this reduced-order description of the flow can be consolidated, at least to some extent, within the attached eddy framework. We discussed above that the specific eddy geometry is not important in the context of the attached eddy framework, and that low-order statistics, e.g. the mean velocity profile and mean-squared velocity fluctuations, can be recovered so long as the assumptions of the attached eddy hypothesis are obeyed. The resolvent analysis of McKeon (2019) is essentially the

inverse scenario, since the mean velocity profile is prescribed a priori. Therefore, the resulting self-similar structures will satisfy the mean profile, by definition, but may not capture the higher-order statistics of the flow.

1.4 Objectives

In section 1.2, we discussed in detail how small-textured surfaces modify the drag compared to a smooth surface by imposing different virtual origins on the flow velocity components. The early works considered a virtual origin for the wall-parallel velocity components only, but recent results suggest that a virtual origin for the wall-normal velocity is also necessary to fully describe the effect of the texture (Gómez-de-Segura et al., 2018a; Gómez-de-Segura and García-Mayoral, 2020). In this thesis, we examine the effect on near-wall turbulence of displacing the virtual origins perceived by the different components of the overlying flow. The aim is to develop a unifying virtual-origin framework in which the effect of the surface texture or flow-control strategy can be reduced to a relative offset between the virtual origins perceived by different components of the flow, and which components those would be. This effect has been observed in direct numerical simulations (DNSs) of certain textured surfaces (Gómez-de-Segura et al., 2018b), and also in DNSs with active opposition control (Choi et al., 1994). We impose virtual origins on each of the three velocity components in direct numerical simulations (DNSs) of turbulent channels using Robin, slip-length-like boundary conditions at the domain boundaries, which has been proposed by Gómez-de-Segura and García-Mayoral (2020) as a simple and effective method. In the case of surface texture that is isotropic in the wall-parallel directions, it can be shown that this kind of boundary condition actually arises from a mathematical analysis of the effect of the texture on the overlying flow (Bottaro, 2019; Bottaro and Naqvi, 2020; Lācis et al., 2020).

The focus of this aspect of the thesis is the extent to which the velocities perceiving different virtual origins modify the dynamics of turbulence. We also aim to determine if it is possible to predict the shift in the mean velocity profile, ΔU^+ , a priori from the apparent virtual origins perceived by the flow. While the observation that some textures produce such an effect is the motivation behind this aspect of the thesis, it is beyond our scope to quantify this effect for specific textures, although some preliminary work on this can be found in Gómez-de-Segura et al. (2018b). Figure 1.12 portrays results from that study. The figure demonstrates that when the texture size is small enough, there is a linear regime in which ΔU^+ is equal to the height difference between the virtual origin perceived by the mean flow, $y^+ = -\ell_U^+$, and the virtual origin perceived by turbulence, $y^+ = -\ell_T^+$. This effect will be discussed in detail in chapter 3. We note that it is also beyond our scope to derive equivalent boundary conditions for specific textures, or to establish the connection between such equivalent conditions and the observed virtual-origin effect. These concepts are discussed further in section 2.2.

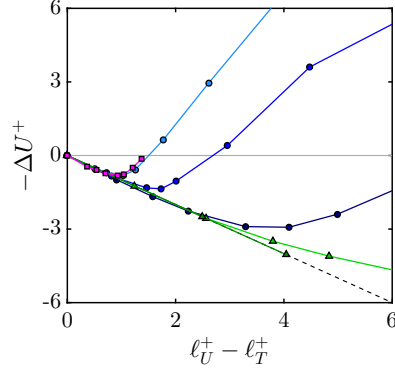


Figure 1.12 ΔU^+ for various types of complex surfaces as a function of the difference between the virtual origins $\ell_V^+ - \ell_T^+$. Adapted from Gómez-de-Segura et al. (2018b). $-\square-$, riblets; $-\circ-$, from light to dark blue, permeable substrates with increasing streamwise to wall-normal permeability ratios; $-\triangle-$, superhydrophobic surfaces with regular and randomly distributed posts.

As well as studying the control of the buffer layer, we also wish to gain a better understanding of the potential drag reduction achievable by manipulating the flow in the logarithmic layer. To this end, we investigate the effect of controlling the flow within the logarithmic layer alone, without directly modifying the flow elsewhere, and attempt to assess how this effect varies with Reynolds number. We first consider the effect of the Reynolds number on the drag reduction achievable by an idealised, hypothetical logarithmic-layer control strategy. We then conduct a series of direct numerical simulations of turbulent channels at friction Reynolds numbers in the range $360 \leq Re_\tau \leq 2000$ and investigate the effect of controlling the flow in the logarithmic layer alone. The general idea of these simulations is to target the self-similar, wall-attached sweep and ejection motions discussed in section 1.3.2. As well as the use of wall-normal jets in experiments mentioned above (Abbassi et al., 2017; Ruan et al., 2018, 2019), another possible strategy could be to control these structures with a technique akin to opposition control (Choi et al., 1994). For this strategy, the large-scale wall-normal fluctuations in the logarithmic layer, generated by the sweeps and ejections, would be opposed with blowing and suction at the wall (see e.g. Guseva et al., 2019). While this might achieve the desired effect far from the wall, the near-wall turbulence cycle could be significantly disrupted, if not eradicated entirely. In contrast, Toedtli et al. (2020) studied the effect of varying-phase opposition control within the buffer layer. They found that for large positive phase shifts the control resulted in wide spanwise-aligned rollers, which caused an increase in drag, eradicated the near-wall turbulence cycle and significantly modified the flow across a large part of the channel. This suggests that even when only the small scales in the buffer layer are targeted with opposition control, this can still generate large-scale, possibly undesirable, changes in the flow. In our simulations, we attempt to decouple the effects of modifying the flow in the buffer and logarithmic layers, and assess the effect of controlling the logarithmic-layer structures and their dynamics alone, without directly affecting the turbulence in the near-wall region. We do this by artificially

setting to zero certain streamwise and spanwise length scales from the wall-normal velocity across a range of heights, primarily within the logarithmic layer of the flow. The idea is to make the contribution to uv for those length scales to be zero, disrupting the sweep and ejection motions discussed above. While it would not be possible to implement this form of control in reality, it is hoped that our simulations might provide insight into the effect of controlling the logarithmic layer alone, while affecting the rest of the flow as little as possible, providing bounds for what can realistically be achieved.

We note that [de Giovanetti et al. \(2016\)](#) also investigated the effect of controlling large-scale attached structures, and concluded that, at sufficiently large Reynolds numbers, most of the skin friction is generated by turbulent motions in the logarithmic layer of the flow. Their method involved damping all turbulent fluctuations larger than a given spanwise wavelength across the full extent of the channel by restricting the spanwise extent of the domain, without discriminating between velocity components or particular wall-normal locations. When all spanwise wavelengths larger than 0.2δ are removed, they observed a reduction in skin friction of approximately 60%. However, since their simulations were conducted at constant mass flow rate, this could be attributed, at least in part, to the relative gain in mean velocity in the logarithmic layer and above, and the subsequent drop in pressure gradient, similar to the effect seen in the minimal channel flows of [Chung et al. \(2015\)](#) and [MacDonald et al. \(2016\)](#). In this thesis we employ a more targeted approach. As mentioned above, we remove only certain streamwise and spanwise scales from the wall-normal velocity across only specific heights. The aim is to control the flow in the logarithmic layer, while affecting the rest of the flow as little as possible, and, in contrast to the study of [de Giovanetti et al. \(2016\)](#), we do not control the flow in the wake region. Ultimately, this could improve our understanding of the potential drag reduction achievable by logarithmic-layer control strategies.

1.5 Organisation of the thesis

The remaining chapters of this thesis are organised as follows:

Chapter 2 summarises the numerical methods used. We describe the DNS solver and discuss the use of Robin conditions to impose virtual origins on each of the three velocity components. We also outline the method for removing specific streamwise and spanwise wavelengths from the wall-normal velocity in the logarithmic-layer control simulations.

Chapter 3 concerns the study on virtual origins. Here, we discuss in detail the effect on the flow of imposing different virtual origins for all three velocity components. We propose, from physical and empirical arguments, an expression that can be used to predict ΔU^+ from the apparent virtual origins a priori. We also analyse results from opposition-control simulations, which suggest that certain active flow-control techniques can also be interpreted in terms of virtual origins. We present a theoretical, eddy-viscosity framework

that produces a priori the effect observed in our simulations. The findings presented in this chapter have been published in [Ibrahim et al. \(2021\)](#).

Chapter 4 begins our discussion on the control of the logarithmic layer. We consider the effect on the flow of an idealised, hypothetical logarithmic-layer control strategy, and derive a general expression for the drag reduction that depends on the Reynolds number. This expression may be used as a theoretical prediction for the maximum drag reduction achievable by strategies that target the logarithmic layer directly.

Chapter 5 presents the results of the logarithmic-layer control simulations, in which we artificially remove certain streamwise and spanwise length scales of v , primarily within the logarithmic layer. We analyse the effect of the control on the flow both within the logarithmic layer and in the buffer and outer layers, and discuss how its performance changes as the Reynolds number varies. We also compare the results of our simulations to the idealised control strategy presented in chapter 4. Preliminary results from this chapter have been published in [Ibrahim et al. \(2020\)](#).

Chapter 6 summarises the main conclusions of this thesis and provides some comments on potential avenues for future work.

Chapter 2

Numerical methods

This chapter outlines the numerical methods used in this thesis. First, in section 2.1, we provide a general overview of the direct numerical simulation solver used to simulate the turbulent flow within a channel. Next, the aspects of the code specific to this work are explained. The use of Robin slip-length-like boundary conditions for imposing different virtual origins on different components of the flow is discussed in section 2.2. Then, the implementation of opposition control at the channel walls for all three velocity components is summarised in section 2.3. Finally, the method for artificially removing certain streamwise and spanwise wavelengths of the wall-normal velocity within the logarithmic layer of the flow is presented in section 2.4.

2.1 DNS of turbulent channel flows

In this section, we outline the method for the direct numerical simulation (DNS) of turbulent channel flow. The simulations are conducted in a domain doubly periodic in the wall-parallel directions, using a code adapted from [García-Mayoral and Jiménez \(2011b\)](#) and [Fairhall and García-Mayoral \(2018\)](#). We solve the non-dimensional, unsteady, incompressible Navier–Stokes equations

$$\frac{\partial \mathbf{u}}{\partial t} + \mathbf{u} \cdot \nabla \mathbf{u} = -\nabla p + \frac{1}{Re} \nabla^2 \mathbf{u}, \quad (2.1)$$

$$\nabla \cdot \mathbf{u} = 0, \quad (2.2)$$

where $\mathbf{u} = (u, v, w)$ is the velocity vector with components in the streamwise, x , wall-normal, y , and spanwise, z , directions, respectively, p is the kinematic pressure and Re is the channel bulk Reynolds number. In the streamwise and spanwise directions, due to the periodicity of the domain, the variables are solved in Fourier space, applying the 2/3 dealising rule when computing the nonlinear advective terms. The wall-normal domain is discretised using a second-order centred finite difference scheme on a staggered grid. Time integration is carried out using the fractional step method ([Kim and Moin, 1985](#)), along with a three-step Runge–Kutta

| | | |
|-----------------------------|-----------------------------|----------------------------|
| $\alpha_1 = \beta_1 = 4/15$ | $\alpha_2 = \beta_2 = 1/15$ | $\alpha_3 = \beta_3 = 1/6$ |
| $\gamma_1 = 8/15$ | $\gamma_2 = 5/12$ | $\gamma_3 = 3/4$ |
| $\zeta_1 = 0$ | $\zeta_2 = -17/60$ | $\zeta_3 = -5/12$ |

Table 2.1 Runge–Kutta coefficients (Le and Moin, 1991).

scheme. The Runge–Kutta coefficients are shown in table 2.1, and are the same as in Le and Moin (1991), for which semi-implicit and explicit schemes are used to approximate the viscous and advective terms, respectively.

Our simulations are conducted at five friction Reynolds numbers, $Re_\tau = 180, 360, 550, 950$ and 2000 . In each case, the flow is driven by a constant streamwise pressure gradient, in order to keep the friction velocity u_τ and thus the friction Reynolds $Re_\tau = \delta^+$ fixed. Therefore, changes in drag compared to uncontrolled (or smooth-wall) reference channels are observed through changes in the channel bulk velocity, U_b , and not the friction at the wall. The viscous length scale, therefore, also remains constant. In all cases the channel half-height is $\delta = 1$. For the majority of the simulations, the wall-parallel domain size is given by $L_x = 2\pi$ and $L_z = \pi$. This has been shown by Lozano-Durán and Jiménez (2014) to be sufficiently large to capture the key turbulence processes and length scales of the buffer and logarithmic layers of the flow, and reproduce well the one-point statistics of domains of larger size. Parameters relating to the typical domain size and grid resolution for each Reynolds number are summarised in table 2.2. The grid resolution in the wall-parallel directions, Δx^+ and Δz^+ , is quoted in collocation points, in dealiasing space. In the wall-normal direction, the grid is stretched such that it has a minimum value, Δy_{min}^+ , at the wall and a maximum value, Δy_{max}^+ , at the channel centre. Note that some simulations are conducted in domains with larger wall-parallel dimensions. When this is the case, any differences will be made clear. The variable time step is controlled by

$$\Delta t = \min \left\{ 0.7 \left[\frac{\Delta x}{\pi|u|}, \frac{\Delta z}{\pi|w|}, \frac{\Delta y}{\pi|v|} \right], 2.5Re \left[\frac{\Delta x^2}{\pi^2}, \frac{\Delta z^2}{\pi^2}, \frac{\Delta y^2}{4} \right] \right\}, \quad (2.3)$$

which corresponds to maintaining a convective CFL number of 0.7 and a viscous one of 2.5. In all cases, the flow is allowed to evolve until any initial transients have decayed, and then statistics are collected over a window of at least 20 largest-eddy turnover times, $T_E = \delta/u_\tau$, unless specified otherwise.

2.2 Robin, slip-length-like boundary conditions

Virtual origins for the three velocity components are introduced into the DNS solver by imposing Robin, slip-length boundary conditions at the channel walls, following Gómez-de-Segura and

| Re_τ | L_x/δ | L_z/δ | Δx^+ | Δz^+ | Δy_{min}^+ | Δy_{max}^+ |
|-----------|--------------|--------------|--------------|--------------|--------------------|--------------------|
| 180 | 2π | π | 5.9 | 2.9 | 0.29 | 2.9 |
| 360 | 2π | π | 5.9 | 3.0 | 0.27 | 2.6 |
| 550 | 2π | π | 9.0 | 4.5 | 0.29 | 3.0 |
| 950 | 2π | π | 9.2 | 4.6 | 0.33 | 5.0 |
| 2000 | 2π | π | 10.9 | 5.5 | 0.33 | 6.6 |

Table 2.2 Summary of parameters relating to the typical domain size and grid resolution in the present study. Δx^+ and Δz^+ denote the grid resolution in the wall-parallel directions in terms of collocation points, in dealiasing space. Δy_{min}^+ and Δy_{max}^+ are the minimum and maximum spacing between grid points in the wall-normal direction, due to the grid stretching.

García-Mayoral (2020). At the bottom wall of the channel, these take the form

$$u|_{y=0} = \ell_x \frac{\partial u}{\partial y} \Big|_{y=0}, \quad v|_{y=0} = \ell_y \frac{\partial v}{\partial y} \Big|_{y=0} \quad \text{and} \quad w|_{y=0} = \ell_z \frac{\partial w}{\partial y} \Big|_{y=0}, \quad (2.4)$$

so that u , v and w at the domain boundary are related to their respective wall-normal gradients by the three slip lengths, ℓ_x , ℓ_y and ℓ_z . Equivalent, symmetric boundary conditions are also applied to the top wall of the channel. The coupling between velocity components, their wall-normal gradients and the pressure is fully implicit and embedded in the LU factorisation intrinsic in the fractional-step method (Perot, 1993). A detailed description of the implementation of this type of boundary conditions can be found in Gómez-de-Segura and García-Mayoral (2019). Note that for v , ℓ_y is not physically a ‘slip length’ as v is not parallel to the wall, but, by extension, we will also refer to ℓ_y as the ‘slip length’ in the wall-normal direction. To prevent any net surface mass flux, the slip length for the xz -averaged wall-normal velocity is set to zero, and hence ℓ_y is only applied to its fluctuating component. Note also that a free-slip condition, e.g. $\partial u/\partial y = 0$, is equivalent, in principle, to imposing an infinitely large slip length, $\ell_x = \infty$.

It is important to mention that, formally, first-order homogenisation produces Robin boundary conditions for the tangential velocities alone, and a non-zero transpiration arises only for second- or higher-order expansions. Our boundary conditions should thus not be viewed as equivalent boundary conditions in the sense of homogenisation, but purely as a method to impose virtual origins. Although not the focus of this paper, we refer the reader to the works of Bottaro (2019), Bottaro and Naqvi (2020) and Lācis et al. (2020) for the discussion on how to obtain such equivalent boundary conditions for actual textures. The expansion in homogenisation is typically done for the small parameter given by the ratio of the texture size to the flow thickness. One difficulty in turbulent flows, however, is that the ratio would need to remain small even for the smallest length scales in the flow. These would typically be the diameter of the near-wall quasi-streamwise vortices or their height above the surface, both of order 15 wall units (Robinson, 1991; Schoppa and Hussain, 2002). This implies that for the expansion to converge the texture size would need to be even smaller. Most textures in that size range, however, behave as hydraulically smooth (Jiménez, 1994). As discussed in

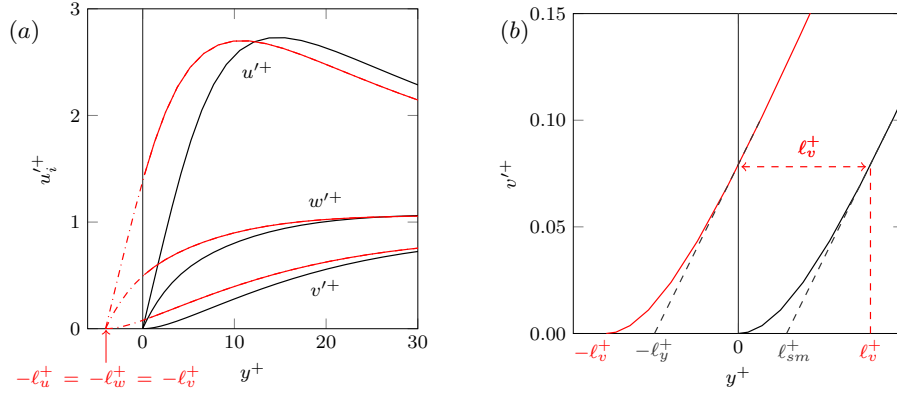


Figure 2.1 Schematics showing (a) the definition of virtual origins ℓ_u^+ , ℓ_w^+ and ℓ_v^+ as the shift of the r.m.s. velocity fluctuations with respect to a smooth channel; (b) the distinction between ℓ_v^+ and ℓ_y^+ . Adapted from Gómez-de-Segura and García-Mayoral (2020).

chapter 1, it is beyond the scope of the present thesis to derive equivalent boundary conditions for specific textures, or to establish the connection between such equivalent conditions and the observed virtual-origin effect. Alternatively, the focus of this work is the extent to which the velocities perceiving different virtual origins modify the dynamics of turbulence. Nevertheless, Lācis et al. (2020) and Bottaro and Naqvi (2020) argue that retaining the first non-trivial (non-zero) coefficients in the expansion for each velocity component yields Robin conditions that are equivalent to (2.4), at least for x - z isotropic textures, and that these three coefficients dominate the physics.

While the concepts of slip lengths and virtual origins have been used interchangeably in the literature, following Gómez-de-Segura and García-Mayoral (2020) we make a subtle but important difference. Let us denote by ℓ_x^+ , ℓ_y^+ and ℓ_z^+ the slip lengths in the streamwise, wall-normal and spanwise directions, respectively, which are defined exclusively as the Robin coefficients for the simulation boundary conditions (2.4). Physically, they simply correspond to the wall-normal locations where the velocity components become zero when linearly extrapolated from the reference plane, $y = 0$. In order to associate the imposed slip lengths with smooth-wall data a priori, we define the virtual origins of u , v and w as the notional distance below the reference plane where each velocity component would perceive a virtual, smooth wall. To do this, we assume the shape of each r.m.s.-fluctuation profile would remain the same as over a smooth wall, independently of the others. The virtual origins would then be located at $y^+ = -\ell_u^+$, $y^+ = -\ell_v^+$ and $y^+ = -\ell_w^+$, respectively. We note that this is not physics-based, but it simply allows us to establish an a priori correspondence between the offset in each velocity component and the slip length for that velocity while accounting for the non-linear behaviour of the fluctuating velocities, especially for v , near the wall. The definition of these virtual origins is illustrated in figure 2.1(a). The slip lengths for the Robin boundary conditions (2.4) are therefore set with the objective of yielding a prescribed set of virtual origins ℓ_u , ℓ_v and

ℓ_w . Table 3.1 summarises the parameters of the simulations that we conduct in this study. For each case, the slip lengths ℓ_x^+ , ℓ_z^+ and ℓ_y^+ are given, along with the corresponding virtual origins ℓ_u^+ , ℓ_w^+ and ℓ_v^+ . Since the virtual origins are computed from the slip lengths a priori, assuming the shape of smooth-wall velocity profiles remain unchanged, there is a one-to-one a priori relationship between slip lengths and virtual origins. The simulations are split into various ‘families’, each designed to systematically test a particular aspect of this virtual-origin framework. For example, some cases impose a virtual origin on v alone (denoted by ‘V’), while other cases impose a virtual origin on both u and v (denoted by ‘UV’), and so on. The exact purpose of each family is explained in chapter 3. Note that for some of the simulations, the slip length applied to the mean flow, $\ell_{x,m}$, is different to the slip length applied to the streamwise fluctuations, ℓ_x . Since we solve the flow in Fourier space in the wall-parallel directions, this can be implemented easily by imposing different slip-length boundary conditions on the different modes $\hat{u}(k_x, k_z, y)$ as required, where k_x and k_z are the streamwise and spanwise wavenumbers, respectively.

For a virtual origin of a few wall units, we expect the slip lengths ℓ_x^+ and ℓ_z^+ to be approximately equal to ℓ_u^+ and ℓ_w^+ , because the wall-parallel velocities u^+ and w^+ are essentially linear in the immediate vicinity of the wall. The case of the wall-normal velocity, however, is less straightforward. Since v^+ is essentially quadratic very near the wall, the height of the virtual origin perceived by v^+ , $y^+ = -\ell_v^+$, can differ significantly from the slip length ℓ_y^+ , even for small values, as illustrated in figure 2.1(b). We choose ℓ_y^+ as the ratio between v^+ and dv^+/dy^+ at a height $y^+ = \ell_v^+$ above a smooth wall. From figure 2.1(b), ℓ_y^+ and ℓ_v^+ are related by $\ell_y^+ = \ell_v^+ - \ell_{sm}^+$, where ℓ_{sm}^+ is obtained by linearly extrapolating the slope of the smooth-wall profile at $y^+ = \ell_v^+$. Note that the value of ℓ_{sm}^+ is a function of ℓ_v^+ , as it depends on the local slope of the profile at the height from which the extrapolation is calculated. A curvature effect can also be significant for ℓ_w^+ , since the profile of w^+ becomes noticeably curved for $y^+ \gtrsim 2$, but this effect is small for u^+ . Since the mean velocity profile is approximately linear up to $y^+ \approx 5$, the distance below the plane $y^+ = 0$ of the virtual origin experienced by the mean flow, ℓ_U^+ , is essentially equal to the slip velocity of the mean flow in wall units, U_s^+ , and also to its slip length, $\ell_{x,m}^+$. It should, however, be mentioned that in general, if ℓ_x^+ is large enough, the virtual origin perceived by the mean flow, $y^+ = -\ell_U^+$, is not necessarily coincident with the virtual origin for the streamwise fluctuations, $y^+ = -\ell_u^+$, since their profiles curve differently as they approach the wall, even if $\ell_x^+ = \ell_{x,m}^+$.

2.3 Opposition control

As well as the virtual-origin simulations described above, we also investigate the effect of opposition control (Choi et al., 1994) from the viewpoint of virtual origins. We carry out three simulations at $Re_\tau \approx 180$, applying opposition control to v alone, w alone, and both v and w . The same DNS code as for the virtual-origin simulations is used, with the only difference being

the imposed boundary conditions. The control is implemented in the code explicitly, with the measured velocity at the plane $y^+ = y_d^+$ at time step n is opposed at the wall at time step $n + 1$. A summary of the opposition-control simulations is given in table 3.2, including several parameters relevant to their interpretation in terms of virtual origins. These simulations are discussed in detail in section 3.6.

2.4 Artificially removing length scales from the wall-normal velocity

In chapter 5, we present and discuss the results of various DNSs in which we artificially remove certain streamwise and spanwise length scales from the wall-normal velocity, v , primarily within the logarithmic layer. We discussed the motivation for this aspect of the present thesis in chapter 1. The general idea is to inhibit the dynamics of the self-similar, wall-attached eddies within the logarithmic-layer discussed in section 1.3.2. In an averaged sense, these structures consist of a vortex cluster flanked by a sweep-ejection pair, with a corresponding pair of high- and low-speed streaks, as portrayed in figure 1.11 (del Álamo et al., 2006; Flores and Jiménez, 2010; Lozano-Durán et al., 2012). The sweep and ejection motions, known collectively as Q^- events, are associated with coherent regions of Reynolds stress uv . The combined aspect ratio of the sweep-ejection pair and its associated vortex cluster is approximately 4:1:1.5 in the streamwise, wall-normal and spanwise directions, respectively (Lozano-Durán et al., 2012). If the sweep-ejection pair is positioned so its centre of gravity is at y_c , then it will have a length of approximately $8y_c$ in the streamwise direction, a height of $2y_c$ in the wall-normal direction and a width of $3y_c$ in the spanwise direction. Note that the aspect ratio of the vortex cluster alone is approximately 3:1:1.5 (del Álamo et al., 2006). By removing specific scales from v , we thus remove the contribution of those scales to uv , which would, in turn, remove their contribution to the sweep and ejection motions associated with the vortex clusters. Next, we outline the method for removing only certain scales from v .

The wall-normal velocity in Fourier space may be written as $\hat{v}(k_x, k_z, y)$, where k_x and k_z are the streamwise and spanwise wavenumbers, respectively. The wavenumbers satisfy $-N_x/2 \leq k_x \leq N_x/2 - 1$ and $-N_z/2 \leq k_z \leq N_z/2 - 1$, where N_x and N_z are the total number of modes in each wall-parallel direction. Each unique pair of wavenumbers (k_x, k_z) is referred to as a ‘mode’, and the length scale of a mode is given by the pair of wavelengths associated with its wavenumbers, $(\lambda_x, \lambda_z) = (L_x/|k_x|, L_z/|k_z|)$. Note, therefore, that each unique pair of wavelengths (λ_x, λ_z) has contributions from four pairs of wavenumbers, i.e. the four modes $(\pm k_x, \pm k_z)$. In each simulation, a certain set of length scales will be removed from the flow across a range of heights primarily within the logarithmic layer. We will refer to these removed length scales as the target length scales or wavelengths, $\lambda_{x,t}$ and $\lambda_{z,t}$, and the region in which they are

removed as the forcing region. The forcing region, y_f , is defined by $y_{f,min} \leq y_f \leq y_{f,max}$. In general, the target wavelengths will vary across the forcing region.

The wavelengths are removed by explicitly setting to zero the relevant modes of v in our simulations at every time step, after the predictor step. This is easily achieved, because the code solves for the primitive variables in Fourier space. Note that the initial conditions for these simulations were taken from reference uncontrolled flows at the same Reynolds number. Since the forcing is only imposed in some y planes, with no smoothing, abrupt gradients could be observed in the flow in the first instance, especially in the wall-normal velocity at the interface between forced and unforced heights. These sharp gradients were, however, observed to smooth out after an initial transient, as continuity resulted in only small values of v in the unforced planes adjacent to the forced ones. From the point of view of the forced modes, these interfaces act thereafter as impermeable-but-slipping boundaries.

Our logarithmic-layer forcing simulations can be broadly split into two groups, which we refer to as simulations with ‘block forcing’ and simulations with ‘hierarchical forcing’. The details of these simulations, including the specific choices of target length scales and forcing regions, will be outlined in chapter 5 and are summarised in tables 5.1 and 5.2.

Chapter 3

A unifying virtual-origin framework for turbulence over drag-altering surfaces

In this chapter, we present the results of direct numerical simulations of turbulent channels in which we impose different virtual origins for the different velocity components using Robin slip-length-like boundary conditions (2.4). The implementation of these boundary conditions and their interpretation as virtual origins is discussed in detail in section 2.2. A summary of the simulations we conduct is provided in table 3.1. The aim is to determine the effect on the flow of imposing different virtual origins for each velocity component. In particular, we are concerned with how ΔU^+ and the near-wall turbulence dynamics are affected by the virtual origins. We also wish to better understand the physical mechanism at play, such that we can potentially predict the effect of the virtual origins on the flow a priori.

The findings presented in this chapter have been published in [Ibrahim et al. \(2021\)](#).

3.1 The origin for turbulence

In section 1.2, we introduced the idea that the quasi-streamwise vortices, and hence turbulence, might perceive an intermediate origin between the virtual origins perceived by v and w . We now discuss this concept in more detail. Let us postulate that the only effect of the virtual origins, particularly those perceived by v and w , on the near-wall turbulence is to set its origin at some intermediate plane, while the flow remains otherwise the same as over a smooth wall. In this thesis, we define ℓ_T^+ as the distance between the virtual origin perceived by turbulence and the reference plane $y^+ = 0$. When $\ell_T^+ > 0$, the virtual origin perceived by turbulence is below the reference plane, and therefore we refer to the plane $y^+ = -\ell_T^+$ as the virtual origin for turbulence. Likewise, we denote by $y^+ = -\ell_U^+$ the virtual origin perceived by the mean flow. It follows from the streamwise momentum equation that the shape of the mean velocity profile in a

| Case | Re_τ | L_x/δ | L_z/δ | ℓ_x^+ | ℓ_z^+ | ℓ_y^+ | $\ell_{x,m}^+$ | ℓ_u^+ | ℓ_w^+ | ℓ_v^+ | ℓ_U^+ | ℓ_T^+ | $\ell_{T,pred}^+$ |
|--------|-----------|--------------|--------------|------------|------------|------------|----------------|------------|------------|------------|------------|------------|-------------------|
| V1 | 180 | 2π | π | 0.0 | 0.0 | 1.2 | — | 0.0 | 0.0 | 1.9 | 0.0 | 0.0 | 0.0 |
| V2 | 180 | 2π | π | 0.0 | 0.0 | 2.5 | — | 0.0 | 0.0 | 3.9 | 0.0 | 0.0 | 0.0 |
| UV1 | 180 | 2π | π | 2.0 | 0.0 | 1.2 | — | 2.0 | 0.0 | 1.9 | 2.0 | 0.0 | 0.0 |
| UV2 | 180 | 2π | π | 4.0 | 0.0 | 2.5 | — | 3.6 | 0.0 | 3.9 | 4.0 | 0.0 | 0.0 |
| UM1 | 180 | 2π | π | 5.0 | 0.0 | 0.0 | 0.0 | 4.3 | 0.0 | 0.0 | 0.0 | 0.0 | 0.0 |
| UM2 | 180 | 2π | π | 10.0 | 0.0 | 0.0 | 0.0 | 6.6 | 0.0 | 0.0 | 0.0 | 0.0 | 0.0 |
| UM3 | 180 | 2π | π | 20.0 | 0.0 | 0.0 | 0.0 | 8.8 | 0.0 | 0.0 | 0.0 | 0.0 | 0.0 |
| UM4 | 180 | 2π | π | 50.0 | 0.0 | 0.0 | 0.0 | 11.2 | 0.0 | 0.0 | 0.0 | 0.0 | 0.0 |
| UM5 | 180 | 2π | π | 100.0 | 0.0 | 0.0 | 0.0 | 12.6 | 0.0 | 0.0 | 0.0 | 0.0 | 0.0 |
| UM6 | 180 | 2π | π | ∞ | 0.0 | 0.0 | 0.0 | ∞ | 0.0 | 0.0 | 0.0 | 0.0 | 0.0 |
| UWV1 | 180 | 2π | π | 2.0 | 2.0 | 1.2 | — | 2.0 | 1.7 | 1.9 | 2.0 | 1.7 | 1.7 |
| UWV2 | 180 | 2π | π | 3.0 | 3.0 | 1.9 | — | 2.9 | 2.4 | 3.0 | 3.0 | 2.4 | 2.4 |
| UWV3 | 180 | 2π | π | 4.0 | 4.0 | 1.2 | — | 3.6 | 2.9 | 1.9 | 4.0 | 2.7 | 2.7 |
| UWV3H | 550 | 2π | π | 4.0 | 4.0 | 1.2 | — | 3.6 | 2.9 | 1.9 | 3.9 | 2.6 | 2.7 |
| UWV3HD | 550 | 8π | 3π | 4.0 | 4.0 | 1.2 | — | 3.6 | 2.9 | 1.9 | 3.9 | 2.6 | 2.7 |
| UWV4 | 180 | 2π | π | 4.0 | 4.0 | 2.5 | — | 3.6 | 2.9 | 3.9 | 3.8 | 2.9 | 2.9 |
| UWV5 | 180 | 2π | π | 4.0 | 6.0 | 1.5 | — | 3.6 | 3.9 | 2.3 | 3.9 | 3.5 | 3.5 |
| UWV6 | 180 | 2π | π | 4.0 | 6.0 | 2.0 | — | 3.6 | 3.9 | 3.2 | 3.8 | 3.8 | 3.8 |
| UWV6M | 180 | 2π | π | 4.0 | 6.0 | 2.0 | 10.0 | 3.6 | 3.9 | 3.2 | 9.4 | 3.8 | 3.8 |
| UWVL1 | 180 | 2π | π | 6.0 | 2.0 | 4.5 | — | 4.9 | 1.7 | 6.3 | 5.7 | 2.4 | 1.7 |
| UWVL2 | 180 | 2π | π | 5.0 | 5.0 | 5.0 | — | 4.3 | 3.4 | 6.8 | 4.4 | 4.7 | 3.4 |
| UWVL3 | 180 | 2π | π | 8.2 | 11.0 | 4.3 | — | 5.9 | 5.9 | 6.0 | 6.7 | 5.7 | 5.9 |
| UWVL4 | 180 | 2π | π | 10.0 | 10.0 | 10.0 | — | 6.6 | 5.5 | 11.2 | 6.0 | 7.7 | 5.5 |
| WV1 | 180 | 2π | π | 0.0 | 2.0 | 1.2 | — | 0.0 | 1.7 | 1.9 | 0.0 | 2.1 | 1.7 |
| WV2 | 180 | 2π | π | 0.0 | 4.0 | 2.5 | — | 0.0 | 2.9 | 3.9 | 0.0 | 4.4 | 2.9 |
| WV3 | 180 | 2π | π | 0.0 | 6.0 | 2.2 | — | 0.0 | 3.9 | 3.4 | 0.0 | 4.9 | 3.9 |

Table 3.1 Summary of simulations, including the slip lengths used for the boundary conditions, ℓ_x^+ , ℓ_z^+ and ℓ_y^+ , and their corresponding virtual origins, ℓ_u^+ , ℓ_w^+ and ℓ_v^+ , calculated a priori from the smooth-wall profiles. The slip length for the mean flow, $\ell_{x,m}^+$, is given only when it is different to the slip length for the streamwise velocity fluctuations. Note that, here, Re_τ is the friction Reynolds number calculated with respect to the plane $y = 0$. The virtual origin for the mean flow, ℓ_U^+ , is given as the mean streamwise slip velocity, U_s^+ , measured at $y = 0$. The virtual origin for turbulence, ℓ_T^+ , is found a posteriori and compared to that predicted by equation (3.6), $\ell_{T,pred}^+$. In the case names, ‘U’, ‘V’ and ‘W’ denote a non-zero slip-length boundary condition on u , v and w , respectively, ‘M’ signifies that the slip applied to the streamwise velocity fluctuations is not the same as that applied to (M)ean velocity, ‘H’ is for the (H)igher Reynolds number cases at $Re_\tau = 550$, ‘D’ is for the simulation with the larger (D)omain in the streamwise and spanwise directions, and ‘L’ is for cases with (L)arge slip lengths. Note that the slip lengths, ℓ_x^+ , ℓ_z^+ and ℓ_y^+ , and virtual origins, ℓ_u^+ , ℓ_w^+ and ℓ_v^+ , are scaled with the friction velocity measured at the domain boundary, $y = 0$, whereas ℓ_U^+ and ℓ_T^+ are scaled with the friction velocity measured at the origin for turbulence $y = -\ell_T^+$. The origin for turbulence predicted from (3.6), $\ell_{T,pred}^+$, is scaled with the friction velocity at that origin, i.e. at $y = -\ell_{T,pred}^+$.

channel is determined by turbulence through the Reynolds stress (Pope, 2000; Gómez-de-Segura and García-Mayoral, 2020). If $\ell_U^+ > \ell_T^+$, the virtual origin perceived by the mean flow is deeper than that perceived by the turbulence. In this case, the mean velocity profile would be free to grow with essentially unit gradient in wall units from $y^+ = -\ell_U^+$ to $y^+ = -\ell_T^+$, due to the absence of Reynolds shear stress in the region $-\ell_U^+ \leq y^+ \leq -\ell_T^+$. Above $y^+ = -\ell_T^+$, the Reynolds shear stress would be the same as over a smooth wall, and so would the shape of the mean velocity profile, but shifted by the additional velocity $U^+(y^+ = -\ell_T^+) = \ell_U^+ - \ell_T^+$. Note that the above ideas apply to the virtual profile that would extend below $y^+ = 0$, as mentioned in section 1.2. The outward shift of the mean velocity profile would then necessarily be given by

$$\Delta U^+ = \ell_U^+ - \ell_T^+, \quad (3.1)$$

which would propagate to all heights above the plane $y^+ = -\ell_T^+$ (Gómez-de-Segura et al., 2018a; García-Mayoral et al., 2019).

The physical idea described by (3.1) was, in fact, essentially proposed by Luchini (1996), who postulated that the logarithmic law would be modified by the presence of texture only through a shift ΔU^+ “if the structure of the turbulent eddies were unaltered in the reference frame that has the transverse equivalent wall as origin, whereas the mean flow profile obviously starts at the longitudinal equivalent wall.” In other words, ΔU^+ should be the height difference between the origin for the mean flow, at $y^+ = -\ell_U^+$, and the origin for turbulence, at $y^+ = -\ell_T^+$. In this framework, from the point of view of turbulence the ‘wall’ is located at $y^+ = -\ell_T^+$, which, therefore, should also be the height of reference when comparing with smooth-wall data. Note that (3.1) is based on the assumption that the effect of the texture on the mean flow and turbulence is only to change the virtual origins that they perceive, and that the dynamics of the near-wall cycle is unaffected. This requires that the flow perceives the surface in a homogenised fashion, and the direct, granular effect of the texture is negligible (García-Mayoral et al., 2019). In the context of superhydrophobic surfaces, for instance, Fairhall et al. (2019) show that this is the case so long as the characteristic length scale of the texture in wall units satisfies $L^+ \lesssim 25$. Using the results from our DNSs, we will now examine the validity of (3.1), starting first with the dependence of ℓ_T^+ on the virtual origins imposed on the three velocity components, ℓ_u^+ , ℓ_v^+ and ℓ_w^+ .

In section 1.2 we have discussed the idea that the quasi-streamwise vortices of the near-wall cycle induce, as a first-order effect, a spanwise flow very near the wall and, as a second-order effect, a wall-normal one. This would explain the saturation in the effect of the spanwise slip length, ℓ_z^+ , in the absence of permeability, i.e. when $\ell_y^+ = 0$. Furthermore, this is consistent with the idea that when the virtual origin perceived by the wall-normal velocity is roughly at the same depth as that perceived by the spanwise velocity, $\ell_v^+ \approx \ell_w^+$, no saturation is observed (Gómez-de-Segura et al., 2018a). This implies that when imposing a virtual origin on the wall-normal velocity alone, without any spanwise slip, the virtual origin perceived by the

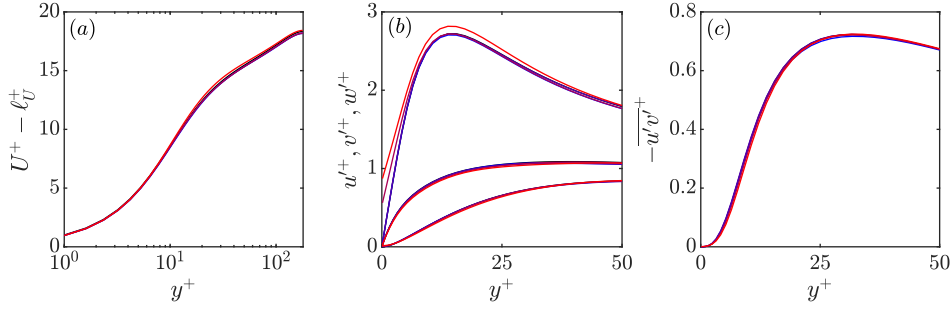


Figure 3.1 Mean velocity profiles, r.m.s. velocity fluctuations and Reynolds shear stress profiles for slip-length simulations with no spanwise slip. Black lines, smooth-wall reference data; blue to red lines, cases V1, V2, UV1 and UV2. Note that in (a), the mean streamwise slip length, ℓ_U^+ , where appropriate, has been subtracted from the mean velocity profile.

vortices should remain at the domain boundary, $y = 0$, regardless of how large ℓ_v^+ was. Since, in this case, $w = 0$ at the reference plane, and the vortices induce predominantly a spanwise flow in the vicinity of the wall, transpiration alone would not allow the vortices to move any closer to the reference plane. This is the contrasting, but complementary concept to the saturation in the effect of ℓ_z^+ in the absence of transpiration depicted in figure 1.6.

We assess the idea presented in the previous paragraph in simulations V1, V2, UV1 and UV2, all of which have $\ell_w^+ = 0$. The mean velocity profiles, r.m.s. velocity fluctuations and Reynolds stress profiles for these simulations are shown in figure 3.1. The figure supports the idea that the virtual origin experienced by the spanwise flow is, indeed, the most limiting in terms of setting the virtual origin for turbulence, and $\ell_T^+ = 0$ for all cases. For the two cases with a non-zero virtual origin for v only, cases V1 and V2, there is no change in the statistics whatsoever with respect to the smooth-wall data, even for virtual origins as large as $\ell_v^+ \approx 4$. When a non-zero virtual origin is also applied to the streamwise flow, such that $\ell_u^+, \ell_v^+ > 0$ but $\ell_w^+ = 0$, there is still no change in the wall-normal and spanwise r.m.s. velocity fluctuations, v'^+ and w'^+ , or the Reynolds stress profile. We also observe that the mean velocity profile is essentially identical to the smooth-wall case, save for the shift $\ell_U^+ = U_s^+$, as shown in figure 3.1(a). However, the peak value of the streamwise r.m.s. velocity fluctuations, u'^+ , increases as ℓ_u^+ is increased, and the u'^+ curve does not fit well the smooth-wall data near the wall for case UV2, when $\ell_u^+ = 4$. This appears to occur independently of the mean flow and other statistics, and this will be investigated further in section 3.2.

The results presented so far suggest that the quasi-streamwise vortices cannot perceive an origin deeper than the origin perceived by the spanwise velocity. We now investigate the effect on the flow when both ℓ_w^+ and ℓ_v^+ are non-zero, using simulations UWV1–UWV6. The mean velocity profiles, r.m.s. velocity fluctuations and Reynolds shear stress profiles for these simulations are included in figure 3.2. These simulations have non-zero slip-length coefficients for all three velocity components, with $\ell_x^+ \lesssim 4$, $\ell_y^+ \lesssim 2$ and $\ell_z^+ \lesssim 6$. In figure 3.2(a), after subtracting ℓ_U^+ from the mean flow in each case, we see that there is still a noticeable difference

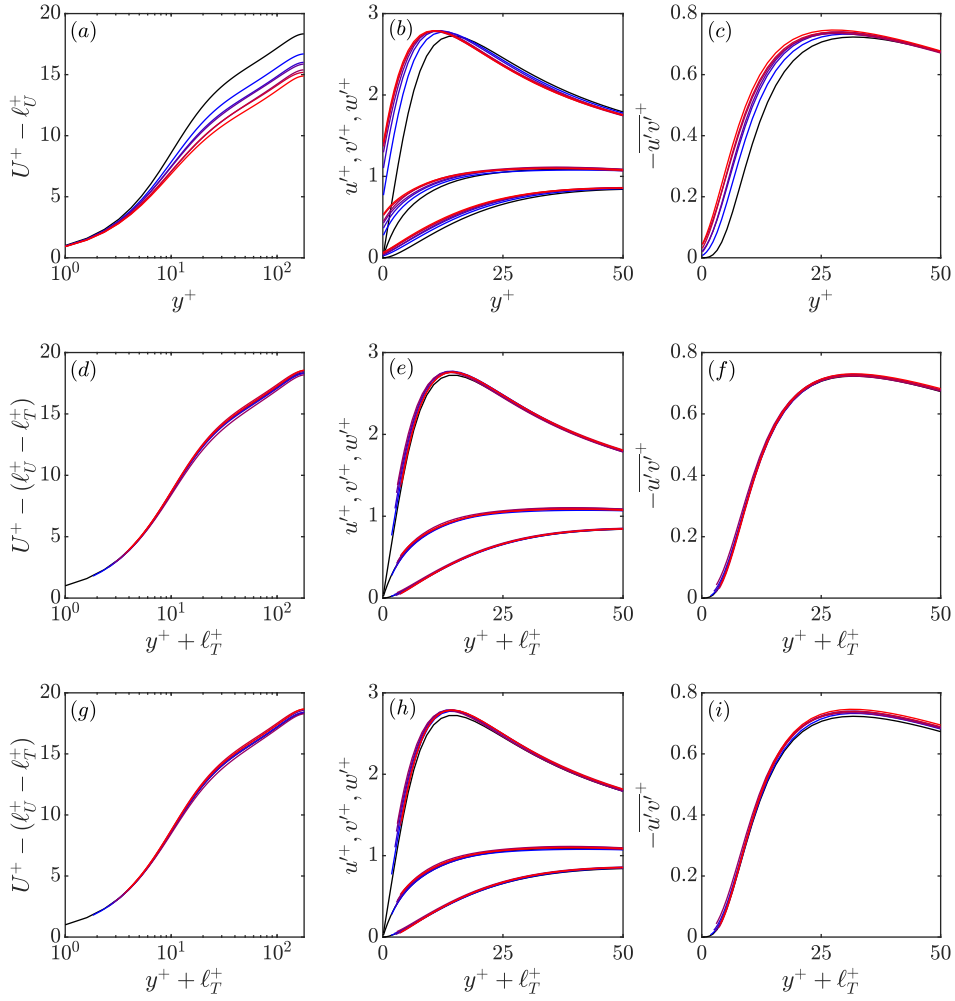


Figure 3.2 Mean velocity profiles, r.m.s. velocity fluctuations and Reynolds shear stress profiles for simulations with non-zero slip-length boundary conditions applied to all three velocity components. (a–c) scaled with the friction velocity at the reference plane, $y^+ = 0$; (d–f) shifted in y^+ by ℓ_T^+ and scaled with the friction velocity at the origin for turbulence, $y^+ = -\ell_T^+$; (g–i) shifted in y^+ by ℓ_T^+ , but scaled with the friction velocity at the reference plane, $y^+ = 0$. Black lines, smooth-wall reference data; blue to red lines, cases UWV1–UWV6.

between the mean velocity profile of the smooth-wall and the slip-length simulations. This difference is consistent with the origin for turbulence lying below the reference plane, $y^+ = 0$, which acts to increase the drag. We also observe in figure 3.2(b,c) that the velocity fluctuations and Reynolds stress profile are shifted towards $y^+ = 0$ and that their qualitative shape appears to have changed.

The above is the conventional way of representing turbulence statistics in the flow-control literature. For example, the observed reduction in velocity and vorticity fluctuations in the flow above riblets has been interpreted by some authors as the quasi-streamwise vortices being modified or damped, as well as the spanwise motion of the near-wall streaks being inhibited (see e.g. Choi et al., 1993; Chu and Karniadakis, 1993; El-Samni et al., 2007). Similarly, in studies

on the effects of superhydrophobic surfaces, authors have reported that turbulent structures are weakened, modified or disrupted by the presence of the surface (see e.g. [Min and Kim, 2004](#); [Busse and Sandham, 2012](#); [Park et al., 2013](#); [Jelly et al., 2014](#)). These interpretations would suggest that the turbulence is no longer as it would be over a smooth wall. However, following the physical arguments leading to (3.1), if turbulence remains otherwise as it would over a smooth surface, it should be possible to account for the difference with smooth-wall data by a mere origin offset.

First we discuss the choice of the friction velocity u_τ . As mentioned above, if as proposed by [Luchini \(1996\)](#) turbulence perceives a virtual smooth wall at $y = -\ell_T$, it follows that the friction velocity u_τ that scales the flow would be provided by the shear stress at that height. Since the total stress in a channel is linear with y , the friction velocity at $y = -\ell_T$ can be found by simply extrapolating the total stress curve from the domain boundary, $y = 0$. This would be given by

$$u_\tau(y = -\ell_T) = u_{\tau,0} \sqrt{\frac{\delta + \ell_T}{\delta}}, \quad (3.2)$$

where $u_{\tau,0}$ is the friction velocity measured at $y = 0$. Note that the friction velocity measured from the surface drag is not necessarily the same as the friction velocity that sets the scaling for the turbulence. Nevertheless, from (3.2), the ratio $u_\tau/u_{\tau,0}$ is close to unity as long as $\ell_T/\delta \ll 1$, which will be the case at the typical Reynolds numbers of experiments and engineering applications. As we will see below, even in the cases presented in this study, which are conducted at $Re_\tau = 180$, u_τ measured at $y = -\ell_T$ is never more than about 2% larger than $u_{\tau,0}$.

Using the friction velocity of equation (3.2), we can recalculate the viscous length scale and renormalise the measured velocities and Reynolds stress. These profiles can then be shifted in y^+ by ℓ_T^+ , where the ‘+’ superscript now indicates scaling in wall units based on the u_τ computed from (3.2). If the turbulence dynamics are indeed unmodified compared to the flow over a smooth wall, except for this shift in origin, which affects both the wall-normal coordinate and the scaling of the flow, then the r.m.s. velocity fluctuations and Reynolds stress profile should essentially collapse to the smooth-wall data. Since $\Delta U^+ = \ell_U^+ - \ell_T^+$, the only difference between the curve $U^+ - \ell_U^+$ and the smooth-wall mean velocity profile should be ℓ_T^+ at all heights.

We measure the virtual origin for turbulence a posteriori in cases UWV1–UWV6 by finding the shift that best fits the Reynolds stress curve to smooth-wall data in the near-wall region, $5 \lesssim y^+ + \ell_T^+ \lesssim 20$, and compute the friction velocity at this origin from (3.2). The measured value of ℓ_T^+ is included in table 3.1 for each case, along with the value for all the other cases considered in this study. The figure shows that when the wall-normal coordinate is measured from the virtual origin for turbulence, $y^+ = -\ell_T^+$, the wall-normal and spanwise r.m.s. fluctuations and Reynolds stress curves essentially collapse to the smooth-wall data, as shown in figures 3.2(e,f). This suggests that, in these cases, the turbulence remains essentially

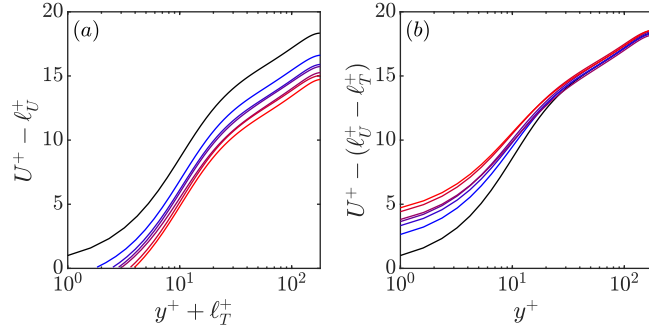


Figure 3.3 Mean velocity profiles for cases UWV1–UWV6, scaled with the friction velocity at the origin for turbulence, $y^+ = -\ell_T^+$: (a) $U^+ - \ell_U^+$ with the wall-normal coordinate measured from the origin for turbulence, $y^+ = -\ell_T^+$; (b) $U^+ - (\ell_U^+ - \ell_T^+)$ with the wall-normal coordinate measured from the boundary, $y^+ = 0$. Black lines, smooth-wall reference data; blue to red lines, cases UWV1–UWV6.

unchanged compared to the flow over a smooth wall. We will refer to this as the turbulence being essentially ‘smooth-wall like’. Further, this implies that any apparent modifications to turbulence that might be concluded from figures 3.2(b,c) are actually an apparent effect caused by the way the data is portrayed. Let us note that the resulting v'^+ and w'^+ profiles appear to perceive an origin at $y^+ = -\ell_T^+$, and not the ones prescribed a priori, $y^+ = -\ell_v^+$ and $y^+ = -\ell_w^+$. This is the expected result if v'^+ and w'^+ arise from smooth-like near-wall dynamics and are thus intrinsically coupled. The offsets ℓ_v^+ and ℓ_w^+ are merely prescribed, a priori values to quantify the offset in v and w caused by the surface, but turbulence would react to their combined effect, perceiving a single origin if it is to remain smooth-wall-like. There are some small deviations from the smooth-wall data for u'^+ , which will be discussed in section 3.2. Significantly, figure 3.2(d) demonstrates that the mean velocity profile is also smooth-wall-like, when plotted against $y^+ + \ell_T^+$, save for the difference $\Delta U^+ = \ell_U^+ - \ell_T^+$. This supports the validity of (3.1). Note also that, as discussed above, the friction velocity measured at the origin for turbulence $y = -\ell_T$ is not much larger than that measured at $y = 0$. This is emphasised by figures 3.2(g–i), which show the data shifted in y^+ by ℓ_T^+ , but scaled with the friction velocity at the reference plane, $y^+ = 0$. In this case, we see that the collapse between the statistics of cases UWV1–UWV6 and the smooth-wall data is still acceptable. This demonstrates that the apparent change in turbulence statistics, when portrayed in the conventional manner in figure 3.2(a–c), comes mostly from the change in height origin perceived by turbulence, and the change in friction velocity is only a secondary effect.

For comparison, two other possible ways of portraying the mean velocity profiles for cases UWV1–UWV6 are included in figure 3.3. Once the friction velocity is computed at the origin for turbulence, $y^+ = -\ell_T^+$, and the wall-normal coordinate is also measured from that height, the mean velocity profiles from the slip-length simulations are essentially parallel to the smooth-wall one for all y^+ , as shown in figure 3.3(a). The only difference between the curves of $U^+ - \ell_U^+$ plotted against $y^+ + \ell_T^+$ from the slip-length simulations and the smooth-wall mean velocity

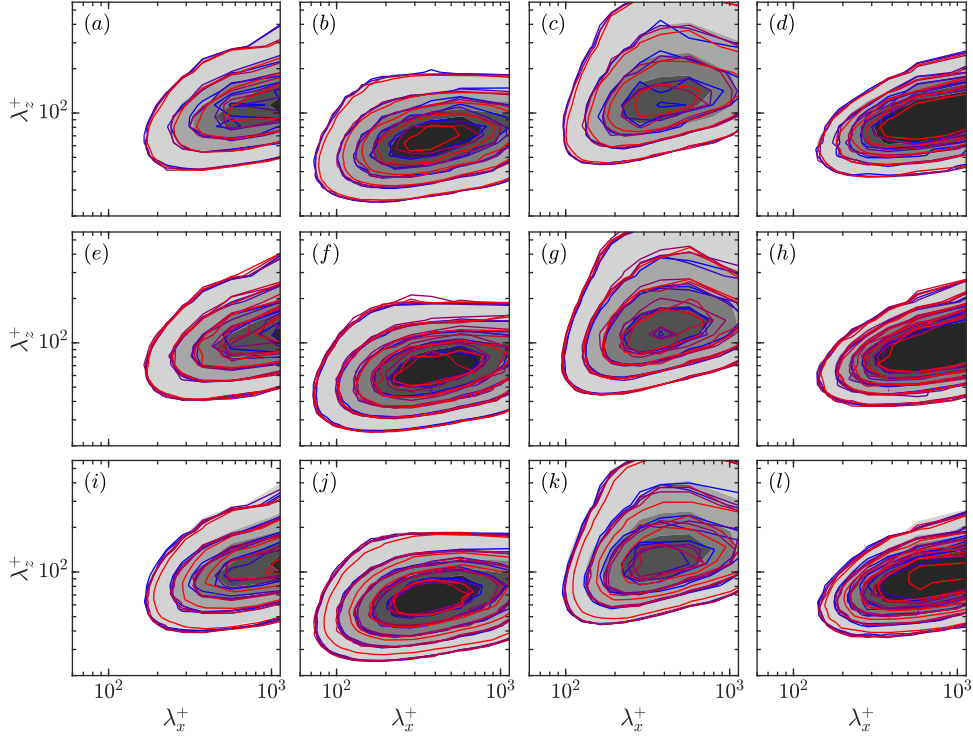


Figure 3.4 Premultiplied two-dimensional spectral densities of u^2 , v^2 , w^2 and uv at $y^+ + \ell_T^+ = 15$, normalised by u_τ at the origin for turbulence, $y^+ = -\ell_T^+$, for various slip-length simulations (line contours), compared to smooth-wall data (filled contours) at $y^+ = 15$. (a–d) cases V1, V2, UV1 and UV2, with line colours as in figure 3.1. (e–h) cases UWV1–UWV6, with line colours as in figure 3.2. (i–l) cases UM1–UM6, with line colours as in figure 3.6. First column, $k_x k_z E_{uu}^+$; second column, $k_x k_z E_{vv}^+$; third column, $k_x k_z E_{ww}^+$; fourth column, $-k_x k_z E_{uv}^+$. The contour increments for each column are 0.3224, 0.0084, 0.0385 and 0.0241, respectively.

profile is the origin for turbulence, ℓ_T^+ , as mentioned above. Alternatively, again computing the friction velocity at $y^+ = -\ell_T^+$, but now leaving $y^+ = 0$ as the datum for the wall-normal coordinate, the profiles of $U^+ - \Delta U^+$ collapse to the smooth-wall profile only for $y^+ \gg 1$, as portrayed in figure 3.3(b). In other words, the profiles collapse to the smooth-wall data only above the near-wall region of the flow (Clauser, 1956). The choice of axes in figure 3.3(b) would indicate that we have measured the correct ΔU^+ , but would not suggest that the profiles are smooth-wall-like across the whole y^+ range. The only way that they will collapse immediately from $y^+ = 0$ is to measure the wall-normal coordinate from the plane $y^+ = -\ell_T^+$, as already shown in figure 3.2(d). This also emphasises the idea that equation (3.1) will only hold if the origin for turbulence, i.e. the plane $y^+ = -\ell_T^+$, is used as reference for the turbulence dynamics, setting their scaling for velocity and length, as well as their height origin.

The collapse of the mean velocity, r.m.s. fluctuations and Reynolds stress profile to the smooth-wall data for cases UWV1–UWV6, shown in figures 3.2(d–f), indicates that the near-wall turbulent dynamics remain smooth-wall-like, and that ℓ_T^+ fully describes the effect of the virtual origins on the turbulence (García-Mayoral et al., 2019). It could, however, be argued that

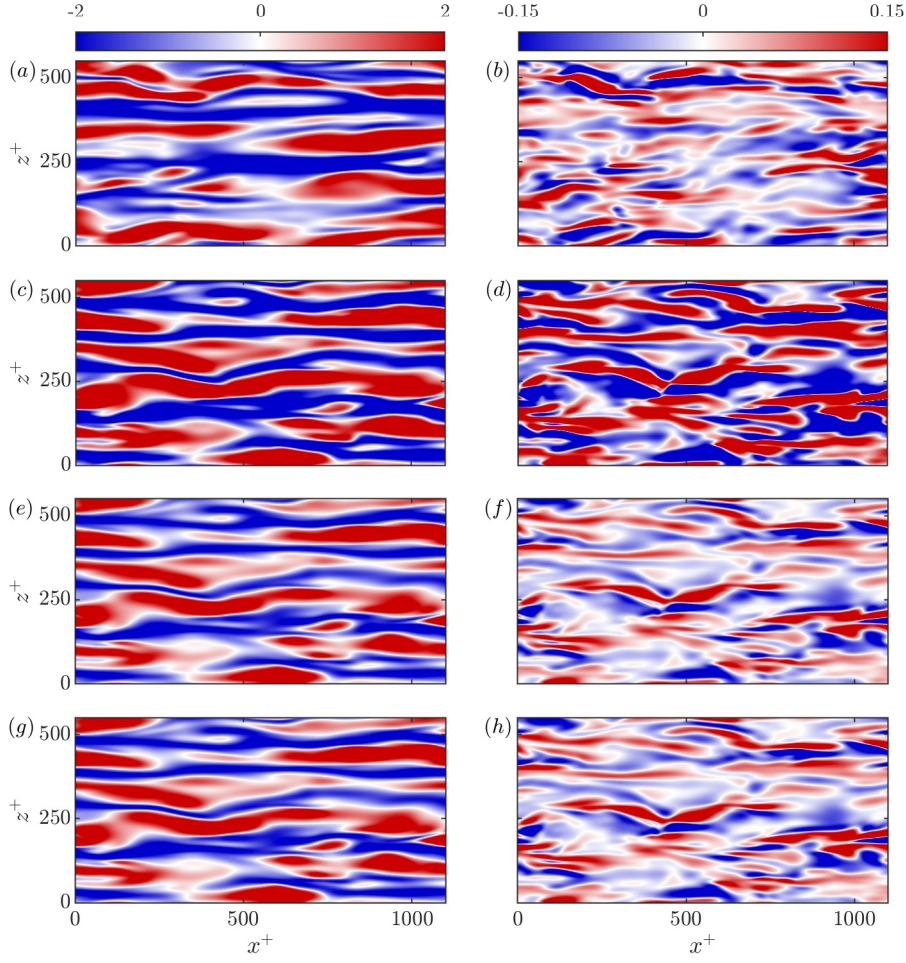


Figure 3.5 Streamwise (*a,c,e,g*) and wall-normal (*b,d,f,h*) instantaneous velocity fluctuation flow fields. (*a,b*) smooth-wall reference case at $y^+ = 5$, scaled with u_τ at $y^+ = 0$; (*c,d*) slip-length simulation UWV6 at $y^+ = 5$, scaled with u_τ at $y^+ = 0$; (*e,f*) the same snapshot as (*c,d*), but now for the wall-parallel plane $y^+ + \ell_T^+ = 5$, scaled with u_τ at the origin for turbulence, $y^+ = -\ell_T^+$; (*g,h*) as (*e,f*), but scaled with the friction velocity at the reference plane, $y^+ = 0$.

energy might be organized differently yet provide the same r.m.s. values. Figure 3.4 portrays the premultiplied energy spectra at $y^+ + \ell_T^+ = 15$ for several cases along with that of a smooth-wall flow at $y^+ \approx 15$. For cases UWV1–UWV6, shown in figure 3.4(*e–h*), the distribution of energy among different length scales is the same as in flows over a smooth wall, which supports the idea that the near-wall turbulence dynamics remain essentially smooth-wall-like. The same is true for cases V1, V2, UV1 and UV2, figure 3.4(*a–d*), which were discussed above and have $\ell_T^+ = 0$. Additionally, figure 3.5 compares snapshots of u'^+ and v'^+ for the flow over a smooth wall at $y^+ = 5$ with those for case UWV6 at two wall-parallel planes, $y^+ = 5$ and $y^+ + \ell_T^+ = 5$. The fluctuations at $y^+ = 5$ are portrayed in figures 3.5(*c,d*), and are scaled with u_τ measured at $y^+ = 0$. On the other hand, the fluctuations at $y^+ + \ell_T^+ = 5$, shown in figures 3.5(*e,f*), are

scaled with u_τ measured at $y^+ = -\ell_T^+$. The figure demonstrates that there is no qualitative visual change in the flow when the snapshots from the smooth-wall flow are compared to those from the slip-length simulation at the equivalent height, i.e. comparing the smooth-wall flow at $y^+ = 5$ with case UWV6 at $y^+ + \ell_T^+ = 5$, measuring u_τ accordingly. However, if the snapshots from the slip-length simulation are compared to the smooth-wall case at the same height above the reference plane $y^+ = 0$, using u_τ measured at $y^+ = 0$ in both cases as is often done in the literature, an apparent intensification of the fluctuations relative to the smooth-wall case can be observed, particularly for v'^+ , as shown in figures 3.5(c,d). Similar to the turbulence statistics presented in figure 3.2, we also show in figure 3.5(g,h) the snapshots from case UWV6 at $y^+ + \ell_T^+ = 0$, but scaled by the friction velocity at the reference plane, $y^+ = 0$. These snapshots are not qualitatively different to those in figure 3.5(e,f), again demonstrating that the most significant apparent change in the flow comes from the change in height origin perceived by turbulence, and the change in friction velocity (at most an increase of 2%) is only a minor effect. This further supports the idea that the near-wall turbulence dynamics remain essentially smooth-wall like, except for the shift of origin ℓ_T^+ . Case UWV6 is used as an example, because it has the deepest virtual origin for turbulence, $y^+ \approx -4$, and the effect is more pronounced, but the same can also be observed for cases UWV1–UWV5.

3.2 Separating the effect of the virtual origin experienced by the mean flow from that experienced by streamwise velocity fluctuations

In section 3.1, we observed for cases V1 and V2 that increasing ℓ_u^+ resulted in an increase in the maximum value of u'^+ and a deviation of its profile away from the smooth-wall data. This leads to the question of why this is the case, to what extent the peak will continue to increase on increasing ℓ_u^+ , and what effect this has on the flow beyond simply modifying u'^+ . More importantly, since this behaviour appears to occur independently of the mean flow, we also wish to address the question of whether or not the virtual origin perceived by the streamwise velocity fluctuations, and their apparent intensification, has any significant effect on ΔU^+ . To answer these questions, we carry out a series of simulations with no slip on the mean flow, i.e. $\ell_U^+ = 0$, and gradually increase the slip length applied to the streamwise fluctuations from $\ell_x^+ = 5$ to $\ell_x^+ = \infty$, the latter being equivalent to a free-slip condition. These are simulations UM1–UM6. They would highlight any effects caused by deepening the virtual origin experienced by the streamwise fluctuations. Results for these simulations are shown in figure 3.6. Note that the virtual origin experienced by the streamwise velocity fluctuations has no significant effect on the mean velocity profile, v'^+ , w'^+ or the Reynolds stress profile, even for an infinite slip length. This demonstrates that the streamwise fluctuations play a negligible role in setting the origin for turbulence, i.e. $\ell_T^+ = 0$, and $\Delta U^+ = 0$. The peak value of u'^+ increases with the streamwise

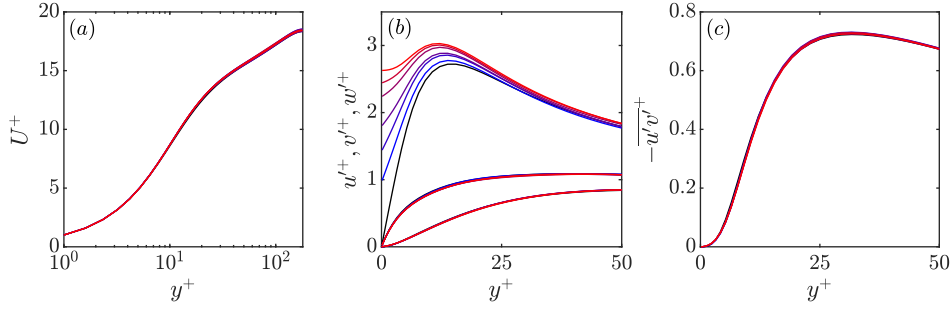


Figure 3.6 Mean velocity profiles, r.m.s. velocity fluctuations and Reynolds shear stress profiles for simulations with slip on the streamwise fluctuations but not on the mean flow, i.e. $\ell_{x,m}^+ = 0$. Black, smooth-wall reference data; blue to red, cases UM1–UM6 with increasing slip on the streamwise fluctuations.

slip, but, even when $\ell_x^+ = \infty$, is not much larger than the smooth-wall value. The y -location of this peak also does not change significantly. The gradual increase in the peak value is likely due to the greater y -range over which the streamwise fluctuations near the wall are brought to zero by viscosity. As ℓ_x^+ is increased, the streamwise fluctuations experience a deeper virtual origin and have more room to decay to zero more slowly. This changes the slope of u'^+ near the wall and results in the gradual increase observed in the peak value, but has no other effect on the turbulence. This can, again, be confirmed from the premultiplied energy spectra for these cases, given figure 3.4(*i–l*). Except for case UM6, the simulation with infinite slip, the spectra for all cases matches very well to the smooth-wall reference data. There are some deviations in the contours for case UM6, but the peak location and overall distribution of energy among length scales still remains essentially smooth-wall-like. It is perhaps surprising that the Reynolds stress, $-\overline{u'v'^+}$, exhibits no change at all, given that u'^+ changes quite noticeably near the wall. However, since v'^+ is so small in the immediate vicinity of the wall, and the shape of its profile remains unmodified, the change in the Reynolds stress is negligible.

The above behaviour can be discussed in terms of the near-wall-cycle structures (Hamilton et al., 1995; Waleffe, 1997). The quasi-streamwise vortices and streaks interact in a quasi-cyclic process in which the vortices act to sustain the streaks through sweeps and ejections of high- and low-speed fluid, respectively. In terms of the r.m.s. velocity fluctuations, the streaks are related to u'^+ , while the quasi-streamwise vortices generate mainly v'^+ and w'^+ . Since applying a slip length in the streamwise direction has no effect on the spanwise or wall-normal velocities, this means that the y -location of the quasi-streamwise vortices cannot change with respect to the domain boundary. If the vortices are unaffected, and the streaks are sustained by the vortices, there cannot, therefore, be a substantial change in the location or magnitude of the peak value of u'^+ . This would explain why the origin for turbulence seems to be independent of the origin for the streamwise velocity fluctuations, at least in the regime where $\ell_u^+ \geq \ell_T^+$.

So far, we have shown that applying a slip length to the streamwise flow appears to have an effect that is independent of the spanwise and wall-normal velocities. Further, applying a

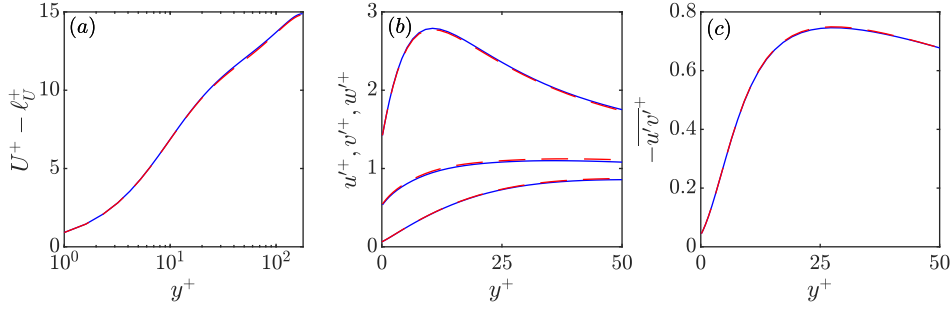


Figure 3.7 Mean velocity profiles, r.m.s. velocity fluctuations and Reynolds shear stress profiles for simulations UWV6 (blue lines) and UWV6M (red dashed lines), which have the same slip lengths applied to the velocity fluctuations but different slip lengths applied to the mean flow.

slip length to the streamwise fluctuations alone has no effect on the mean flow or the turbulent fluctuations other than the effect on u'^+ that has no further consequence discussed above. This suggests that the virtual origin experienced by the mean flow is independent of the virtual origin experienced by the streamwise fluctuations. The only streamwise origin relevant to ΔU^+ would therefore be that experienced by the mean flow, and not the origin experienced by the near-wall streaks, and the streaks appear not to play a significant role in determining the drag. We shall refer to this as the streaks being ‘inactive’ with respect to the change in drag. This is consistent with the idea proposed by Luchini (1996) that turbulence as a whole has one origin, and the other important origin is the one for the mean flow, as we discussed in section 3.1. We check this using simulations UWV6 and UWV6M, with the same set of slip-length coefficients for the fluctuating velocity components, but a different slip on the mean velocity. As shown in table 3.1, for the velocity fluctuations $(\ell_x^+, \ell_z^+, \ell_y^+) = (4.0, 6.0, 2.0)$ in both cases, but for the mean flow is $\ell_{x,m}^+ = 4.0$ and 10.0 , respectively. The statistics for these simulations are portrayed in figure 3.7. The figure shows that once ℓ_U^+ is subtracted from the mean velocity, the mean velocity profile and the other statistics portrayed are identical for both simulations. This demonstrates that if the mean flow experiences a virtual origin different from the one of the streamwise fluctuations, this causes no change to the turbulence itself. This is because the additional mean velocity in case UWV6M corresponds simply to a Galilean shift of the flow compared to case UWV6. In combination with the fact that changing the virtual origin perceived by the streaks has no effect on the drag, this confirms that the important parameter in determining ΔU^+ is ℓ_U^+ , and not ℓ_u^+ . Note that actual textures may not impose different virtual origins on the mean flow and the streamwise fluctuations, as is done in case UWV6M, but its comparison with case UWV6 demonstrates which streamwise origin is physically relevant to ΔU^+ , and hence the drag.

3.3 Predicting the origin for turbulence from the virtual origins experienced by the three velocity components

In the preceding discussion, we have shown that it is possible to displace the turbulence to its virtual origin at $y^+ = -\ell_T^+$ by imposing virtual origins for the three velocity components. We have demonstrated that the turbulence statistics and mean velocity profile essentially collapse to the smooth-wall data when rescaled by the friction velocity at $y^+ = -\ell_T^+$ and measured from that same height. Since we have shown that ℓ_u^+ has no effect on ΔU^+ , at least in the regime where $\ell_u^+ \geq \ell_T^+$, and that ℓ_U^+ has no effect on the origin perceived by the turbulence, it follows that ℓ_T^+ depends only on ℓ_v^+ and ℓ_w^+ . We have also observed that the resulting location of the origin for turbulence exhibits two distinct regimes, with respect to the virtual origins experienced by v and w . The first is when the virtual origin for v is deeper than or equal to the virtual origin for w , i.e. $\ell_v^+ \geq \ell_w^+$. With reference to table 3.1, if $\ell_v^+ \geq \ell_w^+$, then $\ell_T^+ \approx \ell_w^+$, which can be observed for cases V1, V2, UV1, UV2, UWV1, UWV2 and UWV4. The second regime occurs when the origin for w is deeper than the origin for v , i.e. $0 < \ell_v^+ < \ell_w^+$, for example, in cases UWV3, UWV5, UWV6 and UWV3H. We then find that turbulence perceives an origin intermediate between ℓ_v^+ and ℓ_w^+ , such that $\ell_v^+ < \ell_T^+ < \ell_w^+$. This is in agreement with the physical arguments presented in section 1.2. We now wish to infer an expression that can be used to predict the virtual origin for turbulence a priori from the virtual origins for v and w .

As a first step, we start from equation (1.7), which provides an expression for the effective spanwise slip length $\ell_{z,eff}^+$ in terms of the conventional slip length ℓ_z^+ (Fairhall and García-Mayoral, 2018). As discussed in section 1.2, equation (1.7) corresponds to the case with no permeability at the reference plane $y = 0$, i.e. $\ell_y = 0$, and that is why the effect of increasing the spanwise slip eventually saturates (see figures 1.5 and 1.6). Now, we are interested in finding an expression for ℓ_T^+ in terms of the virtual origins perceived by v and w , not the slip-length coefficients. Therefore, it would be more appropriate to express this saturation effect in terms of ℓ_w^+ rather than ℓ_z^+ . This would provide an expression for the virtual origin perceived by w , and hence the virtual origin perceived by turbulence, in the absence of transpiration, i.e. when $\ell_v^+ = 0$. Following Fairhall and García-Mayoral (2018), but now taking into account the curvature of the w'^+ profile, we revisit the expression for the effective spanwise slip (1.7), and arrive at the following empirical relation

$$\ell_{w,eff}^+ \approx \frac{\ell_w^+}{1 + \ell_w^+/5}, \quad (3.3)$$

which is analogous to (1.7) for ℓ_z^+ , but asymptotes to a value of 5 instead of 4. Figure 3.8 is an alternative portrayal of the data from Busse and Sandham (2012) presented earlier in figure 1.5(b), but this time using $\ell_{w,eff}^+$ instead of $\ell_{z,eff}^+$ to calculate ΔU^+ . The figure shows excellent agreement between ΔU^+ and the difference $\ell_x^+ - \ell_{w,eff}^+$, with the data for low $Re_{\tau,0}$

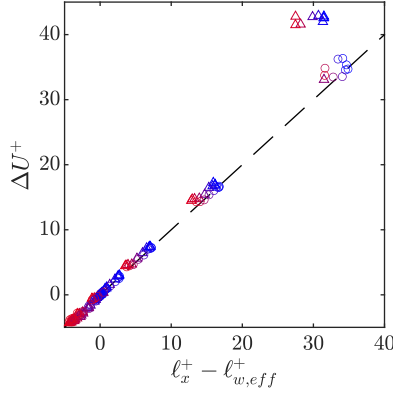


Figure 3.8 Alternative portrayal of the data from [Busse and Sandham \(2012\)](#) presented in figure 1.5(b), with ΔU^+ now a function of $\ell_x^+ - \ell_{w,eff}^+$. Triangles, simulations at $Re_{\tau,0} = 180$; circles, simulations at $Re_{\tau,0} = 360$. From blue to red, increasing $\ell_{w,eff}^+$. The dashed line represents $\Delta U^+ = \ell_x^+ - \ell_{w,eff}^+$.

and high ΔU^+ deviating again as discussed for figure 1.5(b). The results show that when $\ell_v^+ = 0$, equation (3.3) gives an accurate prediction for the origin for turbulence, $\ell_{T,pred}^+$.

The next step is to consider the effect of transpiration, i.e. $\ell_v^+ > 0$, in the regime where $\ell_w^+ > \ell_v^+$. In this case, $v > 0$ at the reference plane $y = 0$, and so (3.3) would no longer be valid. When $\ell_v^+ > 0$, the virtual origin perceived by v now lies below the reference plane, i.e. at $y^+ = -\ell_v^+$. This would delay the saturation in the effect of increasing ℓ_w^+ , because the quasi-streamwise vortices can move closer to the reference plane before being inhibited by the virtual, impermeable plane at $y^+ = -\ell_v^+$. Thus, $\ell_{T,pred}^+$ would be larger for a given ℓ_w^+ . It follows that, in general, the saturation in the effect of ℓ_w^+ should be evaluated with respect to the plane at which v appears to vanish, i.e. $y^+ = -\ell_v^+$, rather than $y^+ = 0$ ([Gómez-de-Segura et al., 2018a](#)). In other words, the virtual origin for turbulence would lie below the virtual origin for v by a height

$$\ell = \frac{(\ell_w^+ - \ell_v^+)}{1 + (\ell_w^+ - \ell_v^+)/5}. \quad (3.4)$$

This expression simply comes from replacing ℓ_w^+ on the right-hand side of (3.3) by $(\ell_w^+ - \ell_v^+)$, i.e. the distance between the virtual origins for w and v . Then, $\ell_{T,pred}^+$ would be given by

$$\ell_{T,pred}^+ \approx \ell_v^+ + \frac{(\ell_w^+ - \ell_v^+)}{1 + (\ell_w^+ - \ell_v^+)/5}. \quad (3.5)$$

This provides an expression for the predicted virtual origin for turbulence in the regime $0 < \ell_v^+ < \ell_w^+$. This regime is sketched in figure 3.9(a), where the virtual origin for turbulence lies between the virtual origins for v and w , with $\ell_v^+ < \ell_{T,pred}^+ < \ell_w^+$.

On the other hand, as demonstrated by [Gómez-de-Segura et al. \(2018a\)](#), if $\ell_v^+ \approx \ell_w^+$ then no saturation in the effect of ℓ_w^+ occurs and $\ell_{T,pred}^+ \approx \ell_w^+$, as sketched in figure 3.9(b). If we increase ℓ_v^+ further, such that $\ell_v^+ > \ell_w^+$, we would not expect the quasi-streamwise vortices to

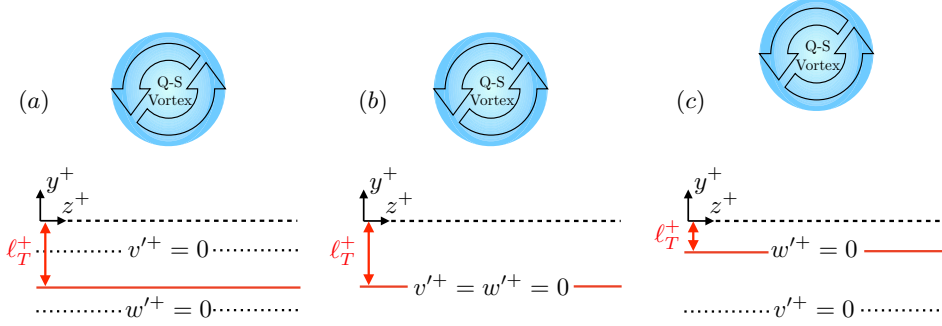


Figure 3.9 Schematics of the location of the origin for turbulence, $y^+ = -\ell_T^+$, when imposing different origins for the spanwise and wall-normal velocities. The planes where $v'^+ = 0$ and $w'^+ = 0$ correspond to the imposed virtual origins, $y^+ = -\ell_v^+$ and $y^+ = -\ell_w^+$, respectively. The origin for turbulence, $y^+ = -\ell_T^+$, is represented by the red line. (a) $\ell_v^+ < \ell_w^+$, (b) $\ell_v^+ = \ell_w^+$, (c) $\ell_v^+ > \ell_w^+$. Note that in each case, the distance between the centre of the quasi-streamwise vortices (Q-S Vortex) and the plane $y^+ = -\ell_T^+$ is the same.

approach the surface further, since their first-order effect is to induce a spanwise velocity at the reference plane. Even if v was allowed to penetrate freely through the reference plane, the quasi-streamwise vortices would require some amount of spanwise slip in the first place to approach this plane. Therefore, when $\ell_v^+ \geq \ell_w^+$, we would expect $\ell_T^+ \approx \ell_w^+$. This is confirmed in our simulations UWV1, UWV2, and UWV4. This regime is sketched in figure 3.9(c). Combining (3.5) and the preceding argument for the regime where $\ell_v^+ \geq \ell_w^+$, a general expression for approximating ℓ_T^+ from ℓ_w^+ and ℓ_v^+ would be

$$\ell_{T,pred}^+ \approx \begin{cases} \ell_v^+ + \frac{(\ell_w^+ - \ell_v^+)}{1 + (\ell_w^+ - \ell_v^+)/5} & \text{if } \ell_w^+ > \ell_v^+, \\ \ell_w^+ & \text{if } \ell_w^+ \leq \ell_v^+. \end{cases} \quad (3.6)$$

When $\ell_{T,pred}^+$ is predicted from the values of ℓ_v^+ and ℓ_w^+ , which are known a priori from ℓ_y^+ and ℓ_z^+ , it shows excellent agreement with the value of ℓ_T^+ measured a posteriori for the cases presented thus far, as shown in table 3.1. In all these cases, ΔU^+ is given by the linear law (3.1), that is, the difference $\ell_U^+ - \ell_T^+$.

A key point epitomised by (3.6) is that the only relevant parameters are the relative positions of the virtual origins of u and w relative to the plane where v appears to vanish. The classical understanding, as first proposed by Luchini et al. (1991), is that the only relevant parameter is the difference between streamwise and spanwise protrusion heights. However, the results of Busse and Sandham (2012) show that this is not the case. We argue that the plane where v appears to vanish (or alternatively, how much the flow can transpire through the reference plane from which the tangential virtual origins are measured) is also important. The result is an extension of Luchini's theory where, rather than on the difference between the virtual

origins perceived by the tangential velocities, ΔU^+ depends on their positions relative to that perceived by the wall-normal velocity, regardless of the plane taken as reference.

3.4 Scaling with Reynolds number and domain size

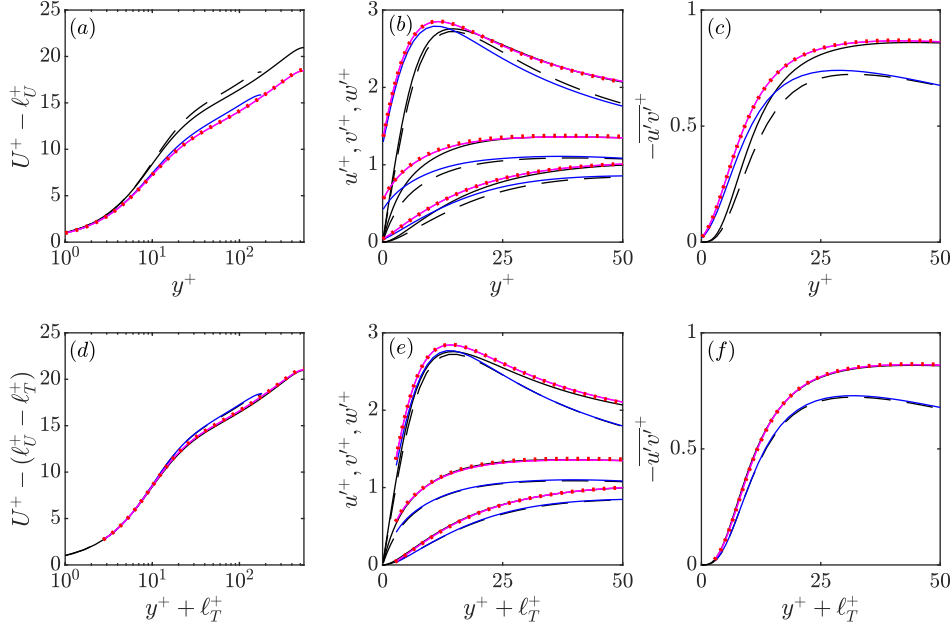


Figure 3.10 Mean velocity profiles, r.m.s. velocity fluctuations and Reynolds shear stress profiles for slip-length simulations UWV3, UWV3H and UWV3HD. These simulations have the same virtual origins, in wall units, for each velocity component, $(\ell_u^+, \ell_w^+, \ell_v^+) = (3.6, 2.9, 1.9)$, but UWV3 is conducted at $Re_\tau \simeq 180$, whereas UWV3H and UWV3HD are conducted at $Re_\tau \simeq 550$. UWV3HD has a larger domain size in the wall-parallel directions, $8\pi \times 3\pi$ instead of $2\pi \times \pi$. (a–c), scaled with the friction velocity at the reference plane, $y^+ = 0$; (d–f) shifted in y^+ by ℓ_T^+ and scaled with the friction velocity at the origin for turbulence, $y^+ = -\ell_T^+$. Smooth-wall reference data is portrayed at (---) $Re_\tau \simeq 180$ and (—) $Re_\tau \simeq 550$; —, case UWV3; —, case UWV3H; ···, case UWV3HD.

As discussed in section 1.2, the universal parameter for quantifying the performance of drag-reducing surfaces is ΔU^+ . The idea is that so long as the texture size of a given surface, L^+ , is fixed in wall units, then so would be ℓ_u^+ , ℓ_v^+ and ℓ_w^+ , and ΔU^+ should remain essentially independent of Re_τ . In our simulations, we impose different virtual origins on each velocity component, ℓ_u^+ , ℓ_v^+ and ℓ_w^+ , and so we wish to determine whether this effect scales in wall units for varying Reynolds numbers. To verify this, we conduct two simulations at different Reynolds numbers, $Re_\tau = 180$ and 550 , but keep the virtual origins constant in wall units, see cases UWV3 and UWV3H in table 3.1. For the two cases considered here, the slip lengths ℓ_x^+ , ℓ_y^+ and ℓ_z^+ are identical for both Reynolds numbers. Note that, in general, this will not necessarily be the case, since the one-to-one a priori relationship discussed in section 2.2 between the Robin slip-length coefficients in equation (2.4), ℓ_x^+ , ℓ_y^+ and ℓ_z^+ , and the resulting virtual origins, ℓ_u^+ , ℓ_v^+ and ℓ_w^+ , will slightly change with the Reynolds number. However, these differences are

consistent with the change in the turbulence statistics over a smooth wall as a result of varying the Reynolds number (see e.g. Moser et al., 1999), as shown figure 3.10. After shifting the mean velocity profile and r.m.s. velocity fluctuations by ℓ_T^+ and rescaling them by the friction velocity at $y^+ = -\ell_T^+$, they essentially collapse to the smooth-wall data. For both Reynolds numbers, the value of $\Delta U^+ = \ell_U^+ - \ell_T^+$ measured a posteriori is 1.3 (see table 3.1), indicating that ΔU^+ is indeed independent of the Reynolds number for fixed values of the virtual origins ℓ_u^+ , ℓ_v^+ and ℓ_w^+ in wall units. However, the measured drag reduction, DR , varies between the two cases, as expected. From (1.4), DR is smaller at higher Re_τ , due to the increase in $U_{\delta_0}^+$ with Re_τ , even though we observe no change in ΔU^+ .

Our simulation domains, $2\pi \times \pi$, are sufficiently large to capture the key turbulence processes and length scales of the near-wall and log-law regions of the flow Lozano-Durán and Jiménez (2014), but scales larger than this will be unresolved. To verify that virtual origins interact only with the smaller scales that reside near the wall, we conduct an additional simulation at $Re_\tau \simeq 550$, UWV3HD, with the same parameters as UWV3H but a domain size $8\pi \times 3\pi$. The results shown in figure 3.10 are indistinguishable, suggesting that the origin-offset mechanism does not interact with the larger, outer turbulence scales, other than by the shift in origin.

3.5 Departure from smooth-wall-like turbulence

The fundamental idea behind the proposed virtual-origin framework is that when we impose virtual origins on each velocity component, we assume that the shape of each r.m.s. velocity profile remains smooth-wall-like independently of the others, as explained in section 2.2. For this assumption to hold, the near-wall turbulence cycle should be left essentially unaltered. Otherwise, these profiles will no longer be smooth-wall-like. As a guide, we can say that the virtual origins should be smaller than the smallest eddies of near-wall turbulence. As discussed in section 2.2, this would be the quasi-streamwise vortices, with diameter and distance to the surface both of order 15 wall units (Robinson, 1991; Schoppa and Hussain, 2002). This would then serve as a rough limit for the applicability of this framework. The cases presented thus far have all been within this regime, and we have demonstrated that the flow remained essentially smooth-wall-like, once the virtual origin for turbulence, ℓ_T^+ , was accounted for. It was also possible to predict ℓ_T^+ from the virtual origins a priori.

To better understand the limits of this framework, we conduct a series of simulations where the imposed virtual origins are relatively large, e.g. up to $\ell_u^+, \ell_w^+ \approx 6$ and $\ell_v^+ \approx 11$. These are cases UWVL1–UWVL4, and their mean velocity profiles, r.m.s. velocity fluctuations and Reynolds stress profiles are shown in figure 3.11. We see that when the imposed virtual origins become too large, the r.m.s. velocity fluctuations and Reynolds stress profile no longer remain smooth-wall-like. In these cases, as we increase the depth of the virtual origins, specifically for v and w , the quasi-streamwise vortices approach the reference plane $y^+ = 0$ to such an extent

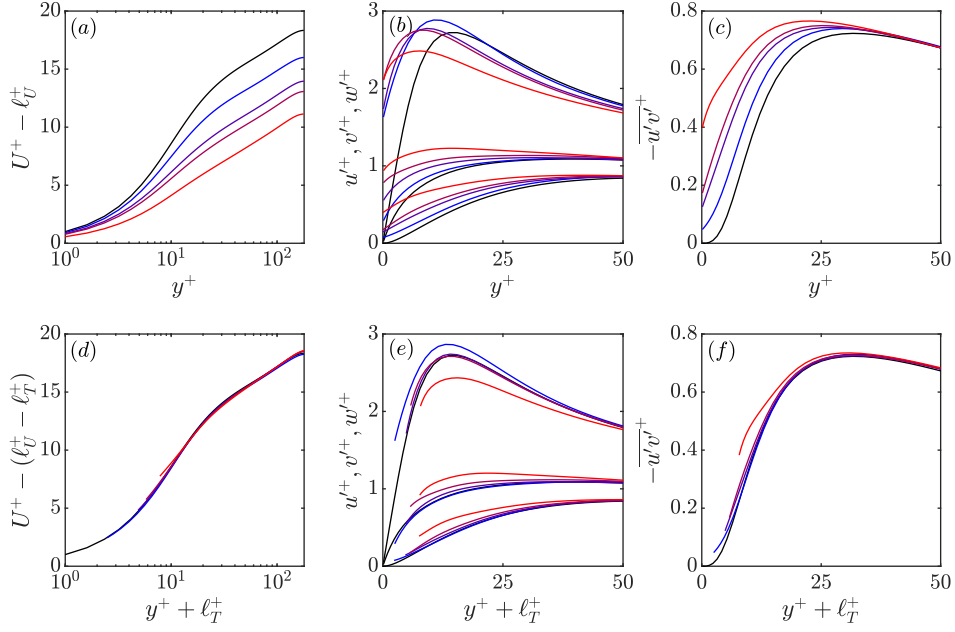


Figure 3.11 Mean velocity profiles, r.m.s. velocity fluctuations and Reynolds shear stress profiles for simulations with slip-length boundary conditions applied to all three velocity components. Here, the values of the slip-length coefficients are relatively large, e.g. up to $\ell_x^+, \ell_y^+, \ell_z^+ \approx 10$. (a–c) scaled with the friction velocity at the reference plane, $y^+ = 0$; (d–f) shifted in y^+ by ℓ_T^+ and scaled with the friction velocity at $y^+ = -\ell_T^+$. Black lines, smooth-wall reference data; blue to red lines, cases UWVL1–UWVL4.

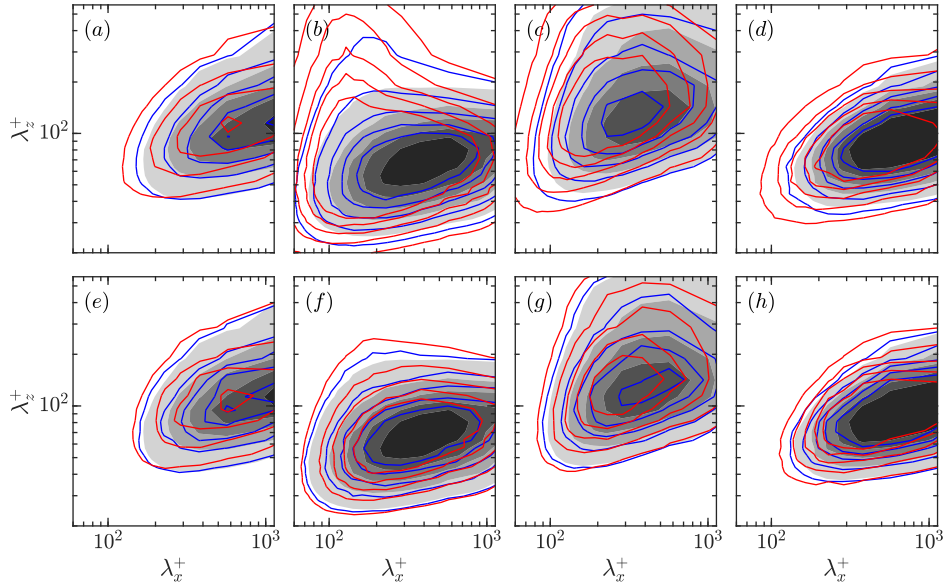


Figure 3.12 Premultiplied two-dimensional spectral densities of u^2 , v^2 , w^2 and uv at $y^+ + \ell_T^+ = 15$, normalised by u_τ at $y^+ = -\ell_T^+$, for various slip-length simulations (line contours), compared to smooth-wall data (filled contours) at $y^+ = 15$. The shift ℓ_T^+ is given in table 3.1 for each case. (a–d) cases UWVL1 and UWVL4, with line colours as in figure 3.11. (e–h) cases WV1 and WV3, with line colours as in figure 3.14. First column, $k_x k_z E_{uu}^+$; second column, $k_x k_z E_{vv}^+$; third column, $k_x k_z E_{wv}^+$; fourth column, $-k_x k_z E_{uv}^+$. The contour increments for each column are 0.3224, 0.0084, 0.0385 and 0.0241, respectively.

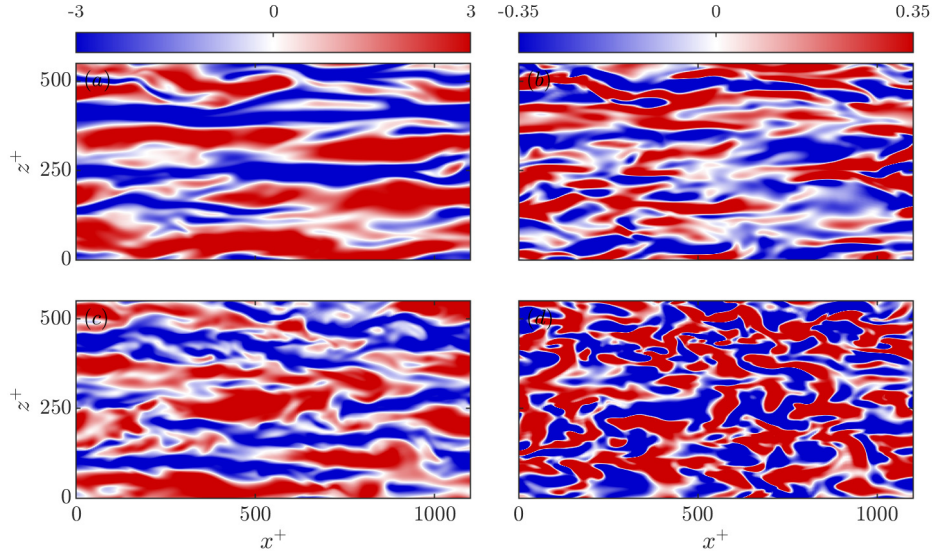


Figure 3.13 Streamwise (*a,c*) and wall-normal (*b,d*) instantaneous velocity fluctuation flow fields. (*a,b*) smooth-wall reference case at $y^+ = 15$, scaled with u_τ at $y^+ = 0$; (*c,d*) slip-length simulation UWVL4 at $y^+ + \ell_T^+ = 15$, scaled with u_τ at $y^+ = -\ell_T^+$.

that they are, in fact, ingested by the domain boundary. The whole near-wall cycle is then fundamentally disrupted, changing the nature of the flow near the wall. This is most apparent for cases UWVL3 and UWVL4. The premultiplied energy spectra for these cases, shown in figure 3.12(*a–d*), indicate that there can be a dramatic change in the distribution of energy among length scales, compared to the smooth-wall case, when the imposed virtual origins are large. For example, in case UWVL4 there is a significant redistribution of energy in the wall-normal velocity to larger spanwise and shorter streamwise wavelengths. This also occurs when the transpiration triggers the appearance of Kelvin–Helmholtz-like spanwise rollers (see e.g. [García-Mayoral and Jiménez, 2011b](#); [Gómez-de-Segura and García-Mayoral, 2019](#)) or in the presence of roughness large enough to disrupt the near-wall cycle ([Abderrahaman-Elena et al., 2019](#)). This increased spanwise coherence of v'^+ can also be observed in the snapshots of case UWVL4, which are compared to those of the smooth-wall reference case in figure 3.13. A similar behaviour was also observed by [Gómez-de-Segura et al. \(2018a\)](#) when using a Stokes-flow model for the virtual layer of flow below $y^+ = 0$, rather than the Robin slip-length boundary conditions used here.

The results of cases UWVL1–UWVL4, suggest that the virtual-origin framework holds only for $\ell_T^+ \lesssim 5$. Beyond this point, the Reynolds stress profiles presented in figures 3.11(*c,f*) indicate that the near-wall turbulence is no-longer smooth-wall-like, and the underlying assumptions of the framework are no longer valid. As discussed above, the origin for turbulence, ℓ_T^+ , should depend only on ℓ_v^+ and ℓ_w^+ . Note, however, that it is more difficult to impose limits on ℓ_w^+ and ℓ_v^+ independently, because both spanwise slip and transpiration are required to increase ℓ_T^+ beyond 5 wall units, as encapsulated by (3.6). For very large spanwise slip lengths without

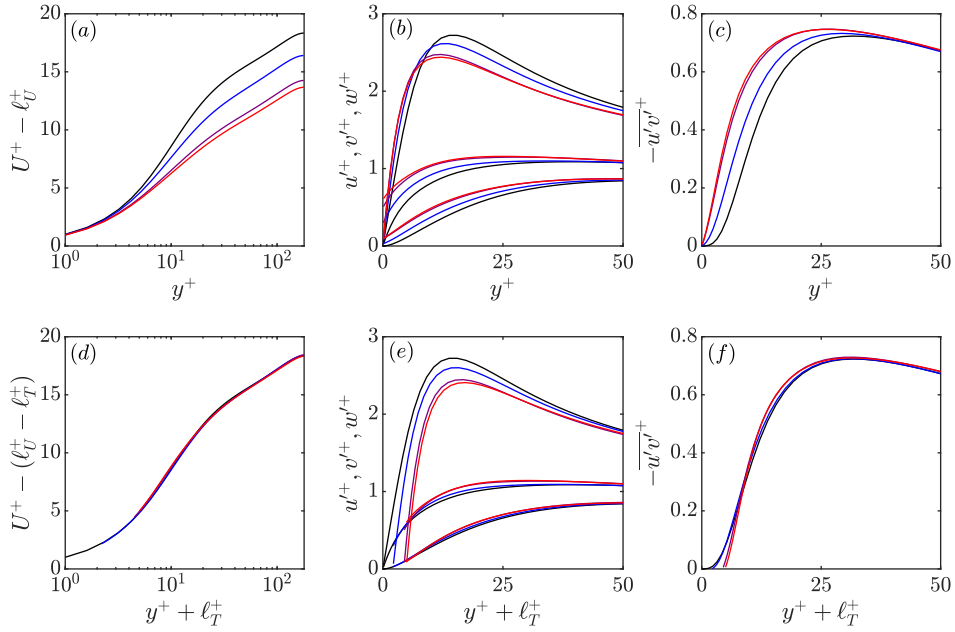


Figure 3.14 Mean velocity profiles, r.m.s. velocity fluctuations and Reynolds shear stress profiles for simulations with slip-length boundary conditions applied to the spanwise and wall-normal velocity components only. (a–c) scaled with the friction velocity at the reference plane, $y^+ = 0$; (d–f) shifted in y^+ by ℓ_T^+ and scaled with the friction velocity at $y^+ = -\ell_T^+$. Black lines, smooth-wall reference data; blue to red lines, cases WV1–WV3.

transpiration (e.g. [Busse and Sandham, 2012](#)), the virtual-origin framework still holds, and a saturation in the effect of ℓ_z^+ is observed, as discussed in section 1.2. In turn, as we have seen in cases V1, V2, UV1 and UV2, increasing ℓ_v^+ beyond ℓ_w^+ bears no consequence on ℓ_T^+ , no matter how large ℓ_v^+ .

The cases considered so far satisfy $\ell_u^+ \gtrsim \ell_T^+$, i.e. the streaks perceive a virtual origin at least as deep as that perceived by the quasi-streamwise vortices. In this regime, as discussed section 3.2, the streamwise fluctuations have a greater y -range in which they are brought to zero by viscosity, as shown in figure 3.6, but otherwise the quasi-streamwise vortices and the turbulence remain smooth-wall like. There is sufficient room for the near-wall-cycle structures to reside, and no change in the turbulence dynamics is observed. In contrast, we now consider the opposite regime, where $\ell_u^+ < \ell_T^+$. This would arguably be the case of interest for roughness, and has been shown to be the case when roughness is sufficiently small ([Abderrahaman-Elena et al., 2019](#)). We fix the origin for the streamwise velocity at $y^+ = 0$, i.e. $\ell_u^+ = 0$, and progressively increase the depth of the origin for turbulence below this plane, i.e. $\ell_T^+ > 0$. As portrayed in figure 3.14, for cases WV1–WV3, we then observe a gradual departure from smooth-wall-like turbulence. Note that $\ell_v^+ < \ell_T^+$ in these cases, and so $\Delta U^+ < 0$, which would correspond to an increase in drag. Case WV1, with $\ell_T^+ \approx 2$, appears to be the limiting case, in which turbulence still remains essentially smooth-wall-like, as can be observed in figure 3.14(d–f), and $\ell_{T,pred}^+$, calculated from equation (3.6), still provides a reasonable estimate for the origin for turbulence,

as shown in table 3.1. However, increasing ℓ_T^+ further results in clear differences between the r.m.s. velocity fluctuations and Reynolds stress profiles compared to the smooth-wall data. This can also be seen in the premultiplied energy spectra shown in figure 3.12(e–h), where the distribution of energy among length scales is no longer smooth-wall-like. For example, the spectra of case WV3 indicates that the energy in the streamwise and spanwise velocity components is now shifted, on average, to shorter streamwise wavelengths. Schematically, the quasi-streamwise vortices would approach the reference plane, but the streaks would be constrained by the condition that $u'^+ = 0$ at $y^+ = 0$. The streaks, which are sustained by the vortices, would then no longer have sufficient room to reside above $y^+ = 0$, compared to the flow over a smooth wall, and would become squashed in y and weakened. This, in turn, would restrict the whole near-wall turbulence dynamics, and cause the flow not to remain smooth-wall-like. From our simulations, this breakdown appears to occur when the virtual origin for turbulence is more than approximately 2 wall units deeper than the origin perceived by the streaks. Therefore, an additional constraint on the present virtual-origin framework would be that the imposed virtual origins should satisfy $\ell_T^+ \lesssim \ell_u^+ + 2$. This is in agreement with the observation in Abderrahaman-Elena et al. (2019) that a virtual-origin framework alone cannot capture the effect of roughness on the flow once the roughness size is large enough that $\Delta U^+ \simeq -2$. Further, it highlights the limitations of modelling the effects of drag-increasing surfaces, such as roughness, with virtual origins alone.

The breakdown of the virtual-origin framework and the subsequent departure from smooth-wall-like turbulence require further discussion. The homogeneous slip-length boundary conditions (2.4) are an approximation of the apparent boundary conditions that real textured surfaces impose on the flow. They are a reasonable model so long as the characteristic texture size is small compared to the length scales of the turbulent eddies in the flow (García-Mayoral et al., 2019). As the texture size, L^+ , is increased, we expect the apparent virtual origins that a given surface imposes on the flow to become deeper. However, on increasing L^+ further, flows over real textured surfaces eventually exhibit additional dynamical mechanisms, typically drag-degrading, such that the effect of the texture can no longer be approximated by a simple virtual-origin model. For example, as L^+ increases for superhydrophobic surfaces, the flow begins to perceive the texture as discrete elements, as opposed to a homogenised effect (Seo and Mani, 2016; Fairhall et al., 2019), and the entrapped gas pockets can also be lost (Seo et al., 2018), both of which fundamentally change the apparent boundary conditions imposed by the surface on the flow. For riblets, in turn, increasing the texture size can trigger the onset of Kelvin–Helmholtz-like rollers, which can have a strong drag-increasing effect on the flow (García-Mayoral and Jiménez, 2011b). Importantly, the depth of the virtual origin for turbulence at which the present framework breaks down, i.e. $\ell_T^+ \approx 5$, could imply a texture size that would place a corresponding real surface in a regime beyond the onset of the failure mechanisms just mentioned. For instance, the onset of the Kelvin–Helmholtz-like instability in riblets can occur for $\ell_T^+ \gtrsim 1$ (García-Mayoral and Jiménez, 2011b). In this case, the limits

| Case | $y_d^+/2$ | ℓ_U^+ | ℓ_w^+ | ℓ_v^+ | $\ell_{T,pred}^+$ | $\ell_U^+ - \ell_{T,pred}^+$ | ΔU^+ |
|-------------------|-----------|------------|------------|------------|-------------------|------------------------------|--------------|
| v control | 3.9 | 0.0 | 0.0 | -3.9 | -1.7 | 1.7 | 1.9 |
| w control | 3.9 | 0.0 | -3.9 | 0.0 | -3.9 | 3.9 | 3.0 |
| w - v control | 3.9 | 0.0 | -3.9 | -3.9 | -3.9 | 3.9 | 3.7 |

Table 3.2 Summary of opposition control simulations. For each case, the notional virtual origins are given with respect to the reference plane $y^+ = 0$, assuming that the control establishes a virtual origin for the opposed velocity components at $y^+ = y_d^+/2$, where y_d^+ is the detection plane height. The predicted virtual origin for turbulence, $\ell_{T,pred}^+$, is given, which is calculated from (3.6). The difference $\ell_U^+ - \ell_{T,pred}^+$ represents the predicted shift in the mean velocity profile, and ΔU^+ is the measured shift in the mean velocity profile from figure 3.15.

imposed by the operating window of the real surface are the most restrictive, and not the theoretical limits of the virtual-origin framework. Therefore, if the goal of a given simulation is to use virtual origins to model the effect on the flow of a real surface, it is crucial to keep in mind the texture size, and hence the magnitude of the virtual origins, at which the flow no longer perceives the surface in a homogenised fashion. This could, in many instances, be the actual limit up to which the virtual-origin framework can be feasibly applied.

3.6 Active opposition control interpreted in a virtual-origin framework

As we mentioned in section 1.2, the findings of the original study on opposition control by Choi et al. (1994) suggest that the effect of the control was to cause an outward shift of the origin for turbulence with respect to the mean flow. This is precisely the idea behind the present virtual-origin framework, captured by (3.1). We now assess if we can also explain the effect of opposition control on the flow with a virtual-origin framework.

We conduct three opposition-control simulations, controlling v alone, w alone, and both v and w . The detection plane in our simulations is set at $y_d^+ \approx 8$, with the aim of generating notional virtual origins for the controlled velocities at $y^+ \approx 4$, similar to our virtual-origin simulation UWV6. This is summarised in table 3.2. Raw results of the simulations are shown in figures 3.15(a-c), where, as expected, we observe an outward shift in the turbulence statistics away from the domain boundary (Choi et al., 1994). We then measure the virtual origin for turbulence, ℓ_T^+ , a posteriori, using the method outlined in section 3.1, and rescale the data with respect to the friction velocity at that origin, from equation (3.2). The results shifted in y^+ by ℓ_T^+ are included in figures 3.15(d-f). Note that, for these cases, the origin for the mean flow is at the reference plane $y^+ = 0$, i.e. $\ell_U^+ = 0$, and so $\Delta U^+ = -\ell_T^+$, from (3.1). The excellent collapse of the turbulence statistics in figure 3.15(d-f) indicates that the effect of this active control technique is to cause an outward shift of the origin for turbulence away from the origin for the mean flow, and that turbulence does, indeed, remain smooth-wall-like except for this

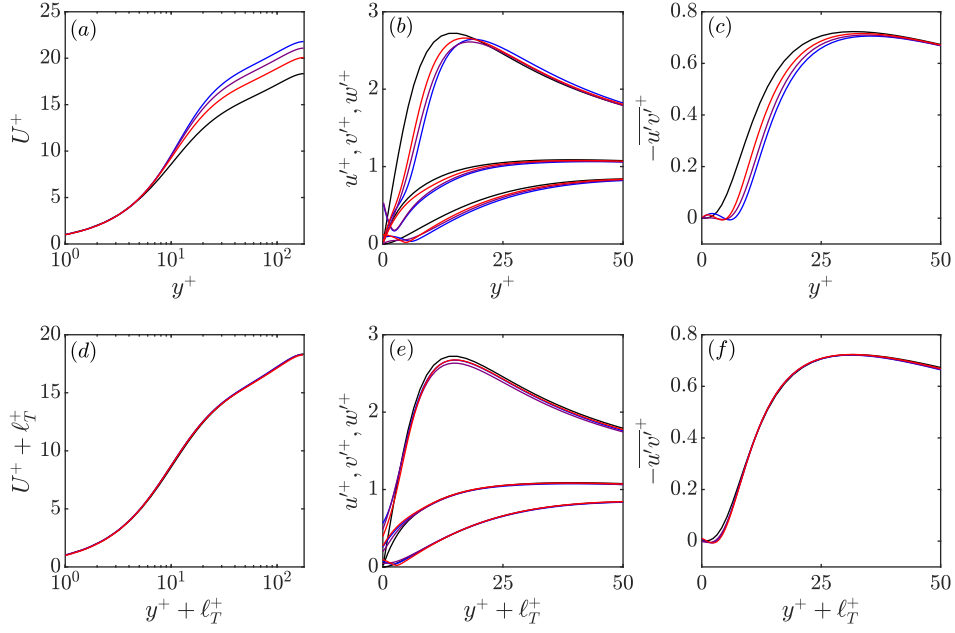


Figure 3.15 Mean velocity profiles, r.m.s. velocity fluctuations and Reynolds shear stress profiles for simulations with opposition control on w and v (in various combinations), with the sensing plane at $y_d^+ = 7.8$. (a–c) scaled with the friction velocity at the reference plane, $y^+ = 0$; (d–f) shifted in y^+ by ℓ_T^+ and scaled with the friction velocity at the origin for turbulence, $y^+ = -\ell_T^+$. Note that in these cases, $\ell_T^+ < 0$ and therefore the origin for turbulence is above the plane $y^+ = 0$. Black lines, smooth-wall reference data; blue to red lines, w - v control, w control and v control.

shift of origin. This suggests that it might be possible to consolidate the effect on the flow of other a wide variety of passive textures and active-control techniques in terms of a relative displacement of the virtual origin for turbulence and the virtual origin perceived by the mean flow, with the turbulence remaining otherwise smooth-wall-like.

While we have shown that for opposition control it is possible to find a shift in the origin for turbulence, ℓ_T^+ , that results in a collapse of the turbulence statistics to the smooth-wall profiles, we now wish to see if it is possible to predict ℓ_T^+ (and ΔU^+) from the virtual origins perceived by the three velocity components, as we did for the slip-length simulations in section 3.3. First we establish where each velocity component would notionally perceive a virtual origin when the control is applied. Based on the discussion in section 1.2, we assume that this would be the plane $y^+ = y_d^+/2$ for controlled velocity components, and $y^+ = 0$ for uncontrolled ones. In our slip-length simulations, in contrast, the apparent virtual origins were always at or below the domain boundary, e.g. at $y^+ = -\ell_w^+$, where $\ell_w^+ \geq 0$. We retain the same nomenclature here, but now the sign of the virtual origins would be reversed, e.g. $\ell_w^+ \leq 0$. For instance, in the case of w - v control, the virtual origin perceived by the mean flow would be the domain boundary $y^+ = 0$, while the virtual origins perceived by v and w would be the plane $y^+ = 3.9$, yielding $\ell_U^+ = 0$ and $\ell_v^+ = \ell_w^+ = -3.9$.

The notional virtual origins for all three cases are included in table 3.2, along with the virtual origin for turbulence, predicted from their values using (3.6). The shift ΔU^+ that these virtual origins would produce is also given in the table as the difference $\ell_U^+ - \ell_{T,pred}^+$ and compared to the shift ΔU^+ measured from figure 3.15. In the case of v control and v - w control, the predicted ΔU^+ agrees well with the measured one, but this is less so in the case of w control. The discrepancy between the predicted and measured ΔU^+ , particularly in the case of w control, could be caused by the control not successfully establishing a virtual origin for w exactly halfway between the domain boundary and the detection plane. In fact, it appears to do so at some height below $y_d^+/2$. Note that in the present virtual-origin framework, the depth of the virtual origin perceived by w , i.e. ℓ_w^+ , is set a priori, assuming that the shape of its r.m.s. velocity profile remained smooth-wall-like. However, the resulting apparent origin for w , as measured a posteriori, is not necessarily at $y^+ = -\ell_w^+$. Instead, as we argue in section 3.1, the virtual origin perceived by the whole turbulence dynamics, and thus w , would be $y^+ = -\ell_T^+$, as can be appreciated for instance in figure 3.2(e). As such, ℓ_w^+ cannot be measured a posteriori from the r.m.s. profiles of the resulting flow, as only ℓ_T^+ can. Nevertheless, from the resulting value of ΔU^+ in the case of w control, and the idea that the virtual origin perceived by w appears to be the most limiting in terms of setting the virtual origin for turbulence, we deduce that the results are consistent with applying a priori $\ell_w^+ \approx -3$, instead of the notional value of -3.9 . In addition, it can be observed from figure 3.15(b) that the profile of v'^+ is also modified indirectly by the control of w near the wall, suggesting that $\ell_v^+ \neq 0$, even though v is not controlled directly. This highlights one of the key differences between the slip-length and opposition-control simulations. In the slip-length simulations, the virtual flow does not have to satisfy the incompressible Navier–Stokes equations below the plane in which the slip-length boundary conditions are applied, $y^+ = 0$. When the virtual origins are imposed, we simply assume that the r.m.s. velocity profiles extend below $y^+ = 0$ in a smooth-wall-like fashion but independently for each velocity component. This is in contrast to opposition control, where the flow must still satisfy continuity and the Navier–Stokes equations from the domain boundary up to the height of any virtual origin perceived by the flow, e.g. for $0 \leq y^+ \leq -\ell_w^+$ for w control. The underlying coupling between the three velocity components, and thus between their virtual origins, makes it difficult for our Robin-based framework to establish their locations a priori when a given velocity component is controlled, and therefore it is not always possible to predict accurately the origin for turbulence a priori. This area grants further research, but in any event it is worth noting that the underlying physical mechanism at play appears to be the same in both the opposition-control and the slip-length simulations. That is, each velocity component perceives a different apparent virtual origin, and this reduces further to a virtual origin perceived by the mean flow and a virtual origin perceived by turbulence. Then, if the virtual origin for the mean flow is deeper than the virtual origin for turbulence, the shift in the mean velocity profile ΔU^+ is simply given by the height difference between the two, from (3.1), and the turbulence above remains otherwise smooth-wall-like. This also illustrates that the

virtual origin for turbulence, even if determined by v and w , may not always follow (3.6), but only when the effect of the control reduces to three different apparent velocity origins that can be imposed through Robin boundary conditions.

For the interested reader, mean velocity profiles from the original v - and w -control simulations of Choi et al. (1994) are interpreted in the virtual-origin framework in appendix A.1.

3.7 An eddy-viscosity model

The work presented in this section was done in collaboration with Prof Daniel Chung, of the University of Melbourne, who conceived the original idea and carried out most of the analysis. It is included here for completeness, since it forms a part of the study on virtual origins in this chapter, and was published alongside it in Ibrahim et al. (2021).

In this section, we present a simple model that captures the dependence of ΔU^+ on ℓ_U^+ and ℓ_T^+ (3.1). For the smooth wall, we can approximate the turbulent mean velocity profile $U_{sm}^+(y^+)$ using an eddy-viscosity model for the Reynolds shear stress $-\overline{u'v'^+} = (\nu_T/\nu)dU_{sm}^+/dy^+$ (e.g. van Driest, 1956), where $\nu_T(y^+)$ is the eddy viscosity representing turbulence. We will use $\nu_T^+(y^+)$ to refer to the normalised eddy viscosity $\nu_T(y^+)/\nu$. For channel flow, the total shear stress is linear:

$$\frac{dU_{sm}^+}{dy^+} - \overline{u'v'^+} = (1 + \nu_T^+) \frac{dU_{sm}^+}{dy^+} = 1 - \frac{y^+}{Re_\tau}. \quad (3.7)$$

Two possible models for ν_T^+ are those of van Driest (1956) and Cess (cf. Reynolds and Tiederman, 1967). The key difference between the two is that van Driest's model does not include the contribution from the wake, and so is only valid when $y/\delta \ll 1$. In this chapter, since the focus is on the near-wall region of the flow, we choose to use van Driest's model for its relative simplicity. Noting that $y^+/Re_\tau = y/\delta$, the total stress in (3.7) becomes nearly uniform in the near-wall region, so we can write (van Driest, 1956):

$$\frac{dU_{sm}^+}{dy^+} \approx f(y^+) = \frac{1}{1 + \nu_T^+(y^+)}, \quad (3.8)$$

with

$$\nu_T^+(y^+) = \frac{1}{2} \left\{ 1 + 4\kappa^2 y^{+2} \left[1 - \exp\left(-\frac{R(y^+)}{A_d}\right) \right]^2 \right\}^{1/2} - \frac{1}{2}. \quad (3.9)$$

Here, $\kappa \approx 0.426$ and $A_d \approx 25.4$ (cf. Reynolds and Tiederman, 1967; del Álamo et al., 2006), and $R(\cdot) \equiv \max(\cdot, 0)$ is the ramp function to ensure that the damping factor in the square brackets remains between 0 and 1 (in practice, the ramp function is regularised with $R(\cdot) = \log[1 + \exp(\cdot)]$). The damping coefficient A_d sets the thickness of the laminar sublayer by damping the contribution from turbulence just above the smooth wall, and thus also sets the

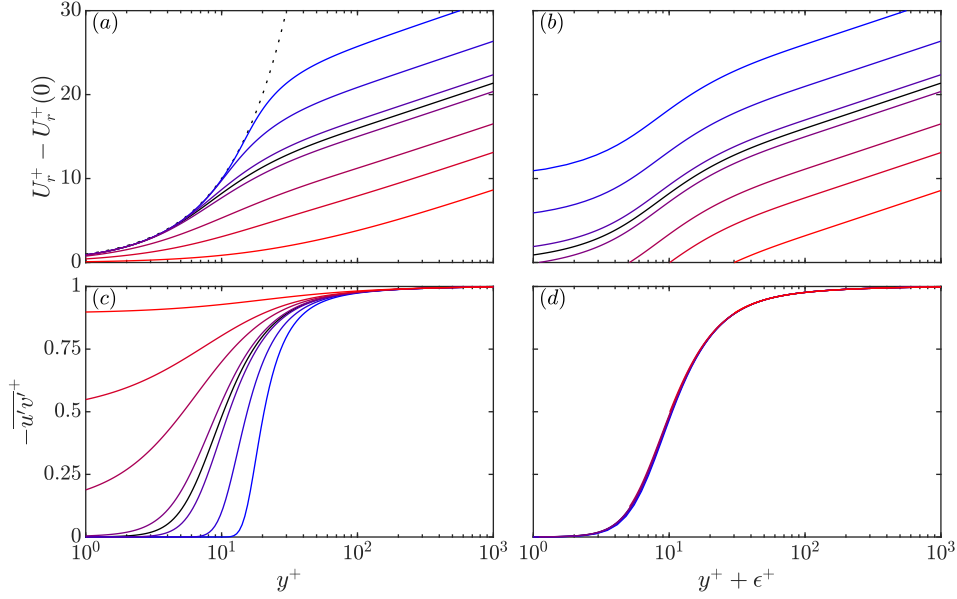


Figure 3.16 Profiles of mean velocity U_r^+ from (3.11) (a,b) and Reynolds shear stress $-\overline{u'v'}^+ = (\nu_T/\nu)dU_r^+/dy^+$ (c,d), plotted relative to the origin for the mean streamwise flow y^+ (a,c) and relative to the origin for turbulence $y^+ + \epsilon^+$ (b,d). Solid black lines, reference smooth-wall profiles, i.e. $\epsilon^+ = 0$; blue to red lines, $\epsilon^+ = [-10, -5, -1, 1, 5, 10, 30]$; dotted black line in (a), laminar mean velocity profile, $U^+ = y^+$, for which $\nu_T/\nu = 0$.

log-law intercept B . For the above values of κ and A_d , $B \approx 5.24$. For reference, we can check that (3.8), with this definition of ν_T/ν (3.9), approaches $dU^+/dy^+ \sim 1/(\kappa y^+)$ for $y^+ \gg 1$. In the limit of small y/δ , (3.9) and the ensuing analysis also apply to other flows such as boundary layers. We can obtain the smooth-wall velocity profile by integrating (3.8), with the definition of ν_T^+ given by (3.9), such that

$$U_{sm}^+(y^+) = \int_0^{y^+} f(\xi^+) d\xi^+, \quad (3.10)$$

where ξ^+ is just the integration variable and y^+ is measured from the smooth wall where we have assumed $U_{sm}^+(0) = 0$ (as we are in the frame fixed to the wall). If $\nu_T^+ = 0$ in (3.10), there is no turbulence and the flow stays laminar, $U^+ = y^+$.

We now apply the idea that the effect of a certain surface texture is to bring turbulence, represented by the eddy viscosity, closer to or farther from the reference plane $y^+ = 0$. In this model, this is achieved by shifting the eddy viscosity ν_T^+ by ϵ^+ , say, in (3.9) and integrating to obtain the velocity profile above the textured wall U_r^+ :

$$U_r^+(y^+) = U_r^+(0) + \int_0^{y^+} f(\xi^+ + \epsilon^+) d\xi^+. \quad (3.11)$$

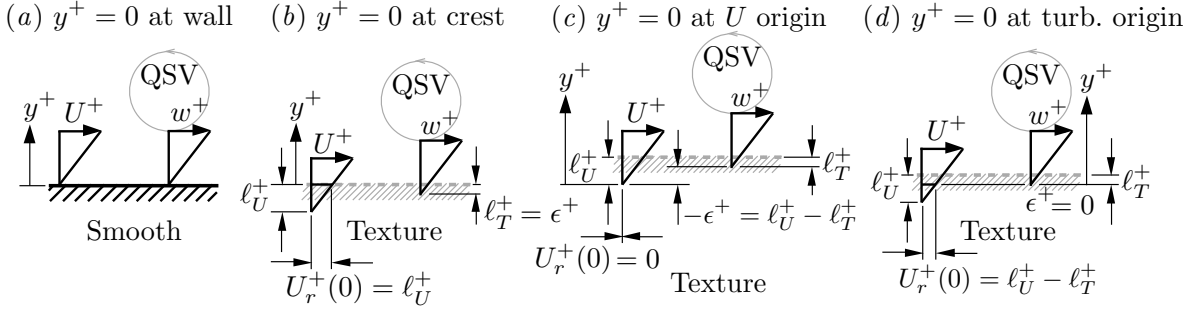


Figure 3.17 Various choices for the reference plane $y^+ = 0$ when considering textured surfaces (b, c, d) relative to the smooth wall (a). These choices give rise to different streamwise slip velocities $U_r^+(y^+ = 0)$ and origins for turbulence ϵ^+ relative to $y^+ = 0$, as indicated in the figures, and hence impact $\Delta U^+ \equiv U_r^+ - U_{sm}^+$ when evaluated at matched $y^+ \ll \infty$ using (3.12). The depths ℓ_U^+ and ℓ_T^+ are not influenced by this choice; and their respective virtual origins are fixed relative to the texture. QSV stands for quasi-streamwise vortices, used to represent the turbulence above walls. Note that $\partial u^+ / \partial y^+ \approx 1$ near the smooth wall and surface texture.

Comparing (3.11) and (3.10), we observe that if $\epsilon^+ = 0$, turbulence is placed as if a smooth wall were located at $y^+ = 0$, and the only effect of the texture is the Galilean transformation $U_r^+(0)$. Figure 3.16(a) shows the mean velocity profile, less the Galilean transformation $U_r^+(0)$, for several values of ϵ^+ . If $\epsilon^+ > 0$, turbulence is brought closer to the wall, because ν_T^+ activates for lower y^+ . Similarly, if $\epsilon^+ < 0$, turbulence is lifted from the wall, because ν_T^+ activates for higher y^+ , as shown by the profiles of Reynolds shear stresses in figure 3.16(c). Comparing figures 3.16(a) and (c), we observe increased velocity (drag reduction) for lifted turbulence and decreased velocity (drag increase) for lowered turbulence.

Unlike for the smooth wall, there are choices on where to locate $y^+ = 0$ for the textured wall. One convenient choice is at the crest of the textures. In this case, sketched in figure 3.17(b), $U_r^+(0)$ is the slip velocity evaluated at the crest and is equal to the height difference between the crest and the virtual origin for the mean flow, i.e. $U_r^+(0) = \ell_U^+$, and ϵ^+ is the height difference between the crest and the virtual origin for turbulence, i.e. $\epsilon^+ = \ell_T^+$. To obtain the shift in mean velocity ΔU^+ , we subtract (3.10) from (3.11) at matched y^+ (and choice of $y^+ = 0$):

$$\Delta U^+(y^+) = U_r^+(y^+) - U_{sm}^+(y^+) = U_r^+(0) + \int_0^{y^+} \left\{ f(\xi^+ + \epsilon^+) - f(\xi^+) \right\} d\xi^+. \quad (3.12)$$

If we instead chose $y^+ = 0$ to be the origin of the streamwise flow, as sketched in figure 3.17(c), then $U_r^+(0) = 0$ by definition and $\epsilon^+ = \ell_T^+ - \ell_U^+$. Yet another choice for $y^+ = 0$ is the origin for turbulence, as sketched in figure 3.17(d), wherein $U_r^+(0) = \ell_U^+ - \ell_T^+$ and $\epsilon^+ = 0$. This last choice is interesting because the integral in (3.12) vanishes, and we obtain immediately $\Delta U^+ = \ell_U^+ - \ell_T^+$ for all y^+ . We can see this in figure 3.16(b), which portrays the mean velocity against the distance to the origin for turbulence $y^+ + \epsilon^+$, regardless of the choice of $y^+ = 0$.

All profiles are parallel down into the viscous region, and so ΔU^+ must be a constant for all y^+ . Another point of consistency is that the modelled Reynolds shear stresses collapse when represented against the distance to the origin for turbulence $y^+ + \epsilon^+$, as shown in figure 3.16(d).

It is well known that in the logarithmic layer, where $y^+ \gg 1$, ΔU^+ is independent of the choice for $y^+ = 0$. To see conditions under which this occurs in the present model, we can set $y^+ \rightarrow \infty$ (logarithmic layer) in the upper limit of integration in (3.12) and find that the integral reduces to $-\int_0^{\epsilon^+} 1/[1+(\nu_T/\nu)(\xi^+)] d\xi^+ = -U^+(\epsilon^+)$, where U is the smooth-wall velocity profile, cf. (3.10), a somewhat surprising result. We know that the mean velocity profile for the smooth wall is $U^+(y^+) \sim y^+$ for $y^+ \lesssim 5$, and so $U^+(\epsilon^+) \sim \epsilon^+$ for $-\infty < \epsilon^+ \lesssim 5$, assuming that the profile extends linearly below $y^+ = 0$. Physically, the lower limit on ϵ^+ represents the idea that lifting turbulence away from the reference plane $y^+ = 0$, i.e. $\epsilon^+ < 0$, will allow the mean velocity profile to grow linearly, with unit gradient in wall units, up to $y^+ = -\epsilon^+$, regardless of the magnitude of ϵ^+ . That is, in (3.11) the integrand $f(\xi^+ + \epsilon^+)$ will be unity when $y^+ \leq -\epsilon^+$, since $\nu_T^+ = 0$ for $y^+ \leq 0$, as defined by (3.9). Substituting these results into (3.12), we obtain $\Delta U^+ \sim U_r^+(0) - U^+(\epsilon^+) \sim U_r^+(0) - \epsilon^+$ for $y^+ \gg 1$ and $-\infty < \epsilon^+ \lesssim 5$. This, in turn, reduces to $\Delta U^+ \sim \ell_U^+ - \ell_T^+$ for $y^+ = 0$ at crest, $\Delta U^+ \sim 0 - (\ell_T^+ - \ell_U^+)$ for $y^+ = 0$ at the U -origin, and $\Delta U^+ \sim (\ell_U^+ - \ell_T^+) - 0$ for $y^+ = 0$ at the origin for turbulence. In other words, we observe that if the integral in (3.12) is taken to $y^+ \rightarrow \infty$, $\Delta U^+ = \ell_U^+ - \ell_T^+$ is independent of the choice of reference plane $y^+ = 0$. Notably, Luchini et al. (1991) also demonstrated that, in the case of riblets, any ‘physically significant’ measure of the effect of the texture on the flow should be independent of the choice of origin. However, in practice the log layer is not thick enough due to finite Re_τ , and the integral in (3.12) cannot be taken to infinity. In that case, equation (3.12) indicates some sensitivity of ΔU^+ to the choice of reference plane.

We investigate this further by considering how the value of ΔU^+ is affected by the choice of $y^+ = 0$ and the upper limit of the integration in (3.12), i.e. the height at which ΔU^+ is measured. We now also include a fourth choice of $y^+ = 0$, where y^+ is measured from the notional valleys of the texture elements. In this reference frame, defining h^+ as the height of the elements in wall units, we would have $U_r^+(0) = \ell_U^+ - h^+$ and $\epsilon^+ = \ell_T^+ - h^+$, so that $\Delta U^+ \sim U_r^+(0) - \epsilon^+ = \ell_U^+ - \ell_T^+$ for $y^+ \rightarrow \infty$, as expected. In figure 3.18(a), profiles of U_r^+ from (3.11) are given for two hypothetical surfaces, one drag-reducing and one drag-increasing, with various choices of $y^+ = 0$. We see that, in each case, the profiles collapse only for large y^+ (in the logarithmic layer), as expected, and only then are they all parallel to the smooth-wall reference case. The profiles that have the origin for turbulence as $y^+ = 0$ are parallel to the smooth-wall profile for all y^+ , as discussed in section 3.1. This is confirmed in figure 3.18(c), which shows the values of ΔU^+ as a function of y^+ from (3.12) for both hypothetical surfaces, for the various choices of $y^+ = 0$. The figure shows that ΔU^+ is constant for all y^+ when the origin for turbulence is taken as $y^+ = 0$, whereas the curves for the other choices of $y^+ = 0$ asymptote to the ‘true’ value only when $y^+ \gtrsim 100$, i.e. in the log layer. This is consistent with the above analysis, where we demonstrated that ΔU^+ is independent of the choice of

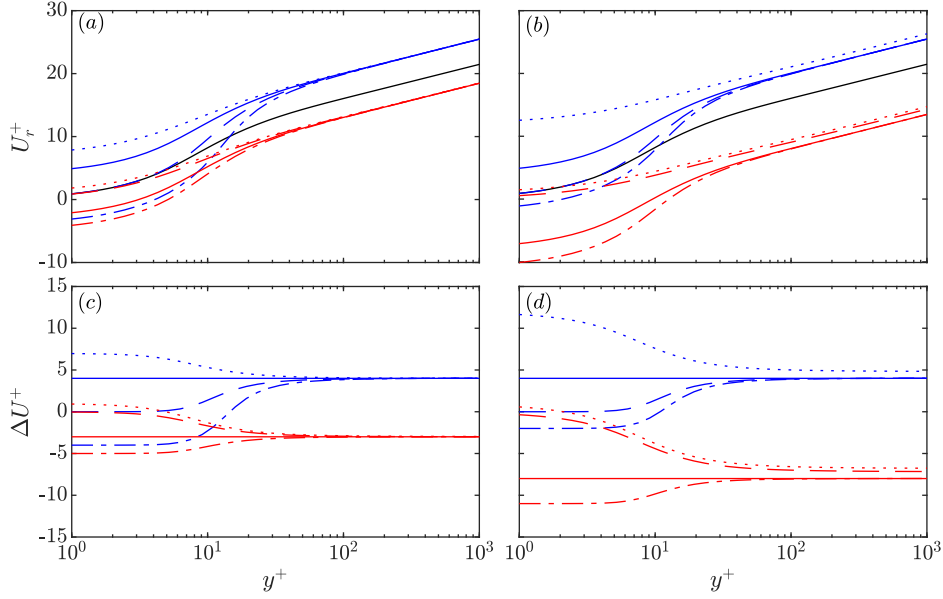


Figure 3.18 Mean velocity profiles U_r^+ from (3.11) (a,b) and variation of ΔU^+ with y^+ from (3.12) (c,d) for different textured walls and various choices of $y^+ = 0$. In the left hand panels (a,c): blue lines, $h^+ = 11$, with $\ell_U^+ = 7$ and $\ell_T^+ = 3$; red lines, $h^+ = 6$, with $\ell_U^+ = 1$ and $\ell_T^+ = 4$. In the right-hand panels (b,d): blue lines, $h^+ = 14$, with $\ell_U^+ = 12$ and $\ell_T^+ = 8$; red lines, $h^+ = 12$, with $\ell_U^+ = 1$ and $\ell_T^+ = 9$. In all panels: dotted lines, $y^+ = 0$ at crest; dashed lines, $y^+ = 0$ at U -origin; solid lines, $y^+ = 0$ at origin for turbulence; dash-dotted lines, $y^+ = 0$ at valleys. The solid black line in (a,b) denotes the reference smooth-wall profile.

$y^+ = 0$ when measured in the log layer. However, it highlights the potential for error when measuring ΔU^+ in experiments or simulations too close to the wall, which could be the only option at low Re_τ . That is, to precisely measure ΔU^+ irrespective of the choice of the reference $y^+ = 0$, the flow should exhibit a sufficiently thick log layer in the first place. While an exact definition of what this would require in practice is beyond the scope of this paper, this implies that Re_τ should be of the order of 500 or more, assuming the log layer is defined loosely as $80\nu/u_\tau \lesssim y \lesssim 0.3\delta$ (Sillero et al., 2013). In contrast, if the origin for turbulence is taken as $y^+ = 0$, then accurate measurements of ΔU^+ can be taken at any height, and thus at far lower values of Re_τ .

From the various choices of reference plane, and ensuing definitions of ϵ^+ (e.g. $\epsilon^+ = \ell_T^+$, $\epsilon^+ = 0$, $\epsilon^+ = \ell_T^+ - \ell_U^+$ and $\epsilon^+ = \ell_T^+ - h^+$), we can infer the values of ℓ_U^+ and ℓ_T^+ that would violate the condition $-\infty < \epsilon^+ \lesssim 5$. There is no need to consider a restriction on h^+ , because when $y^+ = 0$ is taken as the texture valleys, $\epsilon^+ = \ell_T^+ - h^+$ will always be negative, since the origin for turbulence will always be above the valleys (Luchini, 1995). We see immediately that the restrictions on ℓ_U^+ and ℓ_T^+ would be $\ell_T^+ \gtrsim 5$ and $\ell_T^+ - \ell_U^+ \gtrsim 5$. Note that the former limit is relevant both in the regime of drag increase or drag reduction, while the latter limit is relevant for drag increase only. Once the limits are exceeded, ΔU^+ would no longer necessarily be independent of the choice of $y^+ = 0$. Interestingly, we also deduced in section 3.5 from

our slip-length simulations that the virtual-origins framework would break down for $\ell_T^+ \gtrsim 5$. Figures 3.18(b,d) portray the mean velocity profiles, along with the variation of ΔU^+ with y^+ , for two hypothetical textured surface whose values of ℓ_U^+ and ℓ_T^+ result in $\epsilon^+ > 5$, depending on the choice of $y^+ = 0$. One surface satisfies $\ell_T^+ \gtrsim 5$ only, while the other satisfies both $\ell_T^+ \gtrsim 5$ and $\ell_T^+ - \ell_U^+ \gtrsim 5$. These figures demonstrate the potential for error when measuring ΔU^+ , even within the log layer. If ϵ^+ is too large when the texture crests or the origin for the mean flow are taken as $y^+ = 0$, as often done in the literature, it is not possible to measure ΔU^+ accurately at any height, regardless the magnitude of Re_τ . Therefore, to consistently measure ΔU^+ accurately for any texture and Reynolds number, y^+ should be measured from the origin for turbulence. However, if the texture valleys are taken as $y^+ = 0$, ΔU^+ may still be measured accurately within the log layer, provided the Reynolds number is large enough.

Chapter 4

An idealised logarithmic-layer control strategy: theoretical predictions

We now move away from our discussion on virtual origins and the effect of buffer-layer control strategies. In this chapter, we consider the effect on the flow of an idealised, logarithmic-layer control strategy. First, we assume that the control is able to remove all of the Reynolds shear stress in all or part of the logarithmic layer, while leaving the rest of the flow unaltered, and derive an expression for the change in the mean velocity profile compared to a reference, uncontrolled flow. We then consider how this effect would depend on Re_τ , and extend the analysis for the case where only some of the Reynolds shear stress is removed from the controlled region. The results of this chapter could serve as a theoretical prediction for the maximum drag reduction achievable by strategies that target the logarithmic layer alone.

4.1 Relaminarising the logarithmic layer

Let us assume that some hypothetical, idealised control strategy could relaminarise all or part of the logarithmic layer, while leaving the rest of the flow unaltered. This would be equivalent to removing all the turbulent fluctuations within the controlled region, and can be thought of as the optimum that any logarithmic-layer control strategy could achieve, in terms of turbulent drag reduction. The integral mean streamwise momentum equation for fully-developed channel flow, averaged in the wall-parallel directions and time can be written as

$$1 - \frac{y^+}{Re_\tau} = \frac{dU^+}{dy^+} - \overline{u'v'^+}, \quad (4.1)$$

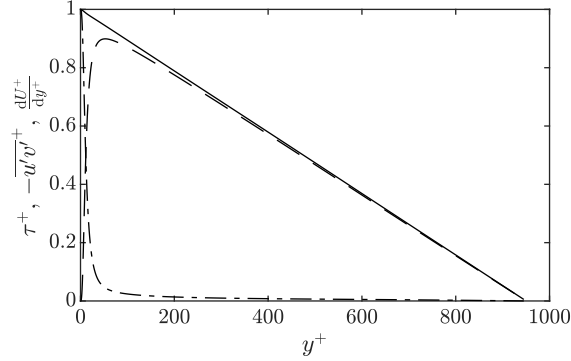


Figure 4.1 Mean stress balance, encapsulated by (4.1), for $Re_\tau = 950$. Solid line, total fluid stress, τ^+ ; dashed line, Reynolds shear stress, $-\overline{u'v'}^+$; dash-dotted line, viscous stress, dU^+/dy^+ .

where $\overline{u'v'}^+$ is the Reynolds shear stress.¹ The expression on the left-hand side of equation (4.1) is the total fluid stress, τ^+ , at a given height y^+ , and is the sum of the viscous and Reynolds shear stresses at that height, as defined by the right-hand side of the equation. The total, viscous and Reynolds shear stresses are portrayed in figure 4.1 for a canonical, uncontrolled channel flow at $Re_\tau = 950$, for reference.

An expression for the uncontrolled mean velocity as a function of y^+ can be found by integrating (4.1) between y_{min}^+ and y^+ , which yields

$$U_0^+(y^+) = U_0^+(y_{min}^+) + y^+ \left(1 - \frac{y^+}{2Re_\tau}\right) - y_{min}^+ \left(1 - \frac{y_{min}^+}{2Re_\tau}\right) - \mathcal{T}_{uv}, \quad (4.2)$$

where

$$\mathcal{T}_{uv} = - \int_{y_{min}^+}^{y^+} \overline{u'v'}_0^+ dy^+ \quad (4.3)$$

and the ‘0’ subscript refers to uncontrolled values. Note that \mathcal{T}_{uv} is always positive, since $\overline{u'v'}_0^+ \leq 0$ for $0 \leq y^+ \leq Re_\tau$, as shown in figure 4.1. We wish to determine the effect of removing all the Reynolds shear stress in all or part of the logarithmic layer, while leaving the rest of the flow unaltered. Therefore, we choose as reference a height within the logarithmic layer, such that $80 \leq y_{min}^+ \leq 0.3Re_\tau$, which comes directly from the limits of the logarithmic layer defined in (1.8). As such, $U_0^+(y_{min}^+)$ can be approximated well from the logarithmic law (1.9). We then assume that $\overline{u'v'}^+ = 0$ in the region $y_{min}^+ \leq y^+ \leq y_{max}^+$, where $y_{max}^+ \leq 0.3Re_\tau$. From (4.2), the mean velocity profile in this case would be

$$U_p^+(y^+) = U_0^+(y_{min}^+) + y^+ \left(1 - \frac{y^+}{2Re_\tau}\right) - y_{min}^+ \left(1 - \frac{y_{min}^+}{2Re_\tau}\right), \quad (4.4)$$

where U_p^+ is a parabolic, laminar mean profile, valid for $y_{min}^+ \leq y^+ \leq y_{max}^+$.

¹Note that the analysis conducted in this chapter is for the specific case of turbulent channels, but it can be easily extended to other equilibrium shear flows, such as zero-pressure-gradient boundary layers or pipe flows.

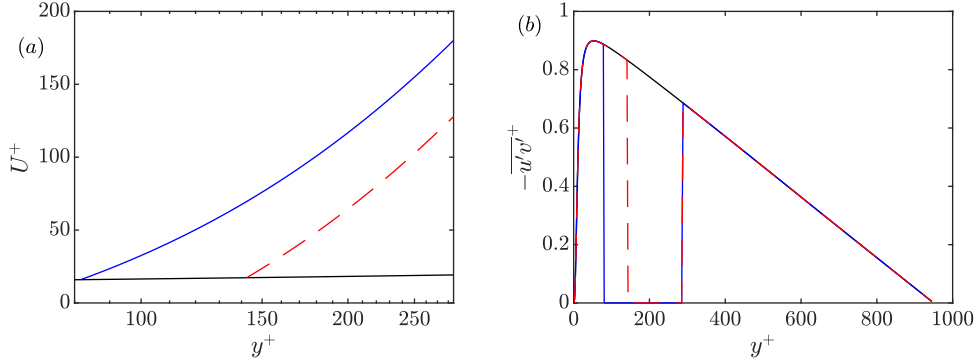


Figure 4.2 Example mean velocity profiles (a) and Reynolds shear stress profiles (b) of the present idealised control strategy, compared to the uncontrolled reference case. In (a), parabolic, laminar mean velocity profiles, U_p^+ , defined by (4.4), for $Re_\tau = 950$. In (b), Reynolds shear stress with $-\overline{u'v'}^+ = 0$ in the controlled region. Black lines, uncontrolled case; blue lines, controlling the whole log layer, with $y_{min}^+ = 80$ and $y_{max}^+ = 0.3Re_\tau$; red dashed lines, controlling only part of the log layer, with $y_{min}^+ = 0.15Re_\tau$ and $y_{max}^+ = 0.3Re_\tau$. Note that in each controlled case, we assume that the Reynolds shear stress outside of the controlled region remains the same as in the uncontrolled case.

For illustrative purposes, two mean velocity profiles computed using equation (4.4) are portrayed in figure 4.2(a) for $Re_\tau = 950$, along with their Reynolds stress profiles in figure 4.2(b). The first case has $y_{min}^+ = 80$ and $y_{max}^+ = 0.3Re_\tau$, i.e. controlling the whole logarithmic layer, while the second has $y_{min}^+ = 0.15Re_\tau$ and $y_{max}^+ = 0.3Re_\tau$, i.e. controlling only part of the logarithmic layer. We see that the mean velocity at the top of the logarithmic layer for the controlled cases is an order of magnitude larger than the uncontrolled one.

The difference between the controlled, parabolic mean velocity profile (4.4) and the uncontrolled one (4.2) is

$$\Delta U_p^+(y^+) = U_p^+(y^+) - U_0^+(y^+) = \mathcal{T}_{uv}. \quad (4.5)$$

In the logarithmic layer, the exact equation for the uncontrolled mean velocity profile (4.2) is approximated well by the logarithmic law (1.9), and so

$$U_0^+(y^+) \approx U_{log}^+(y^+) = \frac{1}{\kappa} \log y^+ + A. \quad (4.6)$$

The Reynolds shear stress $\overline{u'v'}_0^+$ may be found by differentiating (4.6) and substituting the resulting expression for viscous stress dU_0^+/dy^+ into equation (4.1). \mathcal{T}_{uv} can then be calculated from (4.3), yielding $\Delta U_p^+(y^+)$ (4.5). However, an alternative (and equivalent) approach is to substitute (4.6) into (4.5) directly,

$$\Delta U_p^+(y^+) \approx U_p^+(y^+) - U_{log}^+(y^+), \quad (4.7)$$

which depends only on known quantities and thus can be used to predict ΔU_p^+ without further algebraical manipulation.

Since we have assumed that the flow is unaltered outside the controlled region, the Reynolds shear stress profile for $y^+ > y_{max}^+$ would be the same as that of the uncontrolled flow, as shown in figure 4.2(b). Therefore, above the controlled region the mean velocity profile would be shifted with respect to the uncontrolled one, but parallel to it. It follows that the difference between the controlled and uncontrolled profiles at the channel centre, $\Delta U_p^+(y^+ = Re_\tau)$, is equal to their difference at the top of the controlled region, $\Delta U_p^+(y^+ = y_{max}^+)$. Evaluating (4.7) at $y^+ = y_{max}^+$, we have

$$\Delta U_p^+(y^+ = Re_\tau) = U_p^+(y_{max}^+) - U_{log}^+(y_{max}^+), \quad (4.8)$$

which provides an expression for the outward shift of the mean velocity profile at the channel centre compared to an uncontrolled flow at the same Reynolds number, assuming the flow is relaminarised within the logarithmic layer in the region $y_{min}^+ \leq y^+ \leq y_{max}^+$. From (4.8), the value of $\Delta U_p^+(y^+ = Re_\tau)$ for the two examples presented in figure 4.2 is approximately 162 and 109, respectively. These large values of ΔU_p^+ suggest that the potential drag reduction achievable by control strategies that target the flow logarithmic layer alone could be significant. This will be discussed more in the next section.

4.2 Effect of Reynolds number

We are now in a position to determine how the change in the mean velocity profile, ΔU_p^+ , caused by this idealised control strategy varies with Re_τ . From equations (4.8) and (4.4), we might expect that the specific choice of y_{min}^+ and y_{max}^+ would affect the variation of $\Delta U_p^+(y^+ = Re_\tau)$ with Re_τ . We consider three choices of y_{min}^+ and y_{max}^+ :

1. $y_{min}^+ = 80$ and $y_{max}^+ = 0.3Re_\tau$, which corresponds to controlling the whole logarithmic layer for all Re_τ . The thickness of the controlled region therefore varies with Re_τ , both in inner and outer units.
2. $y_{min}^+ = c_1Re_\tau$ and $y_{max}^+ = c_2Re_\tau$, with $c_1 < c_2$ and $80/Re_\tau \leq c_1, c_2 \leq 0.3Re_\tau$. Equivalently, we would have $y_{min} = c_1\delta$ and $y_{max} = c_2\delta$, which corresponds to controlling a fixed region of the flow in outer units as Re_τ varies.
3. $y_{min}^+ = c_3$ and $y_{max}^+ = c_4$, with $c_3 < c_4$ and $80 \leq c_3, c_4 \leq 0.3Re_\tau$ for all Re_τ . This corresponds to controlling a fixed region of the flow in inner units.

To demonstrate the differences between these three cases, we set $c_1 = 80/550 \approx 0.145$, $c_2 = 0.3$, $c_3 = 80$ and $c_4 = 165$. These values are chosen for convenience, because they correspond to controlling the whole logarithmic layer at $Re_\tau = 550$ for all three cases, although the controlled regions obviously become different as Re_τ is varied.

Figure 4.3 portrays the variation of $\Delta U_p^+(y^+ = Re_\tau)$ with Re_τ (4.8) for these three choices of y_{min}^+ and y_{max}^+ , starting from $Re_\tau = 550$. When the whole logarithmic layer is controlled, i.e.

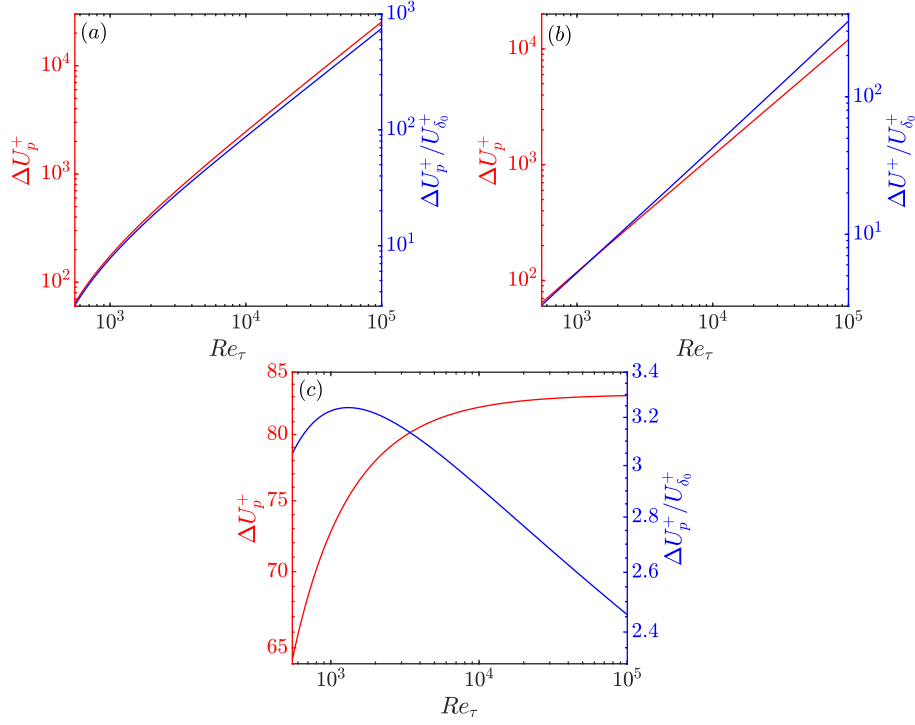


Figure 4.3 Variation of $\Delta U_p^+(y^+ = Re_\tau)$ (4.8), red lines, and $\Delta U_p^+(y^+ = Re_\tau)/U_{\delta_0}^+$, blue lines, with Re_τ for the present idealised control strategy. Three different choices of y_{min}^+ and y_{max}^+ are considered in the range $550 \leq Re_\tau \leq 10^5$: (a) the whole logarithmic layer is controlled, $y_{min}^+ = 80$ and $y_{max}^+ = 0.3Re_\tau$; (b) a fixed region in outer units is controlled, $y_{min}^+ = c_1 Re_\tau$ and $y_{max}^+ = c_2 Re_\tau$, with $c_1 = 0.145$ and $c_2 = 0.3$; (c) a fixed region in inner units is controlled, $y_{min}^+ = c_3$ and $y_{max}^+ = c_4$, with $c_3 = 80$ and $c_4 = 165$. Note that all axes have a logarithmic scale, and the uncontrolled centreline velocity is approximated using the logarithmic fit to the channel data given in figure 1.9, i.e. $U_{\delta_0}^+ \approx 2.45 \log Re_\tau + 5.62$.

$y_{min}^+ = 80$ and $y_{max}^+ = 0.3Re_\tau$, we see that ΔU_p^+ increases with Re_τ , as shown in figure 4.3(a). This is not surprising, since the thickness of the logarithmic layer grows in inner units as Re_τ is increased, and so we would also expect the effect of the control in inner units, i.e. ΔU_p^+ , to increase with Re_τ . Eventually, we see that ΔU_p^+ appears to grow linearly for $Re_\tau \gtrsim 10^3$. Indeed, in the limit of large Re_τ , it is easy to show from (4.4) that the velocity at the upper limit of the control region in this case is

$$U_p^+(y^+ = 0.3Re_\tau) = U_0^+(y^+ = 80) + 0.255Re_\tau - 80. \quad (4.9)$$

Then from (4.8), we would have

$$\Delta U_p^+(y^+ = Re_\tau) = U_0^+(y^+ = 80) + 0.255Re_\tau - 80 - \frac{1}{\kappa} \log(0.3Re_\tau) - A. \quad (4.10)$$

That is, for large Re_τ , to leading order, ΔU_p^+ increases linearly with Re_τ , consistent with figure 4.3(a). Here, the lower limit of the control region in outer units is $y_{min}/\delta = 80/Re_\tau$, which tends to zero as Re_τ increases, whereas the upper limit is fixed at $y_{max}/\delta = 0.3$.

Therefore, for large enough Re_τ , controlling the whole logarithmic layer is essentially equivalent to controlling a fixed region of the flow in outer units, $0 \lesssim y/\delta \lesssim 0.3$.

When the control region is fixed in outer units, i.e. $y_{min}^+ = 0.145Re_\tau$ and $y_{max}^+ = 0.3Re_\tau$, we thus also observe that $\Delta U_p^+(y^+ = Re_\tau)$ increases essentially linearly for all Re_τ , as shown in figure 4.3(b). In this case, from (4.8),

$$\Delta U_p^+(y^+ = Re_\tau) = U_0^+(y^+ = 0.145Re_\tau) + 0.121Re_\tau - 80 - \frac{1}{\kappa} \log(0.3Re_\tau) - A, \quad (4.11)$$

for all Re_τ . Again, to leading order, $\Delta U_p^+(y^+ = Re_\tau)$ increases linearly with Re_τ , since the first term on the right-hand side increases only logarithmically with Re_τ . In this second case, like the first, the thickness of the control region in inner units grows with Re_τ , and thus so does ΔU_p^+ .

For the third choice, when a fixed region of the flow in inner units is controlled, i.e. $y_{min}^+ = 80$ and $y_{max}^+ = 165$, ΔU_p^+ appears to asymptote to a constant value for large Re_τ , in contrast to the first two cases, as shown in figure 4.3(c). This is confirmed by considering the variation of $\Delta U_p^+(y^+ = Re_\tau)$ in the limit of large Re_τ in this case, from (4.8),

$$\Delta U_p^+(y^+ = Re_\tau) = U_0^+(y^+ = 80) + 165 - 80 - \frac{1}{\kappa} \log(165) - A, \quad (4.12)$$

which does not depend on Re_τ . This is the expected result, because the control region is fixed in inner units, and thus the effect of the control in inner units should remain essentially constant with Re_τ . This is analogous to the behaviour observed for control strategies that target the buffer layer, as discussed in chapter 1, and observed in the virtual origin simulations at different Re_τ discussed in section 3.4. That is, when the control parameters, i.e. the virtual origins imposed on the flow, were fixed in inner units, ΔU^+ remained constant with Re_τ .

As alluded to above, ΔU_p^+ provides a measure of the effect of the control in inner units, by definition. In turn, $\Delta U_p^+/U_{\delta_0}^+$ can be viewed as a measure of the effect of the control on the flow in outer units. Here, we choose the reference velocity $U_{\delta_0}^+$ to be the channel centreline velocity of the uncontrolled flow, which, as discussed in section 1.2, allows for comparison with external flows of interest. It may be tempting to simplify $\Delta U_p^+/U_{\delta_0}^+$ and write it as $\Delta U_p/U_{\delta_0}$, neglecting the normalisation of the variables in wall units. However, while $\Delta U_p/U_{\delta_0}$ is dimensionless, it is not such a convenient expression, because U_{δ_0} will vary with u_τ , even for fixed Re_τ . Therefore, when comparing flows at the same Re_τ but different u_τ , it would first be necessary to normalise each mean velocity profile by the centreline velocity U_{δ_0} of its respective uncontrolled flow at the same Re_τ and u_τ , before computing the difference between them, i.e. $\Delta(U_p/U_{\delta_0})$. If the ‘+’ superscripts are retained, we can compute $\Delta U_p^+/U_{\delta_0}^+$ directly from ΔU_p^+ , since $U_{\delta_0}^+$ is fixed for a given Re_τ , making comparisons easier. Indeed, $\Delta U_p^+/U_{\delta_0}^+$ is also the important metric when measuring the drag reduction as demonstrated by equation (1.4), which we repeat here

for reference,

$$DR = 1 - \left(\frac{1}{1 + \Delta U_p^+ / U_{\delta_0}^+} \right)^2. \quad (4.13)$$

Even though this equation was derived in section 1.2 in the context of small-textured surfaces, if we take the reference velocity $U_{\delta_0}^+$ as the channel centreline velocity of the uncontrolled flow, it is valid for any control strategy that produces a shift in the mean velocity profile that extends to the channel centre.

As well as ΔU_p^+ , figure 4.3 shows $\Delta U_p^+(y^+ = Re_\tau) / U_{\delta_0}^+$ for each of the three choices of y_{min}^+ and y_{max}^+ . As discussed in section 1.3, the channel centreline velocity $U_{\delta_0}^+$ increases quasi-logarithmically with Re_τ . Therefore, due to the approximate linear behaviour of $\Delta U_p^+(y^+ = Re_\tau)$ for the first two choices of y_{min}^+ and y_{max}^+ , when either the whole logarithmic layer or a fixed portion of it in outer units is controlled, the variation of $\Delta U_p^+(y^+ = Re_\tau) / U_{\delta_0}^+$ with Re_τ is not qualitatively different to that of $\Delta U_p^+(y^+ = Re_\tau)$, except for the difference in magnitude, as shown in figure 4.3(a, b). From (4.13), we also see that the drag reduction would improve with Re_τ in these cases. This is perhaps a surprising result, because it might be expected that the effect of control would be essentially constant in outer units with Re_τ , at least for large Re_τ , since the thickness of the logarithmic layer then becomes essentially constant in outer units, as discussed above. However, as discussed by Jiménez (2018), the fraction of the turbulent dissipation, i.e. Reynolds shear stress, contained within the logarithmic layer actually increases with Re_τ . The idealised control strategy considered here removes all the Reynolds shear stress from the control region. Therefore, in these cases, the control would remove a larger and larger proportion of the turbulent dissipation as Re_τ increases, which explains why the drag reduction improves with Reynolds number. In contrast, for the third choice of y_{min}^+ and y_{max}^+ , where a fixed region of the flow in inner units is controlled, $\Delta U_p^+(y^+ = Re_\tau) / U_{\delta_0}^+$ decreases with Re_τ , as shown in figure 4.3(c), and thus the drag reduction degrades. This is to be expected, since the thickness of the controlled region in outer units diminishes as Re_τ is increased, akin to the behaviour observed for control strategies that target the buffer layer, as discussed in chapter 1.

It should be mentioned that the values of ΔU_p^+ and $\Delta U_p^+ / U_{\delta_0}^+$ presented here are extremely large and are not physically realistic, particularly when the whole logarithmic layer or a fixed part of it in outer units is controlled. For instance, when the whole logarithmic layer is controlled at $Re_\tau = 10^5$, the centreline velocity is approximately 1000 times larger than that of the uncontrolled flow, as shown in figure 4.3(a). From the outset, we have assumed that the present hypothetical control strategy removes all of the Reynolds shear stress in the control region, which would clearly not be possible in reality. However, as mentioned above, this can be thought of as the optimum that any logarithmic-layer control strategy could achieve, and thus provides an upper bound for the potential performance of real control strategies. Figure 4.4 portrays the variation of drag reduction, DR , with $\Delta U_p^+ / U_{\delta_0}^+$, defined by (4.13), to provide some context for the values shown in figure 4.3. From figure 4.4, we see that DR

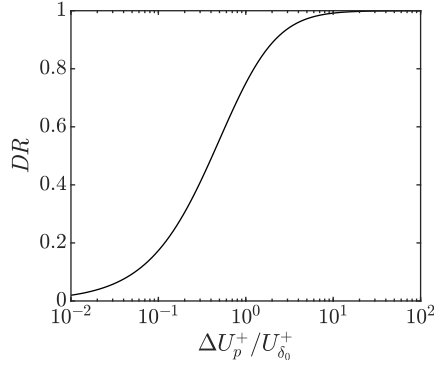


Figure 4.4 Variation of DR with $\Delta U_p^+ / U_{\delta_0}^+$, defined by equation (4.13).

saturates relatively quickly, and for $\Delta U_p^+ / U_{\delta_0}^+ \gtrsim 10$, i.e. a ten-fold increase in the channel centreline velocity compared to the uncontrolled flow, we already observe approximately 100% turbulent drag reduction. For the first two choices of y_{min}^+ and y_{max}^+ described above, shown in figure 4.3(a, b), $DR \approx 100\%$ by $Re_\tau \approx 2000$, which emphasises how large the values of $\Delta U_p^+ / U_{\delta_0}^+$ are in these cases. In the case where a fixed region of the flow in inner units is controlled, $\Delta U_p^+ / U_{\delta_0}^+$ is of order 3, as shown in figure 4.3(c), which corresponds to approximately 95% drag reduction, although we note that the drag reduction degrades with Re_τ in this case. We can conclude, therefore, that logarithmic-layer control strategies have significant potential, in terms of generating a large reduction in drag. Further, if the whole logarithmic layer or a fixed part of it in outer units is controlled, the results of this section suggest that it might be possible to generate a reduction in drag that improves with Re_τ . How this might be achieved in reality is beyond the scope of this thesis, but we will investigate this idea further with our logarithmic-layer control simulations in chapter 5.

4.3 Effect of removing only some of the Reynolds shear stress

We assumed above that the present hypothetical control strategy removes all the Reynolds shear stress in the controlled region, i.e. $\overline{u'v'}^+ = 0$ for $y_{min}^+ \leq y^+ \leq y_{max}^+$. We now extend our analysis to consider the case where the control strategy removes only some of the Reynolds shear stress in the controlled region. This could be because the control does not behave as efficiently as expected, for instance. Alternatively, this could be used to predict the effect of control strategies that remove only a certain proportion of $\overline{u'v'}^+$ by design, as we do in our simulations in chapter 5, where we remove only certain length scales of the wall-normal velocity from the flow.

Let us assume now that the hypothetical control strategy aims to remove a fixed proportion, ϕ , of the Reynolds shear stress in the uncontrolled flow within the controlled region. We define $0 \leq \phi \leq 1$. Following the above analysis in section 4.1, the controlled mean velocity profile in

the region $y_{min}^+ \leq y^+ \leq y_{max}^+$ would be given by

$$\begin{aligned} U_c^+(y^+) &= U_0^+(y_{min}^+) + y^+ \left(1 - \frac{y^+}{2Re_\tau}\right) - y_{min}^+ \left(1 - \frac{y_{min}^+}{2Re_\tau}\right) - (1 - \phi)\mathcal{T}_{uv} \\ &= U_p^+(y^+) - (1 - \phi)\mathcal{T}_{uv}, \end{aligned} \quad (4.14)$$

where \mathcal{T}_{uv} is the integral of the uncontrolled Reynolds shear stress in the control region, as defined by (4.3). When $\phi = 1$, all of the Reynolds shear stress is removed, and we recover the parabolic, laminar profile (4.4), i.e. $U_c^+ = U_p^+$. When $\phi = 0$, none of the Reynolds shear stress is removed, and U_c^+ becomes the uncontrolled mean velocity profile, U_0^+ , defined by (4.2). In section 4.1, we demonstrated that $\mathcal{T}_{uv} = U_p^+(y^+) - U_0^+(y^+)$, as shown by equation (4.5). However, $U_0^+(y^+) \approx U_{log}^+$, where U_{log}^+ is the logarithmic law (4.6). Therefore, we can write

$$\mathcal{T}_{uv} \approx U_p^+(y^+) - U_{log}^+(y^+). \quad (4.15)$$

Substituting (4.15) into (4.14) yields

$$U_c^+(y^+) = U_p^+(y^+) - (1 - \phi) \left(U_p^+(y^+) - U_{log}^+(y^+) \right). \quad (4.16)$$

The difference between the controlled and uncontrolled profiles can then be evaluated, as follows:

$$\begin{aligned} \Delta U_c^+(y^+) &= U_c^+(y^+) - U_0^+(y^+) \approx U_c^+(y^+) - U_{log}^+(y^+) \\ &= \phi(U_p^+(y^+) - U_{log}^+(y^+)) \\ &= \phi\Delta U_p^+(y^+). \end{aligned} \quad (4.17)$$

That is, for a given height y^+ , there is a linear relationship between $\Delta U_c^+(y^+)$ and $\Delta U_p^+(y^+)$, and the constant of proportionality is ϕ . In hindsight, this result is not surprising. It is nevertheless useful, because it demonstrates that the qualitative behaviour of this hypothetical control strategy is the same, irrespective of the proportion of the Reynolds stress that is removed. For instance, the general behaviour of ΔU^+ with Re_τ , presented in figure 4.3, would be unchanged, the only difference being the multiplicative factor ϕ .

4.4 Summary

We conclude this chapter by briefly summarising the key results. We have analysed the behaviour of a hypothetical control strategy that removes a fixed proportion of the Reynolds shear stress within all or part of the logarithmic layer, while leaving the rest of the flow unaltered. The limits of the logarithmic layer are taken as $80 \lesssim y^+ \lesssim 0.3Re_\tau$. The proportion of Reynolds stress removed is ϕ , with $0 \leq \phi \leq 1$, and the controlled region is defined by $y_{min}^+ \leq y^+ \leq y_{max}^+$, with $80 \leq y_{min}^+ < y_{max}^+ \leq 0.3Re_\tau$. For a particular choice of y_{min}^+ , y_{max}^+ and Re_τ , the mean

velocity profile in the controlled region, $U_c^+(y^+)$, is given by equation (4.16). Equation (4.16) is a linear combination of ϕ , the parabolic, laminar mean velocity profile $U_p^+(y^+)$ (4.4) and the logarithmic law $U_{log}^+(y^+)$ (4.6). When $\phi = 0$, $U_c^+(y^+)$ recovers the uncontrolled mean velocity profile, while $U_c^+(y^+) = U_p^+(y^+)$ for $\phi = 1$. The difference between the controlled and uncontrolled mean velocity profiles is given by $\Delta U_c^+(y^+) = U_c^+(y^+) - U_0^+(y^+) = \phi \Delta U_p^+$ (4.17), where $U_0^+(y^+)$ is the uncontrolled mean velocity profile. The variation of both ΔU_p^+ and $\Delta U_p^+/U_{\delta_0}^+$ with Re_τ are included in figure 4.3 for various choices of y_{min}^+ and y_{min}^+ . We observe that control strategies that target the logarithmic layer alone have significant potential, in terms of generating a large reduction in drag that does not degrade with Re_τ , although the way this might be achieved in reality is beyond the scope of this thesis.

Chapter 5

Selective control of the logarithmic layer: results from DNS

In section 1.3, we discussed the logarithmic layer in detail. In particular, we focussed on the description of the flow in terms of self-similar, wall-attached eddies. In an averaged sense, they can be viewed as a vortex cluster flanked by a sweep and an ejection, with a corresponding pair of high- and low-speed streaks, as portrayed in figure 1.11 (del Álamo et al., 2006; Flores and Jiménez, 2010; Lozano-Durán et al., 2012). Keeping in mind this structural description of the flow, in this chapter we investigate methods for controlling the flow in the logarithmic layer, without directly modifying the flow elsewhere. As mentioned in chapter 1, typical control strategies, such as the use of wall-normal jets, can also modify the flow within the buffer layer, making it difficult to separate the effect of controlling the logarithmic layer from the other changes in the flow. Here, we discuss the results of a series of simulations conducted at friction Reynolds numbers in the range $360 \leq Re_\tau \leq 2000$ in which we artificially remove certain streamwise and spanwise length scales from the wall-normal velocity, v , primarily within the logarithmic region. The idea is that the contribution to uv for those length scales will be zero, with the objective of disrupting the sweep and ejection motions discussed above. Our simulations are split into two groups, simulations with ‘block forcing’ and simulations with ‘hierarchical forcing’, which are discussed in sections 5.1 and 5.2, respectively. The method for removing the desired length scales from the flow is described in section 2.4, and we will discuss the details of each group of simulations below. As already mentioned in chapter 1, we note that it would not be possible to implement this form of control in reality, but it is hoped that our simulations might isolate and provide insight into the effect of controlling the logarithmic layer alone, while affecting the rest of the flow as little as possible.

Preliminary results of the block-forcing simulations presented in section 5.1 have been published in Ibrahim et al. (2020).

5.1 Simulations with block forcing

As discussed in section 2.4, in our logarithmic-layer control simulations, we artificially remove certain streamwise and spanwise length scales, $\lambda_{x,t}$ and $\lambda_{z,t}$, from the wall-normal velocity within the forcing region, y_f . In the first group of simulations, the target length scales are the same for every plane within the forcing region and occupy a ‘block’ in $(\lambda_x, \lambda_z, y)$ space. That is, the target length scales satisfy $\lambda_{x,min} \leq \lambda_{x,t} \leq \lambda_{x,max}$ and $\lambda_{z,min} \leq \lambda_{z,t} \leq \lambda_{z,max}$, in the forcing region $y_{f,min} \leq y_f \leq y_{f,max}$. We thus refer to this group of simulations as simulations with ‘block forcing’, and the general idea is to target the self-similar, wall-attached vortex clusters described by del Álamo et al. (2006), which have an aspect ratio of approximately 6:2:3 in the streamwise, wall-normal and spanwise directions, respectively. Del Álamo et al. (2006) also reported that the aspect ratio of the vortex clusters agrees well with the dominant length scales in the energy spectrum of the wall-normal velocity. For reference, the premultiplied two-dimensional spectral density of v^2 , i.e. $k_x k_z E_{vv}^+$, is shown at three heights within the logarithmic layer for a turbulent channel at $Re_\tau = 950$ in figure 5.1(b, f, j). The figure confirms that the central lobe of the spectrum matches well with the line $\lambda_z^+ = 3\lambda_x^+/6$ in the logarithmic layer, as reported by del Álamo et al. (2006). It also demonstrates that as we move away from the wall, the energy containing length scales of v tend to larger values of λ_x^+ and λ_z^+ .

In each case, the target length scales are chosen as follows. We assume that if a given vortex cluster is positioned such that its centre of gravity is at y_c then it will have a streamwise length $6y_c$, a spanwise width $3y_c$ and a height $2y_c$. In these simulations, we aim to target a subset of the self-similar family of vortex clusters, centred at y_t , which we refer to as the target height. It follows that the dominant length scales a vortex cluster centred at y_t would be $(\lambda_x, \lambda_z) \lesssim (6y_t, 3y_t)$. These wavelengths are denoted by the red crosses in figure 5.1(b, f, j), where y_t corresponds to the height at which the spectra are shown. Note that the crosses do not align exactly with the central lobe of the spectrum, due to contributions to the energy at y_t from structures centred at different heights. In each case, we fix the target height y_t and then remove the range of wavelengths $2 \leq \lambda_{x,t}/y_t \leq 6$ and $1 \leq \lambda_{z,t}/y_t \leq 3$. The largest wavelengths correspond to the nominal length and width of the clusters centred at y_t , and the idea is that the smaller ones should account for at least some of their dynamics at smaller scales. Example forcing regions are denoted by the dotted rectangles in figure 5.1(b, f, j), assuming that y_t corresponds to the height at which the spectra are shown. These wavelengths are then removed from v in the forcing region, y_f , either at one height or across a range of heights.

Our block forcing simulations are conducted at three friction Reynolds numbers, $Re_\tau = 360$, 550 and 950, and are summarised in table 5.1. In order to investigate the effect of Reynolds number on the control strategy, some of the simulations at different Reynolds numbers are designed to be consistent in inner or outer units, such as cases P360-150, P550-150 and P950-150, which are consistent in inner units. This will be discussed in more detail below. We also explore the effect of changing the forcing region while keeping the target height fixed. For

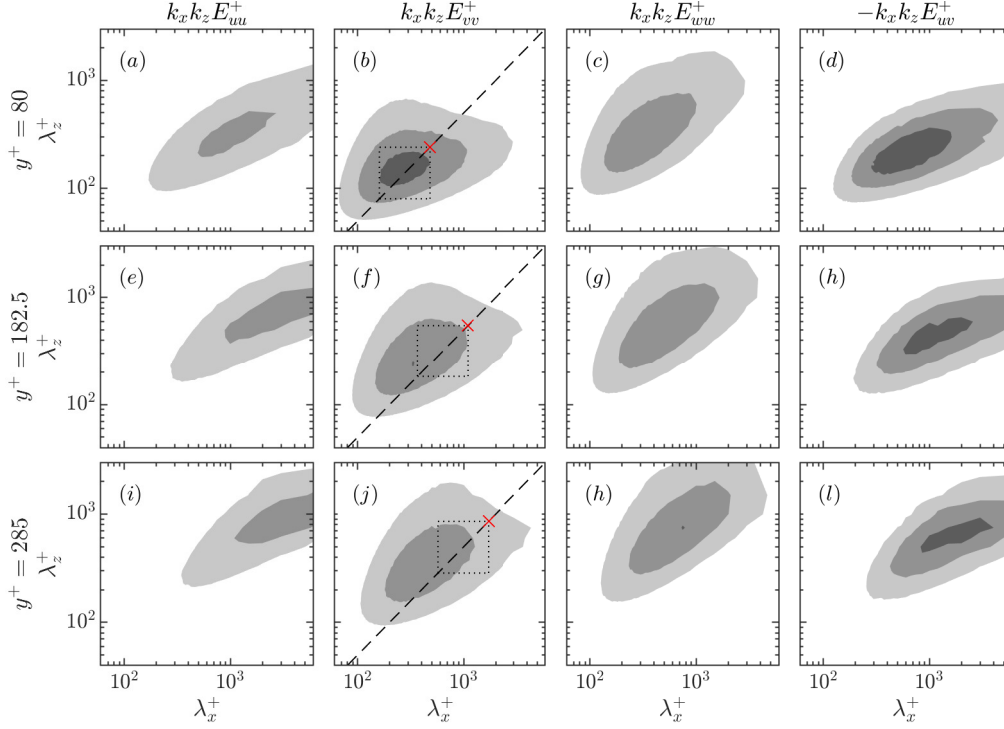


Figure 5.1 Premultiplied two-dimensional spectral densities of u^2 , v^2 , w^2 and uv normalised by u_τ^2 , within the logarithmic layer for an uncontrolled channel at $Re_\tau = 950$. (a–d) at the bottom limit of logarithmic layer, $y^+ = 80$; (e–h) in the middle of the logarithmic layer, $y^+ = 182.5$; (i–l) at the top limit of the logarithmic layer, $y^+ = 0.3Re_\tau = 285$. (a, e, i) $k_x k_z E_{uu}^+$; (b, f, j) $k_x k_z E_{vv}^+$; (c, g, h) $k_x k_z E_{ww}^+$; (d, h, l) $-k_x k_z E_{uv}^+$. The dotted lines in (b, f, j) are $\lambda_z^+ = 3\lambda_x^+/6$, which is consistent with the streamwise-to-spanwise aspect ratio of the self-similar vortex clusters of [del Álamo et al. \(2006\)](#). The red crosses denote $(\lambda_x^+, \lambda_z^+) = (6y_t^+, 3y_t^+)$, where y_t^+ corresponds to the height at which the spectra are shown. The black dotted rectangles mark the region $2y_t^+ \leq \lambda_x^+ \leq 6y_t^+$ and $y_t^+ \leq \lambda_z^+ \leq 3y_t^+$.

instance, the four simulations at $Re_\tau = 550$ have the same target height, y_t^+ , but different forcing heights, y_f^+ . Since the self-similar structures we aim to control are attached to the wall, we would expect that removing the target wavelengths from any height between the wall and the target height would, to some extent, disrupt their dynamics. Therefore, forcing at just one plane (e.g. case P550-150a) or at every height from the wall to that plane (e.g. case W550-150a) might provide some further insight into the effectiveness of this control strategy. In [table 5.1](#), the effect of the control is quantified in terms of ΔU^+ , which here is the difference between the controlled and uncontrolled mean velocity profiles at the channel centre, i.e. $\Delta U^+(y^+ = Re_\tau) = U_c^+(y^+ = Re_\tau) - U_0^+(y^+ = Re_\tau)$. As we will see later, far enough above the forcing region, ΔU^+ becomes essentially constant with y^+ , so the height at which ΔU^+ is measured is, to some extent, arbitrary.

| Case | Line style | Re_τ | y_t^+ | y_t/δ | y_f^+ | y_f/δ | ΔU^+ | $\Delta U^+/U_{\delta_0}^+$ |
|-----------|------------|-----------|---------|--------------|---------|--------------|--------------|-----------------------------|
| P360-150 | — | 360 | 150 | 0.42 | 100 | 0.28 | 0.22 | 0.011 |
| W360-150 | --- | 360 | 150 | 0.42 | 0–100 | 0–0.28 | 0.50 | 0.025 |
| P360-98 | -.-.- | 360 | 98 | 0.27 | 65 | 0.18 | 0.40 | 0.020 |
| W360-98 | | 360 | 98 | 0.27 | 0–65 | 0–0.18 | 1.20 | 0.060 |
| P550-150a | — | 550 | 150 | 0.27 | 100 | 0.18 | 0.39 | 0.019 |
| W550-150a | --- | 550 | 150 | 0.27 | 0–100 | 0–0.18 | 0.85 | 0.041 |
| P550-150b | -.-.- | 550 | 150 | 0.27 | 150 | 0.27 | 0.23 | 0.011 |
| W550-150b | | 550 | 150 | 0.27 | 0–150 | 0–0.27 | 0.69 | 0.033 |
| P950-150 | — | 950 | 150 | 0.16 | 100 | 0.10 | 0.46 | 0.020 |
| P950-259 | --- | 950 | 259 | 0.27 | 173 | 0.18 | 0.54 | 0.024 |
| B950-259 | -.-.- | 950 | 259 | 0.27 | 100–173 | 0.10–0.18 | 0.56 | 0.025 |

Table 5.1 Summary of the simulations with block forcing. The target height, y_t , is the nominal centre of gravity of the vortex cluster we wish to target and y_f is the wall-normal height, or heights, at which these wavelengths are removed. In all cases, the target wavelengths of the wall-normal velocity that we remove from the flow are $2 \leq \lambda_{x,t}/y_t \leq 6$ and $1 \leq \lambda_{z,t}/y_t \leq 3$. Here, the value of ΔU^+ is the difference between the controlled and uncontrolled mean velocity profiles measured at the channel centre, i.e. $\Delta U^+(y^+ = Re_\tau)$. $U_{\delta_0}^+$ is the centreline velocity of the uncontrolled flow at the same Re_τ . In the case names: ‘P’ denotes forcing only at one (P)lane; ‘W’ indicates that the forcing region extends down to the (W)all; ‘B’ indicates that forcing region spans a (B)and of wall-normal heights; the number before the dash corresponds to the friction Reynolds number; and the number after the dash corresponds to the target height in wall units.

5.1.1 Effect of the control on the mean velocity and turbulence

Mean statistics for all the cases in table 5.1 are shown in figure 5.2. The general effect of the control appears to be the same in all cases. We observe an increase in mean velocity above the forcing region, while the flow near the wall remains essentially unaffected, even when the forcing region extends all the way down to the wall, i.e. in cases W360-150, W360-98, W550-150a and W550-150b. Notably, while there are local changes in the r.m.s. velocity fluctuations and Reynolds shear stress in the vicinity of the target height, $y^+ \approx y_t^+$, these changes are small, particularly for $-\overline{u'v'}^+$. In the near-wall region and far enough above the target height, the turbulent fluctuations and Reynolds shear stress essentially collapse to the uncontrolled reference data.

In chapter 4, we have discussed the outward shift of the mean velocity profile, ΔU^+ , produced by a hypothetical control strategy that removed some or all of the Reynolds shear stress within the logarithmic layer, while leaving the rest of the flow unaffected. We noted that ΔU^+ would be constant above the controlled region in that case. In our block-forcing simulations, by removing energy from modes of v within the forcing region, we are thus removing energy from those same modes of the Reynolds stress uv , by definition. Therefore, we might expect that ΔU^+ would eventually become constant with y^+ , if the Reynolds shear stress indeed recovers to the uncontrolled profile. From figure 5.2(a, d, g), the outward shift in the

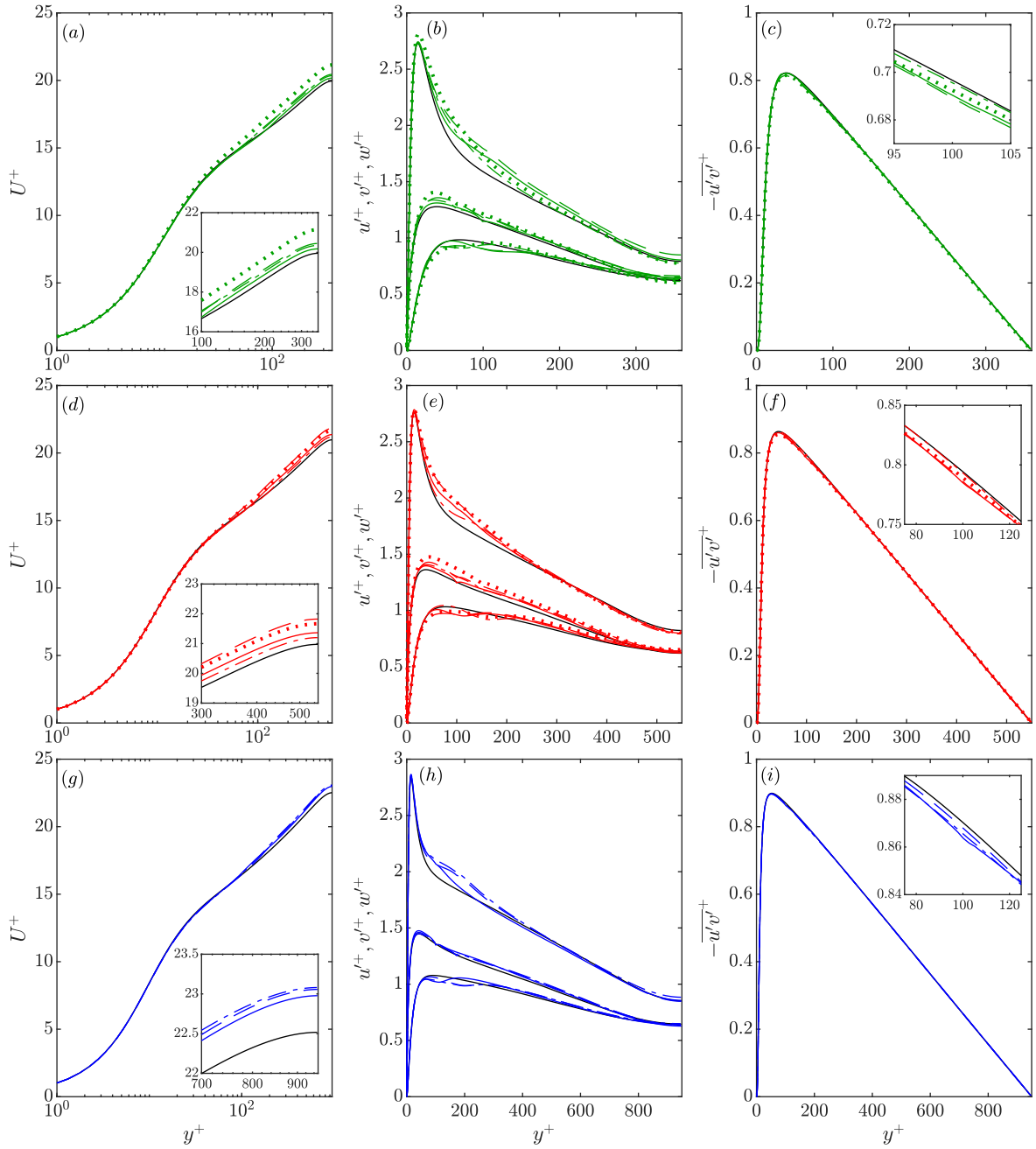


Figure 5.2 Mean statistics for block-forcing simulations (coloured lines), compared with those of the uncontrolled reference case (black lines). (a–c) $Re_\tau = 360$; (d–f) $Re_\tau = 550$; (g–i) $Re_\tau = 950$. See table 5.1 for simulation details. P360-150 (—); W360-150 (---); P360-98 (-.-.); W360-98 (.....); P550-150a (—); W550-150a (---); P550-150b (-.-.); W550-150b (.....); P950-150 (—); P950-259 (-.-.); B950-259 (---).

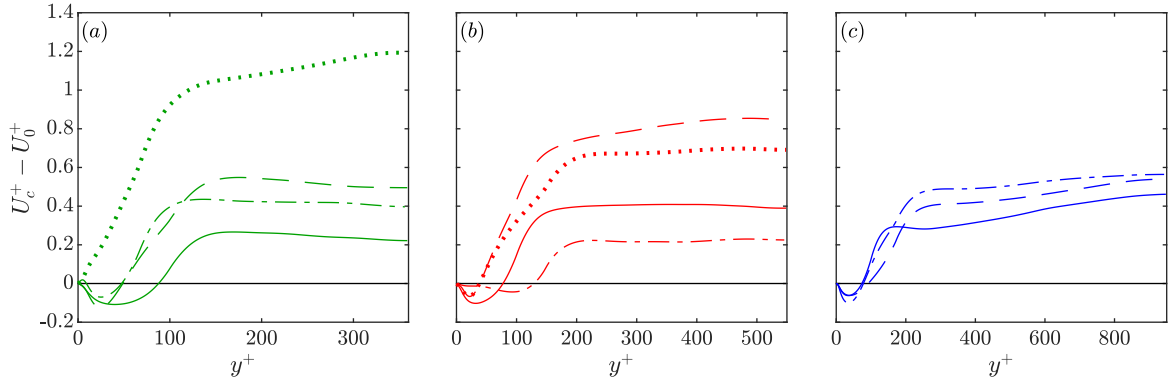


Figure 5.3 Difference between the controlled and uncontrolled mean profiles shown in figure 5.2 as a function of y^+ . (a) $Re_\tau = 360$; (b) $Re_\tau = 550$; (c) $Re_\tau = 950$. See table 5.1 for simulation details. P360-150 (—); W360-150 (---); P360-98 (-.-.); W360-98 (.....); P550-150a (—); W550-150a (---); P550-150b (-.-.); W550-150b (.....); P950-150 (—); P950-259 (---); B950-259 (-.-.).

mean velocity profile in the block-forcing simulations appears to become essentially constant with y^+ , far enough above the target height. We quantify this shift in terms of the difference $\Delta U^+(y^+) = U_c^+ - U_0^+$, where $U_c^+(y^+)$ and $U_0^+(y^+)$ are the controlled and uncontrolled mean velocity profiles, respectively. Figure 5.3 compares the variation of ΔU^+ with y^+ for each case, and shows that ΔU^+ eventually becomes approximately constant far enough above the target height and into the outer region of the flow. This, combined with the fact that the turbulent fluctuations and Reynolds shear stress in these regions are essentially unmodified by the control, suggests that the only effect of the control far enough above the target height is this additional mean velocity, while the dynamics of turbulence remain essentially the same as in the uncontrolled case. This will be discussed in more detail below.

Several of the simulations in table 5.1 have the same target height, y_t^+ , but different forcing regions, y_f^+ . The four cases at $Re_\tau = 550$ all have $y_t^+ = 150$, and thus the same modes are removed in each case, but their forcing regions are different. In case P550-150a the target length scales are removed from just one plane, $y_f^+ = 100$, whereas in case W550-100a they are removed from that plane all the way down to the wall, i.e. $y_f^+ = 0-100$. Similarly, cases P550-150b and W550-150b have $y_f^+ = 150$ and $y_f^+ = 0-150$, respectively. As mentioned above, since the self-similar structures we aim to control are attached to the wall, we would expect that removing the target wavelengths from any height between the wall and the target height would, to some extent, disrupt their dynamics. By varying the forcing region, we are thus able to investigate whether or not this is the case, and gain insight into the effect of the forcing region, for a given target height. As well as the four cases at $Re_\tau = 550$, there are two pairs of cases at $Re_\tau = 360$ that have the same forcing height but different forcing regions. These are cases P360-150 and W360-150 and cases P360-98 and W360-98. The first pair is designed to be consistent with cases P550-150a and W550-150a in inner units, while the second pair is designed to be consistent with them in outer units. Finally, case P950-259 and B950-259

also have the same target height but different forcing regions. In the former, $y_f/\delta = 0.18$, and in the latter, $y_f/\delta = 0.10-0.18$, which corresponds to forcing across a significant part of the logarithmic layer, but not into the buffer layer. Figure 5.3 shows that when the forcing region is thicker, the effect of the control is more pronounced. For instance, the value of ΔU^+ at the channel centre for case W550-150a, when the forcing region is $y_f^+ = 0-100$, is approximately twice that of case P550-150a, which has $y_f^+ = 100$. These cases are denoted by the solid and dashed lines in figure 5.3(b), respectively. Similar trends can also be observed for the other cases that have the same target height but different forcing regions. This suggests that when the forcing region reaches down to the wall, the control has a more robust effect on the attached structures that we aim to target. This is not surprising because if the structures are indeed attached, the target length scales, which are derived from the notional size of the structures themselves, should remain relatively active down into the buffer layer, until they are damped by viscosity. It is interesting to note, however, that the qualitative behaviour of ΔU^+ with y^+ is not significantly different when the target wavelengths are removed from only one plane, and the outward shift in the mean velocity profile still propagates to the channel centre. This suggests that the control still disrupts the dynamics of the target structures in these cases, but to a lesser extent.

Note that the value of ΔU^+ at the channel centre for case W360-98 (dotted line in figure 5.3a) is considerably larger than those of the other cases at the same Re_τ , and is, in fact, the largest of all the cases considered here. We will see later that because the target height is only just inside the logarithmic layer, $y_t^+ \approx 100$, some of the target wavelengths in this case coincide with the dominant length scales of the near-wall cycle, and so removing them disrupts the dynamics of the flow near the wall, at least to some extent. This is undesirable in terms of the aim of this chapter, which is to investigate the effect of controlling the flow in the logarithmic layer without directly affecting the flow elsewhere. However, this demonstrates that if the target height is too close to the wall, it is difficult to control the flow in the logarithmic layer without disrupting the dynamics of the buffer layer. We will discuss the effect of the control on the flow in the buffer layer in more detail below, and we will show that in general the control modifies the flow in the buffer layer very little, when the target height is $y_t^+ \gtrsim 150$. We also observe from figure 5.3(b) that the control appears to be less effective when the forcing region includes the target height y_t^+ (e.g. cases P550-150b and W550-150b), compared to those cases when the target length scales are removed from below the target height only (e.g. cases P550-150a and W550-150a). The reason for this is not immediately clear. However, it is possible that the length scales of v that we remove do not strictly correspond to the structures we originally aimed to target, but perhaps to structures centred at a different height below y_t^+ . As described above, the target wavelengths are chosen using an order-of-magnitude scale argument, based on the conditional attached structures observed in direct simulations of turbulent channels (del Álamo et al., 2006), and so it is expected that there will be some differences between the predicted and actual effect

of the control. It is therefore not surprising that this discrepancy arises, but this should not detract from the discussion on the general effect of the control strategy.

We further investigate the effect of changing the forcing region while keeping the target height fixed, by considering the distribution of energy among length scales for the cases at $Re_\tau = 550$. Figure 5.4 portrays the spectra for cases P550-150a and W550-150a at various heights from $y^+ = 100$ to $y^+ = 400$. In the former case, the forcing region is $y_f^+ = 100$, while in the latter case it is $y_f^+ = 0-100$. From the figure, we observe that the distribution of energy among length scales at the target height (panels *e-h*) is essentially the same for both controlled cases. This can be explained by considering that, from the point of view of the forced modes, there is an impermeable, slipping wall at top of the forcing region, $y^+ \approx 100$, even though the slip velocity they perceive on average is different in each case (figure 5.3*b*). Therefore, except for this difference in mean velocity, we would expect the effect on the turbulent fluctuations above this height to be similar in both cases. This is verified by the spectra farther from the wall (figure 5.4*i-t*). The same effect is observed for cases P550-150b and W550-150b, although their spectra are not shown here, with the impermeable, slipping wall perceived by the forced modes in those cases located at $y^+ \approx 150$. Note that the spectra for cases P550-150a and W550-150a shown in figure 5.4 collapse well to the uncontrolled reference data far enough above the forcing region, $y^+ \gtrsim 200$, which further suggests that the turbulence dynamics in the outer region of the flow are unmodified by the control, and the flow recovers outer-layer similarity (Townsend, 1976). This implies that the choice of forcing region does not have any effect on the flow in the outer region in these cases, except for the difference in mean velocity discussed above (figure 5.3*b*). This is generally true of all the block forcing simulations presented here, and will be discussed in more detail below.

Even though the forcing is applied only to certain modes of v , with the aim of removing those modes of uv , we see from figure 5.4 that the effect on the flow is not limited to the target length scales, and the other components of the flow also exhibit differences compared to the uncontrolled case. For example, while we observe only a small change in the magnitude of the Reynolds shear stress $\overline{u'v'^+}$ in the forcing region (figure 5.2*f*), it is now redistributed to larger wavelengths, as shown in figure 5.4(*d*). The spectra of u^2 and w^2 also exhibit changes in the distribution of energy among length scales at that height compared to the uncontrolled flow (figure 5.4*a, c*), even though the forcing only removes energy directly from wavelengths of v^2 . This can be seen more clearly from figure 5.5, which portrays the difference in energy across length scales between case P550-150a and the uncontrolled case in the forcing region at $y^+ = 100$. This is caused by the nonlinear scale interaction in Fourier space, i.e. (k_x, k_z) space, that arises due to the advective terms of the Navier–Stokes equations (2.1), $\mathbf{u} \cdot \nabla \mathbf{u}$. As discussed in section 2.4, each Fourier mode (k_x, k_z) is related to its pair of wavelengths by $(\lambda_x, \lambda_z) = (L_x/|k_x|, L_z/|k_z|)$, where L_x and L_z are the size of the computational domain in the streamwise and spanwise directions. Setting certain wavelengths of v to zero has a direct effect on other wavelengths, and not just of v but also of u and w , due to terms such as $v \partial u / \partial x$

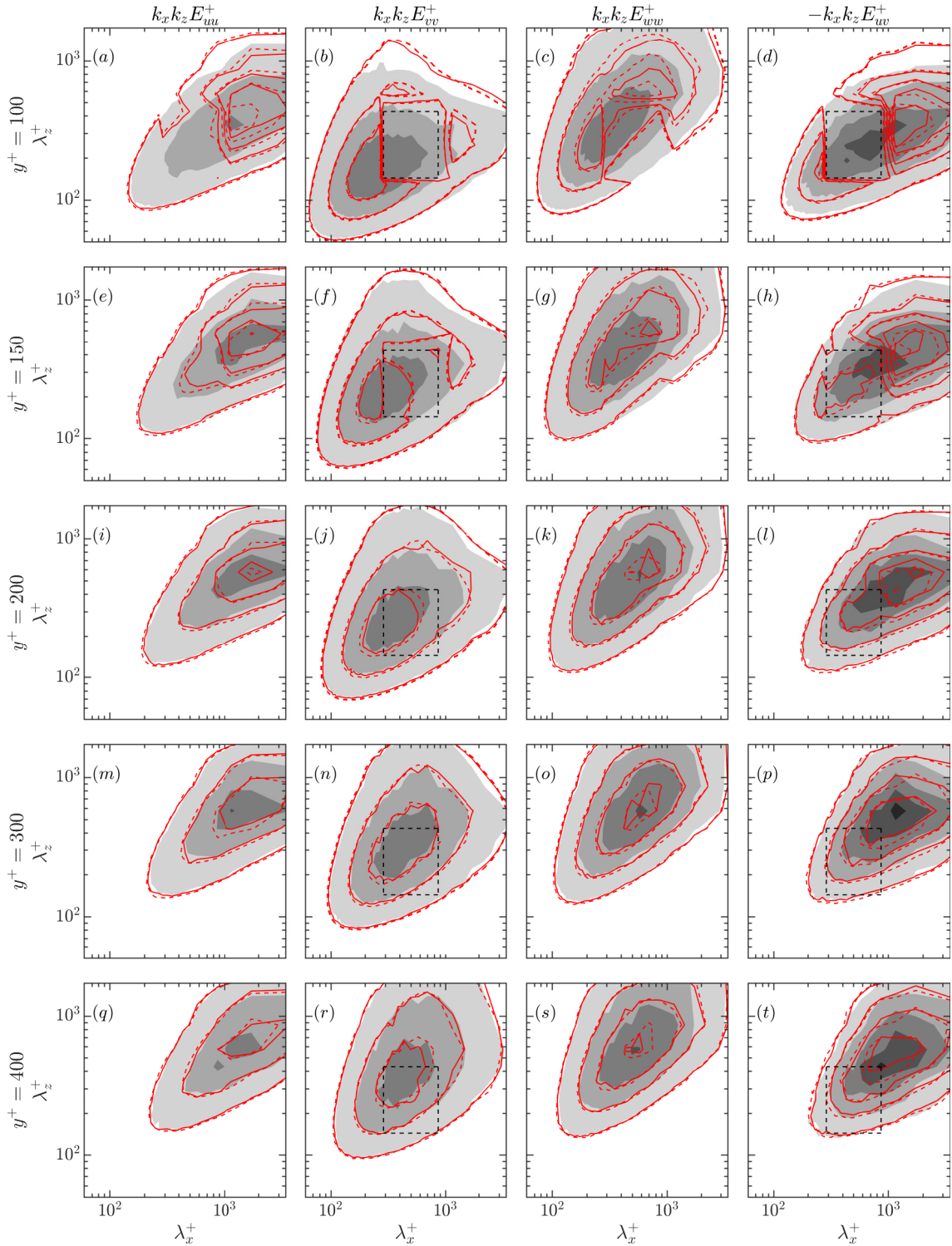


Figure 5.4 Premultiplied two-dimensional spectral densities of u^2 , v^2 , w^2 and uv for cases P550-150a (—) and W550-150a (---) compared to the uncontrolled case (filled contours) at (a–d) $y^+ = 100$, (e–h) $y^+ = 150$, (i–l) $y^+ = 200$, (m–p) $y^+ = 300$ and (q–t) $y^+ = 400$. The black dashed line encloses the wavenumbers of v that are removed from the flow in the forcing region, y_f^+ .

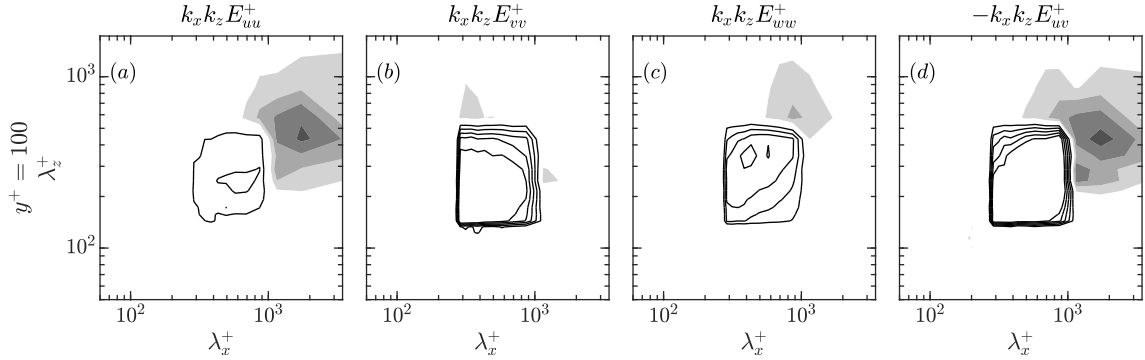


Figure 5.5 Difference between the premultiplied two-dimensional spectral densities of case P550-150a and the uncontrolled case at in the forcing region at $y^+ = 100$. Filled contours denote wavelengths for which the difference is positive, i.e. more energy in the controlled flow, whereas the line contours denote wavelengths for which the difference is negative, i.e. less energy in the controlled flow. Note that, to make this difference clearer, the contour levels in this figure are half that of figure 5.4.

being a convolution in (k_x, k_z) space. Eventually, this results in a wide-spectrum modification to all velocity components of the flow.

Using case P550-150a as an example, we now discuss why targeting length scales of v at just one plane within the logarithmic region generates an outward shift in the mean velocity profile above this height, without affecting the turbulence farther from the wall. To do this we compare the contributions of the viscous and Reynolds shear stresses to the total stress curve in case P550-150a with that of the uncontrolled flow, as shown in figure 5.6(b). The total stress curve must still remain linear in this case and is defined by equation (4.1). The figure shows that there is a small deficit in Reynolds shear stress in the vicinity of the forcing region, caused directly by the removal of energy from v . It is interesting to note that the target wavelengths contribute to approximately 23% of $\overline{u'v'^+}$ in the uncontrolled flow at $y^+ = 100$, but the actual drop in $\overline{u'v'^+}$ is of order 1% only. This suggests that the flow is very robust to the control, and we will discuss this idea further in section 5.3. This drop in Reynolds stress is then balanced by a local increase in viscous stress dU^+/dy^+ (figure 5.6b), which explains why there is a sudden increase in the mean velocity at $y^+ \approx 100$ (figure 5.6a). Above the forcing region, the viscous and Reynolds shear stresses recover to uncontrolled values, and so the shape of the mean velocity profile, i.e. dU^+/dy^+ , returns to that of the uncontrolled case. This strongly suggests that the control does indeed produce a simple shift ΔU^+ , far enough above the forcing region. This is further supported by the fact that, for large enough y^+ , the premultiplied energy spectra eventually exhibit the same distribution of energy among length scales as the uncontrolled case, as mentioned above and shown in figure 5.4. This indicates that turbulence is essentially unchanged and the flow merely experiences an additional mean velocity, suggesting that turbulence far enough from the wall recovers outer-layer similarity (Townsend, 1976). The mechanism just described is common for all the block-forcing simulations presented

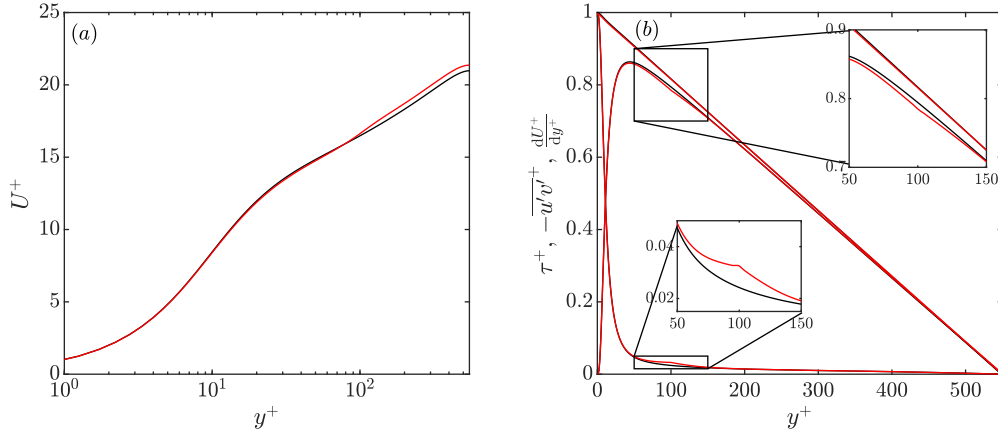


Figure 5.6 Additional statistics for case P550-150a: (a) mean velocity profile for case P550-150a (red line) compared to uncontrolled case (black line); (b) total stress, viscous stress and Reynolds stress for case P550-150a (red lines) and uncontrolled case (black lines).

here. That is, regardless of the thickness of the forcing region, the flow in the outer region recovers outer-layer similarity. Figure 5.7 portrays the premultiplied two-dimensional spectra in the outer layer at $y/\delta = 0.7$ for all the block forcing simulation, and demonstrates that, except for a small amount of statistical noise, the spectra collapse very well to the uncontrolled data for u^2 , v^2 , w^2 and uv , consistent with the eventual collapse of the mean statistics presented earlier in figure 5.2.

We now investigate further the effect of the control on the flow in the buffer layer. The premultiplied energy spectra at $y^+ = 15$ for all cases are portrayed in figure 5.8. The figure shows that when modes are removed only at one plane in the logarithmic layer, there is essentially no change in the distribution of energy among length scales near the wall, compared to the uncontrolled flow. This can be observed from the spectra of case P360-150, case P360-98, case P550-150a, and the three cases at $Re_\tau = 950$. On the other hand, when the forcing region extends down to the wall, we see a more noticeable change in the distribution of energy in the spectra, since the removed modes contain some energy near the wall, as can be seen in cases W360-150, W360-98 and W550-150a. This might suggest that the observed increase in mean velocity (figure 5.3) in these cases is caused, at least in part, by a modification of dynamics of the flow in the buffer layer. However, the overall effect on the near-wall dynamics remains relatively small, as confirmed by the fact that the mean velocity profile, r.m.s. fluctuations and Reynolds shear stress are essentially unmodified near the wall, as shown in figure 5.2. This demonstrates, therefore, that the observed modifications to the spectra in the buffer layer is not significant in terms of overall change in the mean velocity profile. The reason for this is that, while the removed v length scales are some of the most energetic within the logarithmic region, they do not contain a significant amount of energy near the wall. Indeed, for cases W360-150 and W550-150a, the block of removed modes overlaps only slightly with the main lobe of the

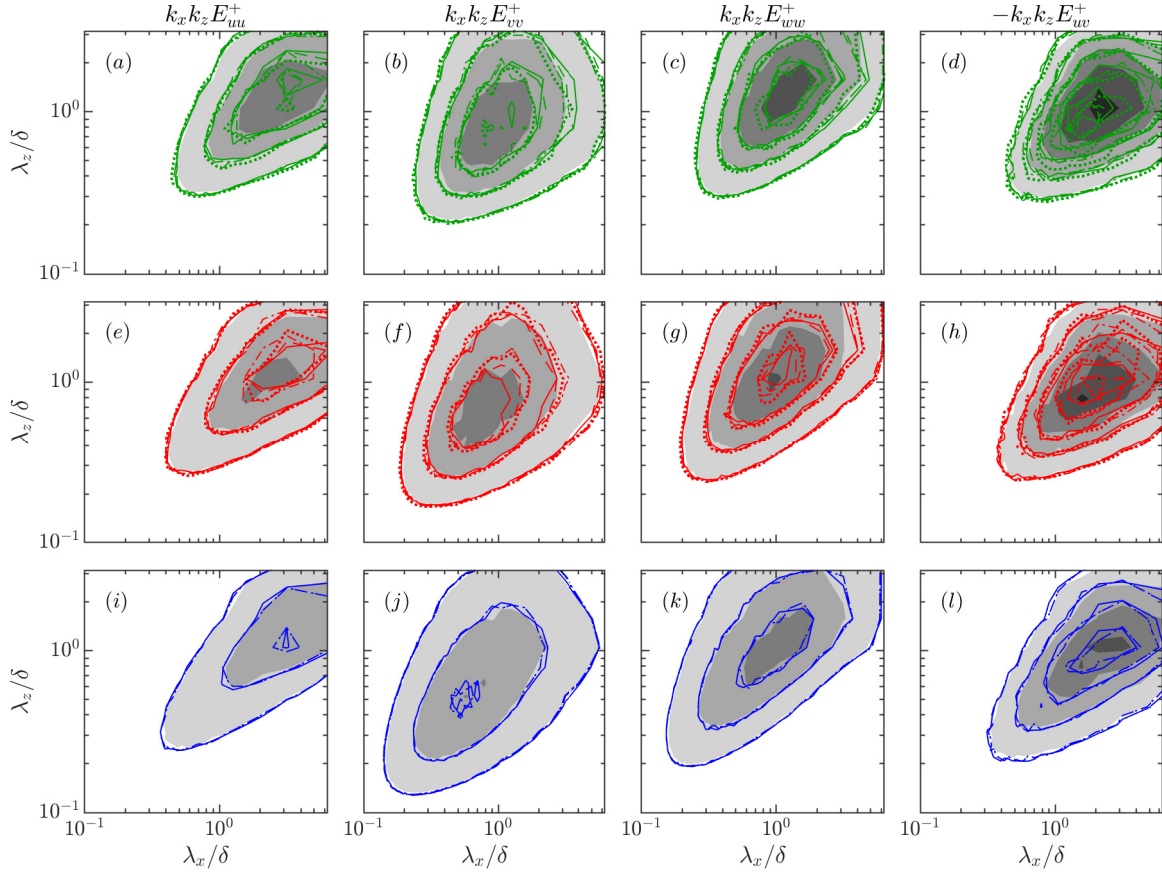


Figure 5.7 Premultiplied two-dimensional spectral densities of u^2 , v^2 , w^2 and wv at $y/\delta = 0.7$ for cases at $Re_\tau = 360$ ($a-d$), $Re_\tau = 550$ ($e-h$) and $Re_\tau = 950$ ($i-l$), compared to the uncontrolled case (filled contours). Note that the axes in this figure are the streamwise and spanwise wavelengths scaled in outer units, i.e. λ_x/δ and λ_z/δ . See table 5.1 for simulation details. P360-150 (—); W360-150 (---); P360-98 (-.-.); W360-98 (⋯); P550-150a (—); W550-150a (---); P550-150b (-.-.); W550-150b (⋯); P950-150 (—); P950-259 (---); B950-259 (-.-.).

spectrum of v^2 , as shown in figure 5.8(b, j). The above behaviour can also be observed for cases P550-150b and W550-150b, although their near-wall spectra and snapshots are not shown here, because they are not qualitatively different near the wall to those of cases P550-150a and W550-150a, shown in figure 5.8($i-l$). In figure 5.9, we also compare snapshots of the wall-normal velocity at $y^+ = 15$ for the uncontrolled flow and cases P550-150a and W550-150a. We see that there is no qualitative change in v at $y^+ = 15$ for the controlled cases, even when the forcing region extends down to the wall, as shown in figure 5.9(c). We note, however, that for case W360-98, the removed v modes contain more energy at $y^+ = 15$, and the spectra of v^2 and wv are modified more noticeably (figure 5.8(f, h)). In this case, the target height lies only just within the logarithmic layer, $y_t^+ \approx 100$, and so the target length scales are comparable in size to the dominant ones of the near-wall cycle. Removing these scales in the region $y_f^+ = 0-65$ thus

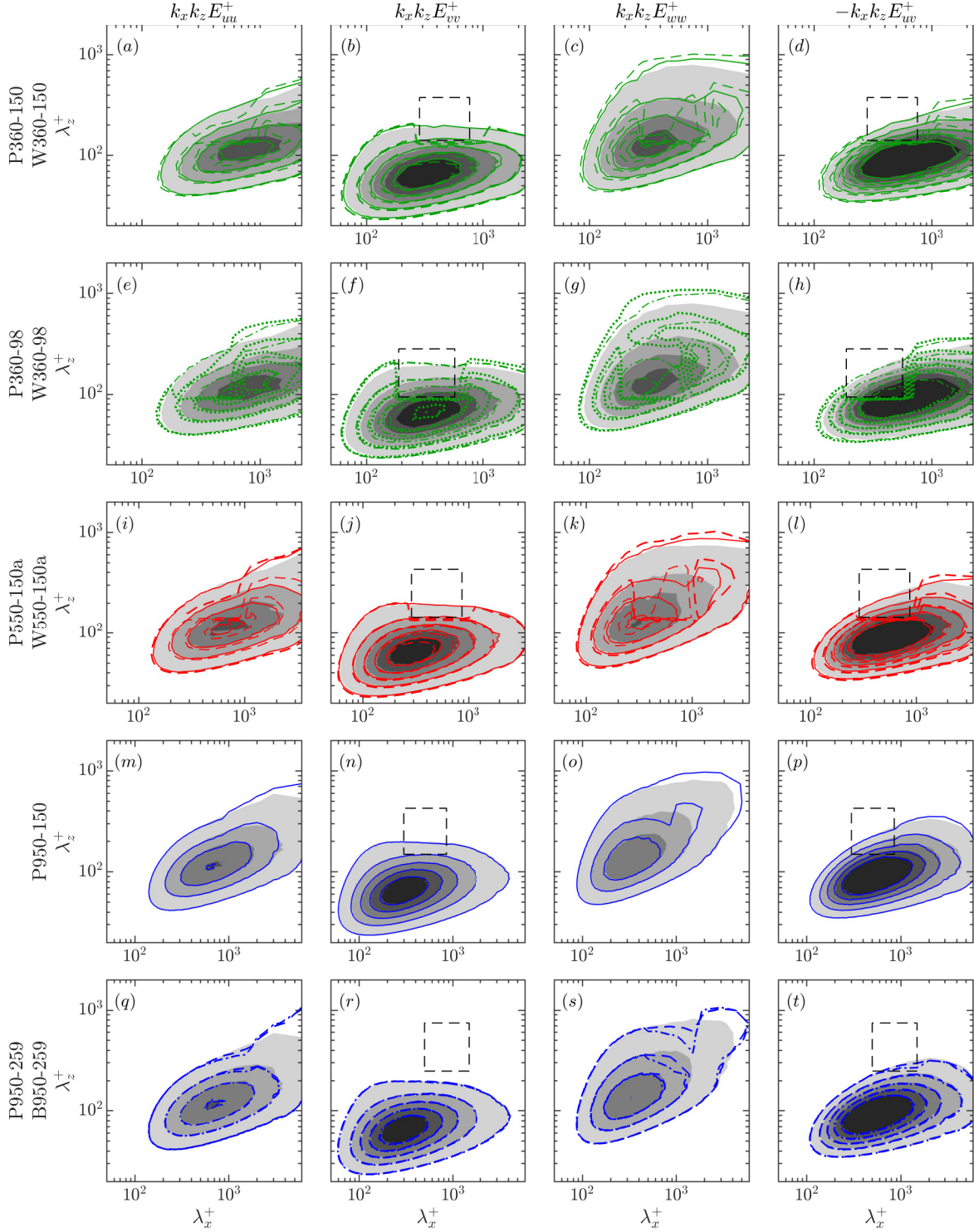


Figure 5.8 Premultiplied two-dimensional spectral densities of u^2 , v^2 , w^2 and uv plotted at $y^+ = 15$ for (a–d) cases P360-150 (—) and W360-150 (---), (e–h) cases P360-98 (— · —) and W360-98 (·····), (i–l) P550-150a (—) and W550-150a (---), (m–p) case P950-150 (—) and (q–t) cases P950-259 (---) and B950-259 (---), all compared to the uncontrolled case at the same height. Filled contours, uncontrolled case; red lines, controlled cases. See table 5.1 for simulation details. The black dashed rectangle encloses the wavelengths of v that are removed from the flow in the forcing region, y_f^+ . Spectra for cases P550-150b and W550-150b are not shown here, because at $y^+ = 15$ they are not qualitatively different to the spectra of P550-150a and W550-150a, respectively.

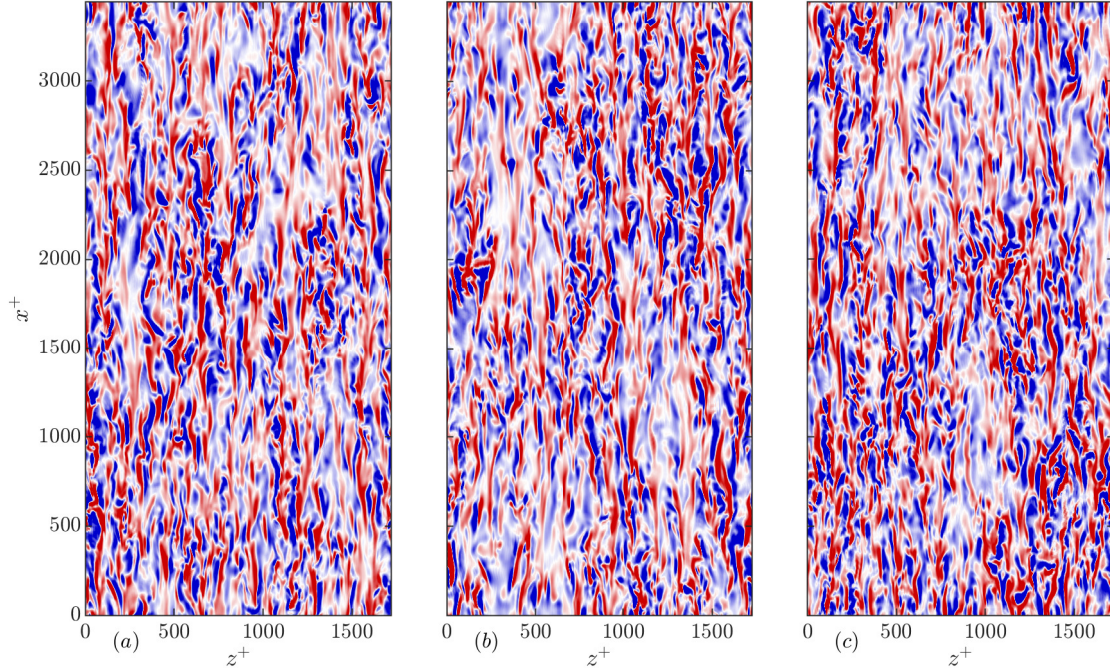


Figure 5.9 Instantaneous snapshots of v^+ at $y^+ = 15$ for the uncontrolled case (a), case P550-150a (b) and case W550-150a (c). Blue to red corresponds to $v^+ = [-0.75, 0.75]$.

suppresses the dynamics of the near-wall cycle, at least to some extent, as well as controlling the flow in the logarithmic layer. This explains why this case has the largest ΔU^+ of all the cases considered here, as discussed above and shown in figure 5.3(a).

In summary, we have seen that it is possible to control the flow in the logarithmic layer alone using the present control strategy, without directly modifying the flow in the buffer or outer layers. The control generates a deficit in Reynolds shear stress in the forcing region, and thus there is a local increase in viscous stress, which causes an outward shift of the mean velocity profile ΔU^+ . We have investigated the effect of varying the thickness of the forcing region while keeping the target height fixed, and found that when the forcing region is thicker, the effect of the control is more pronounced. However, we observed that, in hindsight, the removed wavelengths likely do not correspond exactly to the structures we originally aimed to target, but rather to structures centred at a different height below y_t^+ , and hence the control was more effective when the forcing region was below y_t^+ . We also noted that if the nominal target height of the attached vortex clusters is too close to the wall, the removed length scales can coincide with the dominant length scales of the near-wall cycle, and the dynamics in the buffer layer can be disrupted if the forcing region extends down to the wall (see e.g. case W360-98). This case had the largest value of ΔU^+ , but we argued that this was due to the additional effect of controlling the buffer layer, as well as the logarithmic layer. In all cases, far enough above

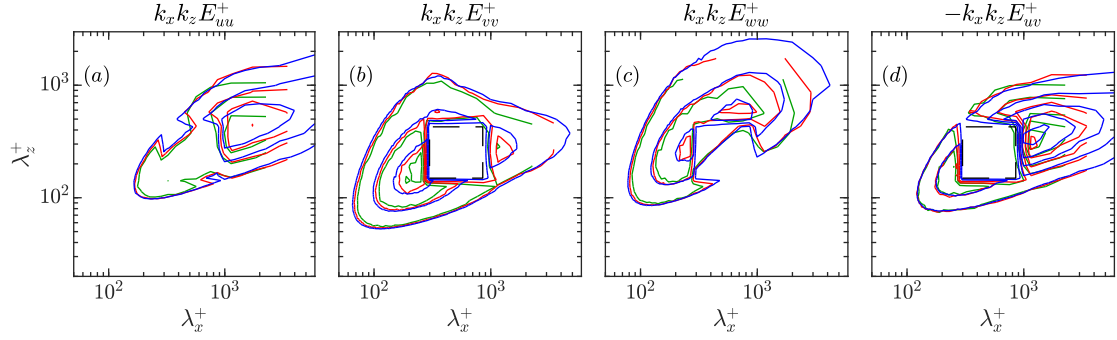


Figure 5.10 Premultiplied two-dimensional spectral densities of u^2 , v^2 , w^2 and uv at $y^+ = y_f^+ = 100$ for cases P360-150 (—), P550-150a (—) and P950-150 (—), in which the control strategy is consistent in inner units. The black dashed line encloses the wavelengths of v that are removed from the flow in the forcing region.

the target height, we observe that the dynamics of turbulence are unmodified compared to the uncontrolled case, and the flow recovers outer-layer similarity (Townsend, 1976).

5.1.2 Comparison of cases at different Re_τ

As mentioned above, some of the block-forcing simulations at different Reynolds numbers are designed such that the target length scales and forcing regions are consistent in either inner or outer units. The idea is to provide insight into the effect of Reynolds number on the control strategy. Here, we compare and discuss two groups of simulations. The first group consists of cases P360-150, P550-150a and P950-150, which all have the same target height and forcing region in wall units, $y_t^+ = 150$ and $y_f^+ = 100$, and so the target length scales are the same when measured in wall units, as can be seen in figure 5.10(b, d). On the other hand, the second group of simulations, cases P360-98, P550-150a and P950-259, have the same target height and forcing region in outer units, $y_t/\delta = 0.27$ and $y_f/\delta = 0.18$. In this second group, the target length scales are the same when measured in outer units, as shown in figure 5.11(b, d).

In order to assess the effect of Reynolds number, we consider the behaviour of both ΔU^+ and $\Delta U^+/U_{\delta_0}^+$ with Re_τ . These metrics are portrayed in figure 5.12(a) for the simulations that are consistent in inner units, and in figure 5.12(b) for the simulations that are consistent in outer units. By definition, ΔU^+ provides a measure of the effect of the control in inner units. This is the universal metric for measuring the effect of buffer-layer control strategies, but, as discussed in chapter 1, the drag reduction will degrade with Re_τ for fixed ΔU^+ . In turn, taking $U_{\delta_0}^+$ as the centreline velocity of the uncontrolled case, $\Delta U^+/U_{\delta_0}^+$ can be viewed as a measure of the flow in outer units, since it represents the relative increase in the channel centreline velocity due to the control. This was discussed in detail in chapter 4. In the first group of simulations, since the target length scales and forcing plane are consistent in inner units, we might expect ΔU^+ to remain essentially constant with Re_τ , and $\Delta U^+/U_{\delta_0}^+$ would thus

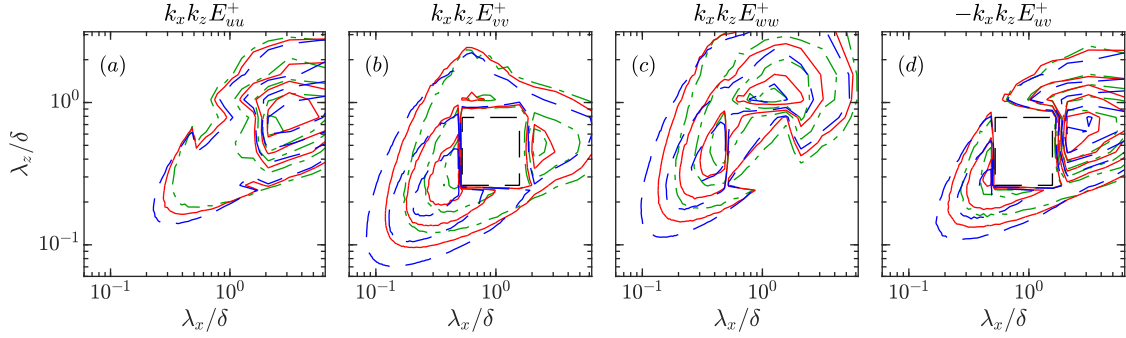


Figure 5.11 Premultiplied two-dimensional spectral densities of u^2 , v^2 , w^2 and uv at $y/\delta = y_f/\delta = 0.18$ for cases P360-98 (---), P550-150a (—) and P950-259 (---), in which the control strategy is consistent in outer units. Note that the axes in this figure are the streamwise and spanwise wavelengths scaled in outer units, i.e. λ_x/δ and λ_z/δ . The black dashed line encloses the wavelengths of v that are removed from the flow in the forcing region.

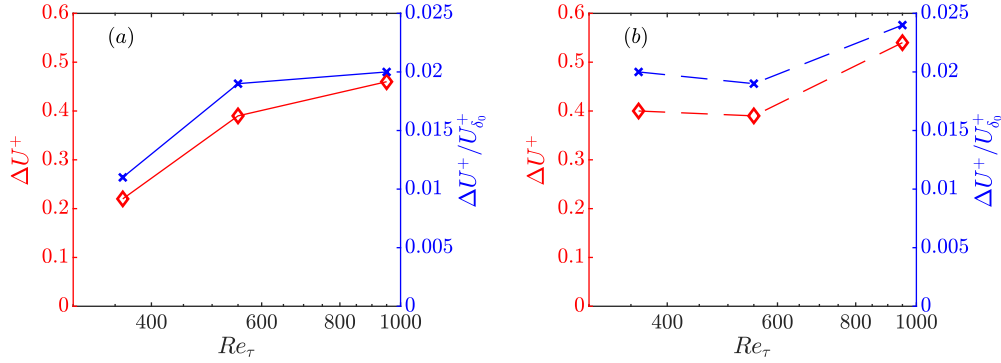


Figure 5.12 ΔU^+ (red lines with diamonds) and $\Delta U^+/U_{\delta_0}^+$ (blue lines with crosses) as a function of Re_τ for (a) simulations with forcing consistent in inner units and (b) simulations with forcing consistent in outer units.

diminish due to the increase in $U_{\delta_0}^+$ with Re_τ . Following similar arguments, in the second group of simulations, where the control is consistent in outer units, we might expect that $\Delta U^+/U_{\delta_0}^+$ remains essentially constant with Re_τ , and thus ΔU^+ would increase. However, the results of our simulations suggest that both ΔU^+ and $\Delta U^+/U_{\delta_0}^+$ increase with Re_τ for both groups of simulations, as shown in figure 5.12, although this trend is less pronounced when the forcing is consistent in outer units (panel b).

To further investigate the effect of the control, figure 5.13 portrays the proportion, ϕ , of the Reynolds shear stress contained in the target length scales at $y^+ = y_t^+$ in the uncontrolled flow, and the actual, relative reduction in the total Reynolds shear stress, $\Delta \overline{u'v'}/\overline{u'v'_0}$, at the same height in the controlled flow. Here, $\overline{u'v'_0}$ is the Reynolds shear stress of the uncontrolled flow, and $\Delta \overline{u'v'} = \overline{u'v'_0} - \overline{u'v'_c}$, where the ‘c’ subscript denotes the controlled case. The figure demonstrates that in both groups of simulations, the proportion of $\overline{u'v'_0}$ contained in the target

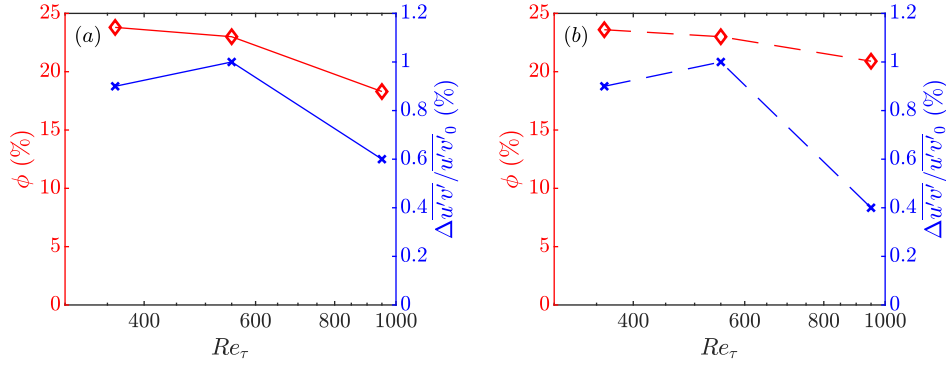


Figure 5.13 Proportion, ϕ , of Reynolds shear stress contained in the target length scales at $y^+ = y_t^+$ in the uncontrolled flow (red lines with diamonds) and actual, relative reduction in Reynolds shear stress, $\Delta \overline{u'v'}/\overline{u'v'_0}$, at $y^+ = y_t^+$ in the controlled flow (blue lines with crosses) as a function of Re_τ for (a) simulations with forcing consistent in inner units and (b) simulations with forcing consistent in outer units.

length scales decreases with increasing Re_τ , although it decreases more slowly when the control is consistent in outer units (figure 5.13b). This behaviour can be explained in terms of the attached-eddy framework discussed in section 1.3.2. As Re_τ increases, the separation of scales between the smallest and largest attached eddies in the logarithmic layer also increases. For a fixed height in wall units, y_t^+ , the largest attached eddies become larger as Re_τ increases, and so the Reynolds shear stress at that height will have contributions from larger length scales in wall units. However, if we consider a fixed height in outer units, y_t/δ , the size of the largest attached eddies is fixed, but the scales at which dissipation occurs become smaller in outer units as Re_τ increases (see e.g. Jiménez, 2012). As a result, in both of these cases (fixed y_t^+ or fixed y_t/δ), the Reynolds shear stress will have contributions from a broader range of length scales as Re_τ increases. It makes sense, therefore, that the proportion of $\overline{u'v'_0}$ contained in the target length scales in our simulations would decrease with Re_τ . However, we also see from figure 5.13 that the actual, relative reduction in $\overline{u'v'}$ in the controlled flow is much smaller than ϕ and varies between Reynolds numbers. This makes it difficult to compare the results at different Reynolds numbers, because even though the forcing regions and target length scales are consistent in either inner or outer units as Re_τ varies, the actual effect of the control is not. While we cannot, therefore, draw solid conclusions about the effect of the Reynolds number on the control strategy, it is interesting to note that the flow appears to be very robust to this kind of control. In our simulations we target approximately 20% of the uncontrolled Reynolds shear stress but we observe only a 1% reduction in the controlled flow. As mentioned above, the Reynolds shear stress originally contained in the target length scales appears to be redistributed to larger streamwise and spanwise wavelengths. For the cases discussed here, this can be seen in figures 5.10(d) and 5.11(d), which illustrates how the flow is so robust to the control. We will discuss this ‘robustness’ in more detail in section 5.3.

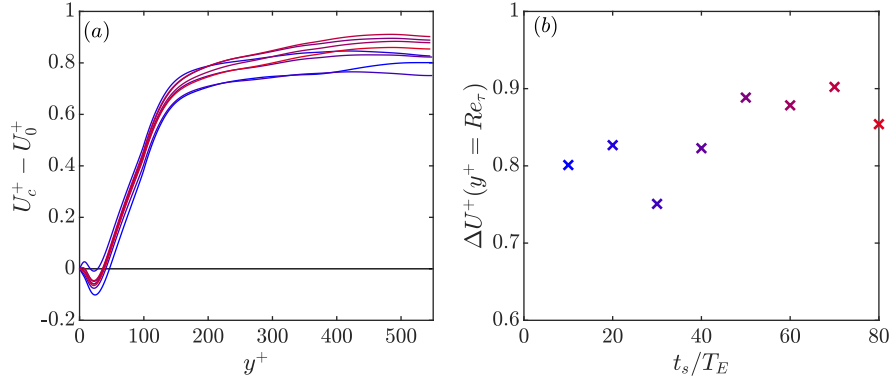


Figure 5.14 Sensitivity of ΔU^+ to the number of largest-eddy turnover times, T_E , over which statistics are collected for case W550-150a. (a) ΔU^+ as a function of y^+ for different t_s/T_E , where t_s is the time-window over which statistics are collected. Blue to red lines, $t_s/T_E = [10, 20, 30, 40, 50, 60, 70, 80]$. (b) ΔU^+ measured at the channel centre as a function of t_s/T_E .

Finally, we also note that $\Delta U^+ \lesssim 0.5$ for the cases shown in figures 5.12 and 5.13, and ΔU^+ is at most 1.2 in any of the block forcing cases presented in this section. In each case, time-averaged statistics have been collected over at least 30 largest-eddy turnover times, $T_E = \delta/u_\tau$. While this is sufficient to provide a good representation of the mean velocity profile, r.m.s. fluctuations and Reynolds shear stress, because ΔU^+ is small it could be sensitive to any statistical uncertainty. This can be appreciated from figure 5.14, which illustrates the sensitivity of ΔU^+ to the time-window, t_s , over which statistics are collected for case W550-150a. The figure shows that the difference between the smallest and largest value of ΔU^+ is $\mathcal{O}(0.2u_\tau)$, which is small in absolute terms, but large relative to the measured value. Note that the value of ΔU^+ at $t_s/T_E = 80$ is more than 10% larger than at $t_s/T_E = 30$ (figure 5.14b), and while ΔU^+ appears to stabilise for $t_s/T_E \gtrsim 50$, it still continues to fluctuate by about 5% beyond this point. These differences are caused by the natural variation of the mean velocity profile in the outer region, due to long time scales of the dynamics of the largest eddies, $\mathcal{O}(T_E)$. Therefore, when ΔU^+ is small, as it is in our block-forcing simulations, the figure shows that very long time-averaging windows ($t_s/T_E \gtrsim 100$) are required to measure accurately ΔU^+ at the channel centre. This is another reason why it is difficult to draw firm conclusions on the effect of Reynolds number in our block-forcing simulations. We will see in section 5.2 that ΔU^+ is typically larger in the simulations with hierarchical forcing. This will allow us to draw more solid conclusions on the effect of Reynolds number, because the natural variation of ΔU^+ is less significant relative to the actual value.

5.2 Simulations with hierarchical forcing

In order to avoid the problems associated with small values of ΔU^+ described above, in this section we conduct a second group of simulations in which the control is more intrusive, and thus

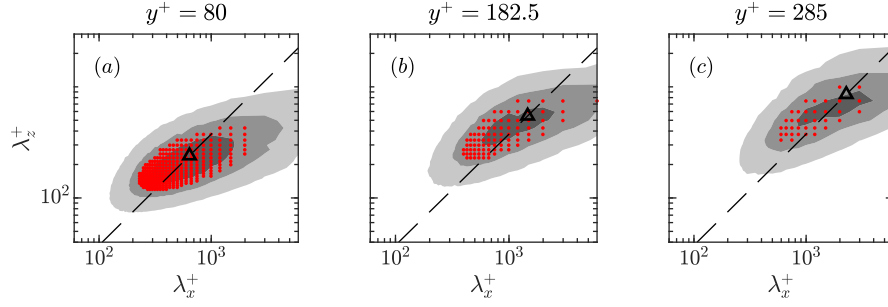


Figure 5.15 Premultiplied two-dimensional spectral density of uv , normalised by $u_\tau^2, -k_x k_z E_{uv}^+$, within the logarithmic layer for an uncontrolled channel at $Re_\tau = 950$. (a) at the bottom limit of logarithmic layer, $y^+ = 80$; (b) in the middle of the logarithmic layer, $y^+ = 182.5$; (c) at the top limit of the logarithmic layer, $y^+ = 0.3Re_\tau = 285$. The red dots denote the target wavelengths at each height. In this example, summing the contribution to uv of the target wavelength is equal to 30% of the Reynolds shear stress at each height. Note that only three wall-parallel planes are shown here, but this procedure is carried out for every plane in the forcing region. The dash lines in each panel are $\lambda_z^+ = 3\lambda_x^+/8$, which is consistent with the streamwise-to-spanwise aspect ratio of the self-similar Q^- , defined in section 1.3.2 (Lozano-Durán et al., 2012). The black triangles denote $(\lambda_x^+, \lambda_z^+) = (8y^+, 3y^+)$, where y^+ corresponds to the height at which the spectra are shown.

ΔU^+ should be larger. In these simulations, the forcing region spans either the whole logarithmic layer or a significant part of it, and the length scales of v that we remove vary with y . For each plane within the forcing region, the removed scales are contiguous in (λ_x, λ_z) space, but tend to larger values as y increases, and we thus refer to them as simulations with ‘hierarchical forcing’. In contrast to the order-of-magnitude arguments used to determine the target wavelengths in the block-forcing simulations, the target wavelengths in the hierarchical-forcing simulations are chosen by analysing the distribution of energy among length scales within the logarithmic layer in uncontrolled reference flows. The target wavelengths of v correspond to the length scales that contribute the most to uv at each height within the forcing region. From figure 5.15, we see that the central lobe of the spectrum of uv moves to larger streamwise and spanwise wavelengths as y^+ increases, meaning that the target wavelengths should also vary with y^+ , tending towards larger values of λ_x^+ and λ_z^+ . To make the choice of target wavelengths consistent across the forcing region, we choose the most dominant wavelengths of the premultiplied spectrum of uv , whose contribution at each height is equal to a fixed proportion, ϕ , of the uncontrolled Reynolds shear stress, $\overline{u'v'}_0^+$. Take, for example, the case where we wish to target 30% of $\overline{u'v'}_0^+$ across the whole logarithmic layer at $Re_\tau = 950$. Figure 5.15 illustrates the wavelengths that satisfy this condition for three wall-parallel planes within the logarithmic layer. While the spectra is shown only at three wall-parallel planes, this is repeated at every height within the logarithmic layer, which provides a list of target wavelengths at each height. These wavelengths are then removed from the wall-normal velocity in the DNS. In general, this procedure can be carried out for simulations at different Reynolds numbers, with different choices of forcing region or proportions of $\overline{u'v'}_0^+$. As mentioned above, the idea is that this more targeted form of control should have a more significant effect on the flow, and ΔU^+ should be larger than in the

| Case | Line style | Re_τ | ϕ (%) | $y_{f,min}^+$ | $y_{f,max}^+$ | $y_{f,min}/\delta$ | $y_{f,max}/\delta$ | ΔU^+ | $\Delta U^+/U_{\delta_0}^+$ |
|----------|------------|-----------|------------|---------------|---------------|--------------------|--------------------|--------------|-----------------------------|
| L360-30 | — | 360 | 30 | 80 | 108 | 0.222 | 0.3 | 0.43 | 0.022 |
| O360-30 | - - - | 360 | 30 | 52 | 108 | 0.145 | 0.3 | 1.18 | 0.059 |
| L550-30 | — | 550 | 30 | 80 | 165 | 0.145 | 0.3 | 1.21 | 0.058 |
| L550-50 | ⋯ | 550 | 50 | 80 | 165 | 0.145 | 0.3 | 1.46 | 0.070 |
| L950-30 | — | 950 | 30 | 80 | 285 | 0.084 | 0.3 | 2.27 | 0.101 |
| O950-30 | - - - | 950 | 30 | 136 | 285 | 0.145 | 0.3 | 1.10 | 0.049 |
| L2000-30 | — | 2000 | 30 | 80 | 600 | 0.040 | 0.3 | (3.38) | (0.139) |
| O2000-30 | - - - | 2000 | 30 | 290 | 600 | 0.145 | 0.3 | (0.66) | (0.027) |

Table 5.2 Summary of the simulations with hierarchical forcing. The proportion ϕ refers to the total contribution to the Reynolds shear stress of the target length scales in the uncontrolled flow. The heights $y_{f,min}$ and $y_{f,max}$ are the bottom and top limits of the forcing region, respectively. Here, ΔU^+ is the difference between the controlled and uncontrolled mean velocity profiles at the channel centre, and $U_{\delta_0}^+$ is the centreline velocity for the uncontrolled reference case at the same Re_τ . In the case names, ‘L’ denotes forcing of the whole (L)ogarithmic layer, with $y_{f,min}^+ = 80$ and $y_{f,max}^+ = 0.3Re_\tau$, ‘O’ signifies that the forcing region is consistent in (O)uter units with case L550-30, with $y_{f,min}/\delta = 0.145$ and $y_{f,max}/\delta = 0.3$, the number before the hyphen is equal to Re_τ , and the number after the hyphen denotes the percentage of uv targeted within the forcing region (ϕ). Note that the two simulations at $Re_\tau = 2000$, cases L2000-30 and O2000-30, are somewhat under-resolved in time ($t_s/T_E \approx 15$), compared to the cases at lower Reynolds numbers. Therefore, their values of ΔU^+ and $\Delta U^+/U_{\delta_0}^+$ are tentative, and are placed in parentheses to reflect this.

block-forcing simulations. The hierarchical-forcing simulations are also conducted at a wider range of Reynolds numbers, including cases at $Re_\tau = 2000$. This should give further insight into the effect of Reynolds number on the control. It is important to emphasise that this approach is based on raw data from uncontrolled reference flows, and is thus not derived from any analysis of the physics mechanisms at play (e.g. scaling arguments, or self-similarity), as was done in the block-forcing simulations in section 5.1. However, we observe from figure 5.15 that the length scales contributing the most to uv , denoted by the central lobe in each panel, respect the aspect ratio of the self-similar, wall-attached Reynolds stress (Q^-) structures discussed in section 1.3, where $\lambda_z^+ \approx 3\lambda_x^+/8$ (Lozano-Durán et al., 2012). Therefore, targeting the central lobe of the spectrum in our hierarchical forcing simulations might also provide insight into the effect of controlling structures of this kind.

The simulations conducted in this section are summarised in table 5.2, and can be split into two main groups. The first group consists of cases L360-30, L550-30, L950-30 and L2000-30, all of which target 30% of uv across the whole logarithmic layer. The lower limit of the forcing region in these cases is $y_{f,min}^+ = 80$, and the upper limit is $y_{f,max}/\delta = 0.3$, based on the limits of the logarithmic layer defined in equation (1.8). We also conduct case L550-50, which targets 50% of uv across the logarithmic layer at $Re_\tau = 550$, for comparison. The second group of simulations consists of cases O360-30, L550-30, O950-30 and O2000-30. The cases with the ‘O’ prefix are designed to be consistent with case L550-30 in outer units, and

thus have $y_{f,max}/\delta = 0.145$ and $y_{f,max}/\delta = 0.3$. Figure 5.16 shows mean statistics for all the hierarchical-forcing simulations. The statistics for the cases at $Re_\tau \leq 950$ were sampled over at least 30 largest-eddy turnover times, i.e. $t_s \geq 30\delta/u_\tau$. However, due to the high computational cost of the simulations at $Re_\tau = 2000$, which have approximately 500 million grid points, the statistics for cases L2000-30 and O2000-30 have been sampled over a time window of $15\delta/u_\tau$ only. Therefore, the results of these two simulations should be considered tentative, compared to those at the lower Reynolds numbers.

Notwithstanding the tentative nature of the results at $Re_\tau = 2000$, we see from figure 5.16 that the overall effect of the control is similar to the block-forcing simulations. This is not surprising, since we use the same method as before, but target a broader range of wavelengths across a larger range of heights within the logarithmic layer. We observe that the mean profile and r.m.s. velocity fluctuations near the wall are essentially unmodified by the control. However, we observe an increase in the intensity of u'^+ above the buffer layer, which causes a small increase in the peak value near the wall, and persists into the outer region of the flow in some cases. The wall-normal and spanwise r.m.s. velocity fluctuations are also modified slightly by the control in the logarithmic layer, but recover to uncontrolled levels in the outer region. There is a small reduction in $\overline{u'v'}^+$ in the forcing region, but it otherwise appears to be essentially the same as in the uncontrolled flow, at least for the cases at $Re_\tau \leq 950$. As discussed in section 5.1, the reduction in $\overline{u'v'}^+$ in the forcing region results in a local increase in dU^+/dy^+ , and thus we observe an increase in the mean velocity profile within and above the logarithmic layer relative to the uncontrolled case. Based on the results of the simulations at the lower Reynolds numbers, we would expect the profiles of $\overline{u'v'}^+$ for cases at $Re_\tau = 2000$ to also recover to the uncontrolled levels in the outer region, $y^+ \gtrsim 1000$, but we do not observe this in figure 5.16(m). This is almost certainly due to the lack of time to converge for the largest fluctuating scales of the flow in these simulation.

To further investigate the effect of the control, we now consider how the forcing affects the distribution of energy among length scales of the various components of the flow, both within and outside of the forcing region. To illustrate this, the premultiplied spectra for the two cases at $Re_\tau = 950$ are portrayed in figure 5.17. The spectra for the cases at the other Reynolds numbers are qualitatively similar to those at $Re_\tau = 950$ and are not shown here. Figure 5.17(a-d) demonstrates that the dynamics in the buffer layer are modified very little by the control, since the distribution of energy among length scales matches well with the uncontrolled case, although there are some noticeable differences for case L950-30, e.g. energy in long streamwise and spanwise length scales of w^2 (panel c). This is consistent with the collapse of the mean statistics near the wall to the uncontrolled reference cases, which are discussed above and shown in figure 5.16. We see that even though the minimum forcing height is $y_{f,min}^+ = 136$ for case O950-30, the distribution of energy among length scales is still different to the uncontrolled flow at $y^+ = 80$ (figure 5.17e-h), suggesting that the effect of the control persists for some depth outside of the forcing region. Since the minimum forcing height for

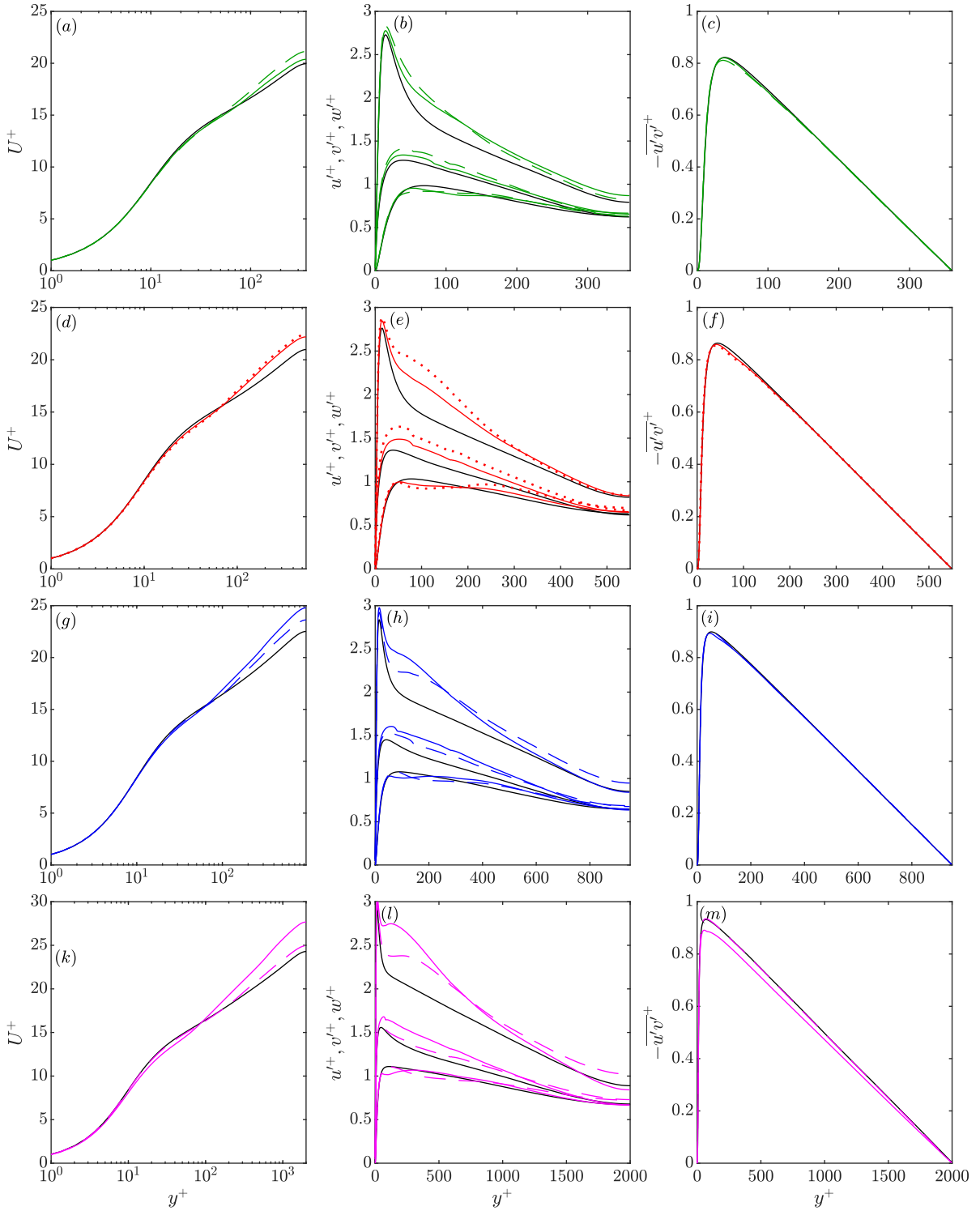


Figure 5.16 Mean statistics for hierarchical-forcing simulations (coloured lines), compared with those of the uncontrolled reference case at the same Reynolds number (black lines). (*a–c*) $Re_\tau = 360$; (*d–f*) $Re_\tau = 550$; (*g–i*) $Re_\tau = 950$; (*j–l*) $Re_\tau = 2000$. See table 5.1 for line styles. Note that the controlled simulations at $Re_\tau = 2000$ are somewhat under-resolved in time ($t_s/T_E \approx 15$), and so their data should be considered tentative. The reference, uncontrolled data for $Re_\tau = 360–950$ is from the present code, while the data at $Re_\tau = 2003$ is taken from Hoyas and Jiménez (2006).

case L950-30 is $y_{f,min}^+ = 80$, this explains why some differences are observed in the spectra at even at $y^+ = 15$. Inside the forcing region, we see that, by targeting v modes, the control successfully removes energy from the central lobe of the uv spectrum, as shown, for instance, in figure 5.17(*j, l*). It appears that a significant part of this removed energy is redistributed to larger streamwise and spanwise wavelengths of both u and uv , including to scales with streamwise wavenumber $k_x = 0$ (see e.g. figure 5.17 *i, l, m, p*). This was also observed in the block-forcing simulations in section 5.1, and will be discussed in more detail in section 5.3. Far enough above the logarithmic layer, e.g. $y/\delta = 0.7$, the distribution of energy among length scales is essentially the same as in the uncontrolled flow (panels *q-t*), which indicates that the dynamics of turbulence are essentially unmodified in the outer region of the flow.

As discussed in section 5.1 and illustrated in figure 5.6, the shape of the mean velocity profile, i.e. the viscous stress dU^+/dy^+ , is influenced directly by the Reynolds shear stress, $\overline{u'v'^+}$, since the two must sum to the linear total stress curve (4.1) at each height. Therefore, if the control generates a local deficit in $\overline{u'v'^+}$ compared to the uncontrolled case, there will be a relative increase in the viscous stress at that height, and the mean velocity profile will increase more quickly with y^+ . Once $\overline{u'v'^+}$ returns to uncontrolled levels, dU^+/dy^+ will thus also return to uncontrolled levels, and the mean velocity profile will be parallel to the uncontrolled one. From the mean statistics in figure 5.16, it appears that this is also the case in the hierarchical-forcing simulations, and the controlled mean velocity profiles eventually become essentially parallel to the uncontrolled ones, far enough above the forcing region. To verify this, figure 5.18 portrays the difference between the mean profiles of the controlled and uncontrolled flows as a function of y^+ , i.e. $\Delta U^+(y^+) = U_c^+(y^+) - U_0^+(y^+)$, as well as this difference normalised by the centreline velocity of the uncontrolled flow as a function of y/δ , i.e. $\Delta U^+(y/\delta)/U_{\delta_0}^+$. We also show in figure 5.19 the difference between the Reynolds shear stress of the controlled and uncontrolled flows, $\Delta \overline{u'v'^+} = \overline{u'v'_c^+} - \overline{u'v'_0^+}$, as a function of both y^+ and y/δ . From figure 5.18(*a, c*), we see that there is a small deficit in mean velocity for $y^+ \lesssim 100$, which suggests that the buffer-layer dynamics are modified slightly, even though we do not control this region directly. This is consistent with the increase in $\overline{u'v'^+}$ in the buffer layer for the controlled cases, denoted by the negative regions of $\Delta \overline{u'v'^+}$ in figure 5.19 and the changes observed in the spectra in figure 5.17. It is interesting to note that the minimum value of $\Delta \overline{u'v'^+}$, i.e. the largest increase in $\overline{u'v'^+}$, occurs at $y^+ \approx 10$, which is the approximate height of the quasi-streamwise vortices of the buffer-layer cycle. These vortices dominate the dynamics of the flow near the wall and organise the Reynolds shear stress there, as discussed in section 1.1, and so it is not surprising that any increase in turbulence intensity would occur at that height. Above the buffer layer, ΔU^+ increases, particularly in the forcing region, as expected, and then becomes essentially constant in the outer region, $y/\delta \gtrsim 0.5$. This is reflected in figure 5.19, where we see a deficit of $\overline{u'v'^+}$ in the forcing region, i.e. $\Delta \overline{u'v'^+} > 0$, and then $\Delta \overline{u'v'^+}$ eventually falls to zero for $y/\delta \gtrsim 0.5$, except for the cases at $Re_\tau = 2000$, which will be discussed further below. We also observed the same effect in the block-forcing simulations in section 5.1, where we argued that this suggest

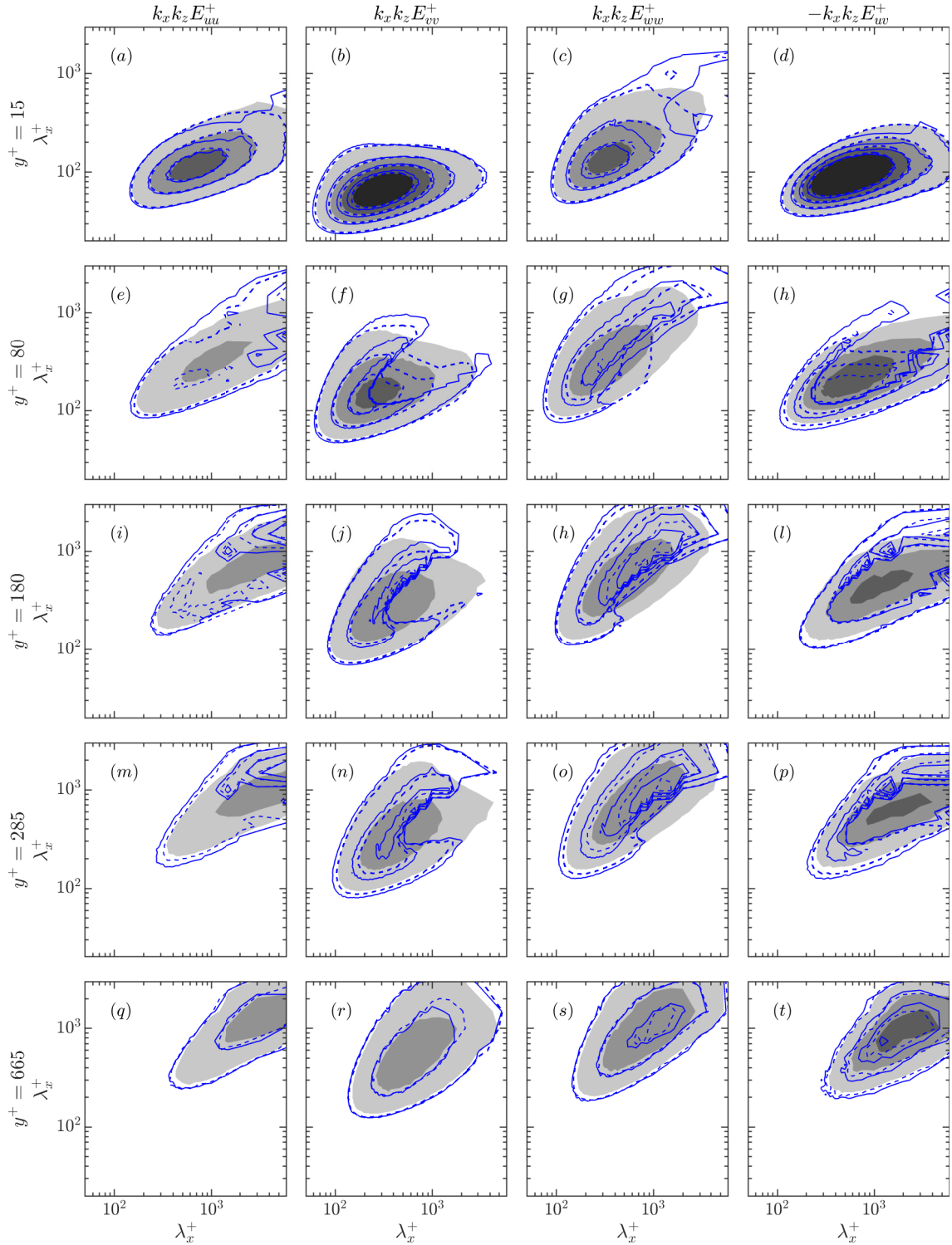


Figure 5.17 Premultiplied two-dimensional spectral densities of u^2 , v^2 , w^2 and uv normalised by u_τ^2 for cases L950-30 (solid blue lines) and O950-30 (dashed blue lines), compared to the uncontrolled case (filled contours). (a–d) in the buffer layer, $y^+ = 15$; (e–h) at the bottom limit of logarithmic layer, $y^+ = 80$; (i–l) in the middle of the logarithmic layer, $y^+ = 180$; (m–p) at the top limit of the logarithmic layer, $y^+ = 0.3Re_\tau = 285$; (q–t) in the outer layer, $y^+ = 0.7Re_\tau = 665$. (a, e, i, m, q) $k_x k_z E_{uu}^+$; (b, f, j, n, r) $k_x k_z E_{vv}^+$; (c, g, h, o, s) $k_x k_z E_{ww}^+$; (d, l, p, t) $-k_x k_z E_{uv}^+$.

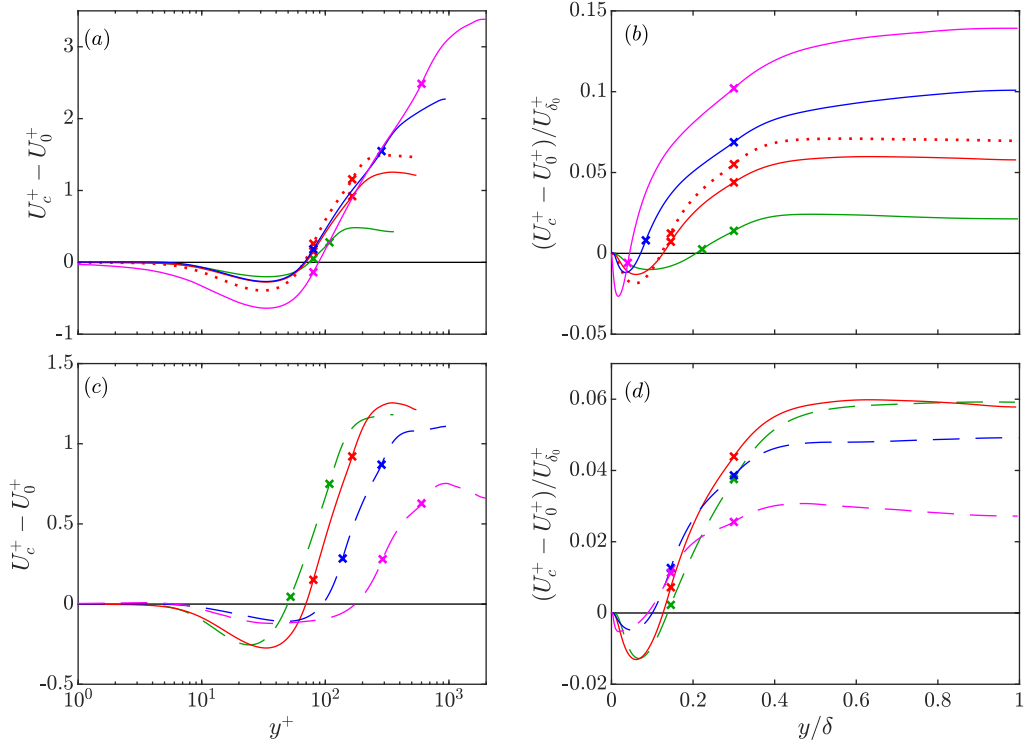


Figure 5.18 Difference between the mean velocity profiles of the controlled and uncontrolled flows as a function of y^+ (a, c), i.e. $\Delta U^+(y^+) = U_c^+(y^+) - U_0^+(y^+)$, and the same difference normalised by the channel centreline velocity of the uncontrolled case as a function of y/δ (b, d), i.e. $\Delta U^+(y/\delta)/U_{\delta_0}^+$. (a, b) cases L360-30, L550-30, L550-50, L950-30 and L2000-30, (c, d) cases O360-30, L550-30, O950-30 and O2000-30. See table 5.1 for line styles. The crosses denote the lower and upper limits of the forcing region in each case, i.e. $y_{f,min}$ and $y_{f,max}$, respectively. Note that the controlled simulations at $Re_\tau = 2000$ are somewhat under-resolved in time ($t_s/T_E \approx 15$), and so their data should be considered tentative.

the dynamics of turbulence in the outer region remained the same as in the uncontrolled case, the only difference being the additional mean velocity ΔU^+ , and thus the flow recovers outer-layer similarity (Townsend, 1976). This is also supported by the spectra for cases L950-30 and O950-30 at $y/\delta = 0.7$ shown in figure 5.17(q-t), which exhibit the same distribution of energy among length scales as the uncontrolled reference case, indicated that the dynamics of turbulence are essentially unmodified in the outer region.

In section 5.1, we demonstrated that because ΔU^+ was small, $\mathcal{O}(0.5)$, very long time-averaging windows were required to measure it accurately. We argued that the situation would improve for larger ΔU^+ , because the natural fluctuations in the mean velocity profile in the outer region would be less significant relative to the measured value. Therefore, the curves of ΔU^+ presented in figure 5.18 will be relatively robust to statistical uncertainty, because ΔU^+ is typically of order 1 or larger. However, we see in figure 5.19 that the magnitude of $\overline{\Delta u'v'^+}$ is much smaller, $\mathcal{O}(0.01)$, and thus will be very sensitive to statistical uncertainty. In light of this, $\overline{\Delta u'v'^+}$ should be viewed as a more qualitative measure of the change in the flow. The effect of statistical uncertainty on $\overline{\Delta u'v'^+}$ can be seen for the simulations at $Re_\tau = 2000$, which,

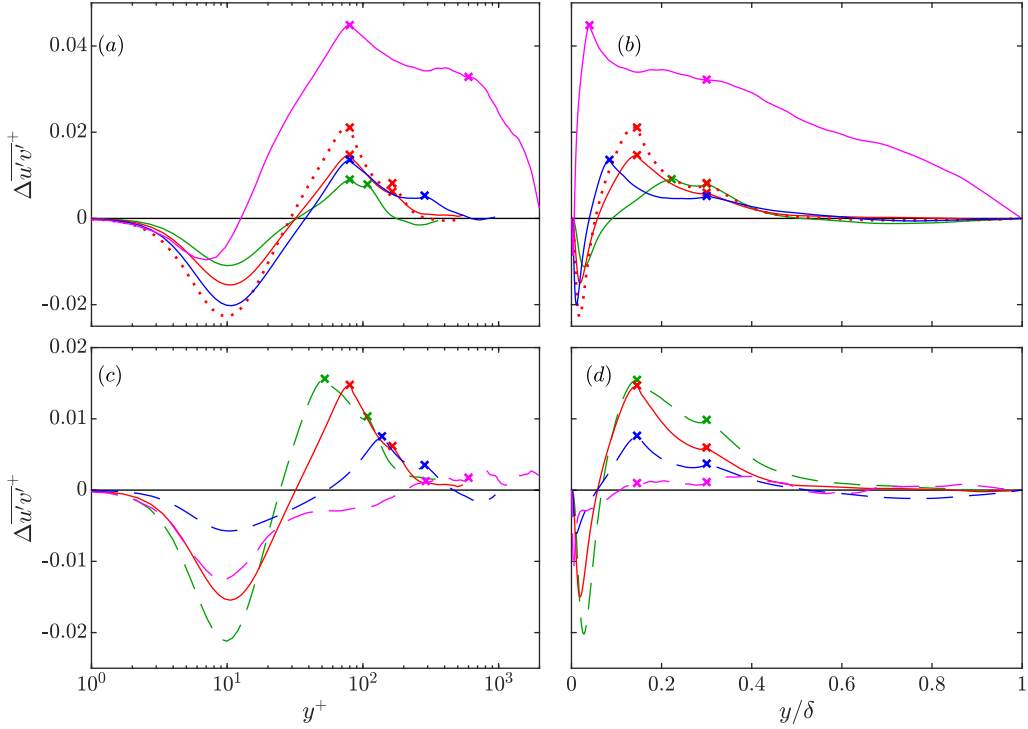


Figure 5.19 Difference between the Reynolds shear stress of the controlled and uncontrolled flows, $\Delta \overline{u'v'}^+ = \overline{u'v'}_c^+ - \overline{u'v'}_0^+$ as a function of y^+ (a, c), and y/δ (b, d). (a, b) cases L360-30, L550-30, L550-50, L950-30 and L2000-30, (c, d) cases O360-30, L550-30, O950-30 and O2000-30. See table 5.1 for line styles. The crosses denote the lower and upper limits of the forcing region in each case, i.e. $y_{f,min}$ and $y_{f,max}$, respectively. Note that the controlled simulations at $Re_\tau = 2000$ are somewhat under-resolved in time ($t_s/T_E \approx 15$), and so their data should be considered tentative.

as mentioned above, are somewhat under-resolved in time. This lack of temporal convergence is particularly clear for case L2000-30 in the outer region, $y/\delta \gtrsim 0.5$, where we would expect $\Delta \overline{u'v'}^+$ to be approximately zero (figure 5.19b), since ΔU^+ is essentially constant in that region (figure 5.18b). Near the wall, $y/\delta \lesssim 0.1$, we have more statistical samples of the eddies in the flow, since the characteristic turnover time of the eddies at a height y is $\mathcal{O}(y/u_\tau)$, and thus the Reynolds shear stress in this region exhibits better temporal convergence.

5.2.1 Effect of Reynolds number and comparison to theoretical predictions

We mentioned above that the hierarchical forcing simulations can be split into two groups. The first group consists of cases L360-30, L550-30, L950-30 and L2000-30, which target 30% of $\overline{u'v'}_0^+$ across the whole logarithmic layer. The forcing region in these cases grows in thickness, in both inner and outer units, as Re_τ increases, i.e. $y_{f,min}^+ = 80$ and $y_{f,max}/\delta = 0.3$. In the second group of simulations, we instead target 30% of $\overline{u'v'}_0^+$ across a fixed region of the flow in outer units, $y_{f,min}/\delta = 0.145$ and $y_{f,max}/\delta = 0.3$. These are cases O360-30, L550-30, O950-30 and O2000-30. We now wish to investigate how the effect of the control varies with Reynolds

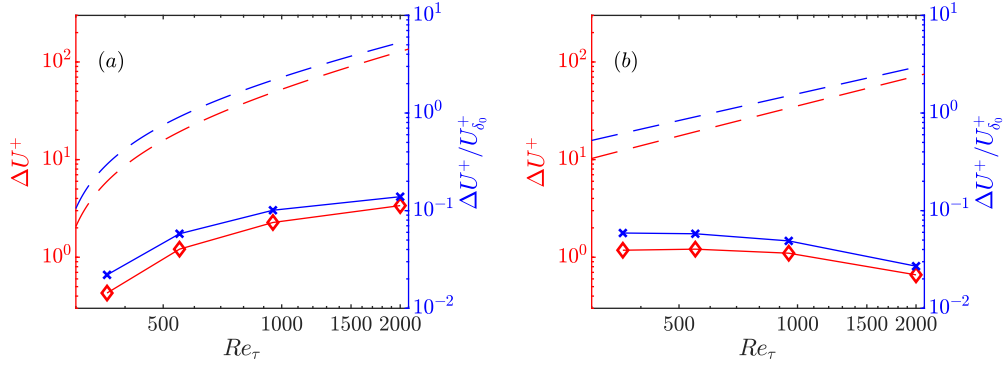


Figure 5.20 $\Delta U^+(y^+ = Re_\tau)$ (red) and $\Delta U^+(y^+ = Re_\tau)/U_{\delta_0}^+$ (blue) as a function of Re_τ from DNSs (solid lines with symbols) compared with theoretical predictions from chapter 4 using equations (4.8) and (4.17), with $\phi = 0.3$ (dashed lines). (a) targeting 30% of uv across the whole logarithmic layer, i.e. cases L360-30, L550-30, L950-30 and L2000-30, and (b) controlling a fixed region of the flow in outer units, $0.145 \leq y/\delta \leq 0.3$, i.e. cases O360-30, L550-30, O950-30 and O2000-30. Note that the controlled simulations at $Re_\tau = 2000$ are somewhat under-resolved in time ($t_s/T_E \approx 15$), and so their data should be considered tentative.

number within these two groups of simulations. In figure 5.20 we show the variation with Re_τ of ΔU^+ and $\Delta U^+/U_{\delta_0}^+$ measured at the channel centre. The first group of simulations is shown in panel (a), while the second is shown in panel (b). For comparison, we also include theoretical curves for the idealised logarithmic-layer control strategy derived in chapter 4. Using equations (4.8) and (4.17), we assume that the control removes 30% of the uncontrolled Reynolds shear stress, i.e. $\phi = 0.3$, and match the theoretical control region to the actual forcing region in our DNSs. These theoretical curves serve as an upper bound for the effect of the control on the flow. That is, they represent the predicted effect of the control if its only effect were to remove the target length scales, while leaving the rest of the flow untouched.

In figure 5.20(a), we see that when the control acts on the whole depth of the logarithmic layer, both ΔU^+ and $\Delta U^+/U_{\delta_0}^+$ increase with Re_τ , which is the trend expected from the theory. However, the values of ΔU^+ and $\Delta U^+/U_{\delta_0}^+$ from the simulations are an order of magnitude smaller than the theoretical ones, and the curves from the simulations appear to diverge from the theoretical ones as Re_τ increases. In the simulations where a fixed region of the flow in outer units is controlled (figure 5.20b), ΔU^+ and $\Delta U^+/U_{\delta_0}^+$ tend to decrease with Re_τ . This is in contrast to the quasi-linear increase of both ΔU^+ and $\Delta U^+/U_{\delta_0}^+$ with Re_τ predicted by the theory. The values of ΔU^+ and $\Delta U^+/U_{\delta_0}^+$ are again at least an order of magnitude smaller than the theoretical ones. These differences likely arise because even though the target wavelengths contribute to 30% of the uncontrolled Reynolds shear stress $\overline{u'v'}_0^+$ in the forcing region, and those length scales of uv are indeed removed from the flow (see e.g. figure 5.17l), the net effect of the control is to remove only a very small proportion of $\overline{u'v'}_0^+$ in the resulting flow. This can be appreciated from the profiles of $\overline{u'v'}^+$ in figure 5.16(c, f, i, m) and $\Delta \overline{u'v'}^+$ in figure 5.19, and

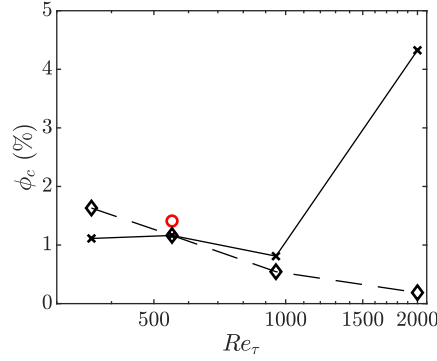


Figure 5.21 The average, relative proportion of Reynolds shear stress removed in the forcing region compared to the uncontrolled flow, ϕ_c , computed from the curves of $\Delta \overline{u'v'^+}$ in figure 5.19 using equation (5.1). Solid line with crosses, cases L360-30, L550-30, L950-30 and L2000-30, in which 30% of uv is targeted across the whole logarithmic layer; dashed line with diamonds, cases O360-30, L550-30, O950-30 and O2000-30, in which 30% of uv is targeted across a fixed region of the flow in outer units, $0.145 \leq y/\delta \leq 0.3$; red circle, case L550-50, in which 50% of uv is targeted across the whole logarithmic layer. Note that the controlled simulations at $Re_\tau = 2000$ are somewhat under-resolved in time ($t_s/T_E \approx 15$), and so their data should be considered tentative.

occurs because the energy originally contained in the target length scales is redistributed to larger streamwise as spanwise wavelengths, as mentioned above.

As discussed in chapter 4, for large enough Re_τ , controlling the whole logarithmic layer is essentially equivalent to controlling a fixed region of the flow in outer units, $0 \lesssim y/\delta \lesssim 0.3$. Therefore, it is surprising that the results of the simulations that control the whole logarithmic layer (figure 5.20a) follow the same general trend as the theory (ΔU^+ increasing with Re_τ), but the simulations that control a fixed region in outer units do not (figure 5.20b). A possible explanation for this is that, with hindsight, the simulations that target a fixed region of the flow in outer units, cases O360-30, L550-30, O950-30 and O2000-30, will likely have a different effect on the flow in the buffer layer, since the minimum height of the control in wall units increases with Re_τ from only $y_{f,min}^+ = 52$ for the lowest Reynolds number (see table 5.2). Therefore, for the lower Reynolds numbers, additional energy would be removed from the buffer layer compared to the simulations at larger Reynolds numbers, and hence the value of ΔU^+ would be artificially larger.

In order to quantify this difference between the predicted and actual effect of the control, figure 5.21 portrays the average, relative decrease in total Reynolds stress removed in the forcing region compared to the uncontrolled flow, which we denote by ϕ_c . This is computed from ratio of the curves of $\Delta \overline{u'v'^+}(y^+)$ in figure 5.19 and their uncontrolled counterparts, $\overline{u'v'_0^+}(y^+)$, at the same Re_τ . That is,

$$\phi_c = \frac{1}{\Delta y_f^+} \int_{y_{f,min}^+}^{y_{f,max}^+} - \frac{\Delta \overline{u'v'^+}(y^+)}{\overline{u'v'_0^+}(y^+)} dy^+, \quad (5.1)$$

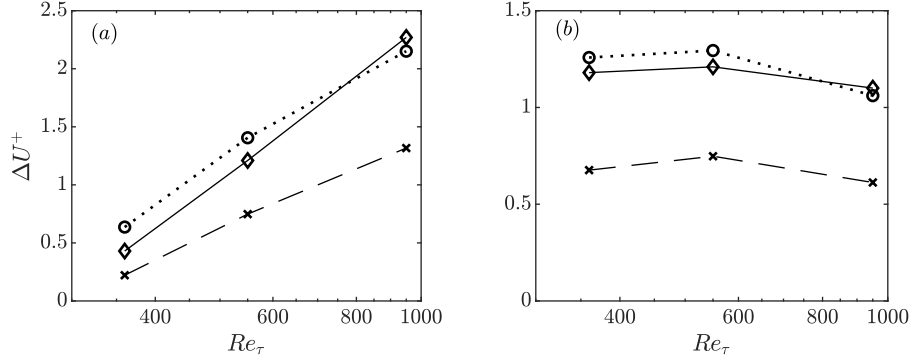


Figure 5.22 $\Delta U^+(y^+ = Re_\tau)$ from hierarchical-forcing simulations (solid lines with diamonds) compared to theoretical predictions using equations (4.8) and (4.17). Dashed lines with crosses, theoretical predictions with $\phi = \phi_c$, calculated using equation (5.1) and shown in figure 5.21. Dotted lines with circles, theoretical predictions with $\phi = \phi'_c$, calculated using equation (5.2) and shown in figure 5.23. (a) cases L360-30, L550-30 and L950-30, in which the forcing region is defined by $y_{f,min}^+ = 80$ and $y_{f,max}^+/\delta = 0.3$. (b) cases O360-30, L550-30 and O950-30, in which the forcing region is defined by $y_{f,min}^+/\delta = 0.145$ and $y_{f,max}^+/\delta = 0.3$.

where $\Delta y_f^+ = y_{f,max}^+ - y_{f,min}^+$ is the thickness of the forcing region and $0 \leq y^+ \leq Re_\tau$. Due to the lack of temporal convergence and the sensitivity of $\overline{\Delta u'v'^+}$ to statistical uncertainty discussed above, the values of ϕ_c for $Re_\tau = 2000$ may not be representative of the true value. However, we observe two trends from the figure for the cases at $Re_\tau \leq 950$. We see that when the whole logarithmic layer is controlled, $\phi_c \approx 1\%$ and remains relatively constant for $Re_\tau \leq 950$. As discussed in chapter 4, the proportion of Reynolds shear stress targeted by the control acts simply as a multiplicative factor in the theoretical expression for ΔU^+ (4.17). This is supported by the curves of ΔU^+ and $\Delta U^+/U_{\delta_0}^+$ for the simulations in figure 5.20(a), which approximately follow the same trends as the theoretical predictions, only an order of magnitude smaller. On the other hand, when a fixed region of the flow in outer units is controlled, figure 5.21 shows that the proportion of Reynolds shear stress removed is still of order 1%, at least for $Re_\tau \leq 950$, but tends to decrease with increasing Re_τ . This is consistent with the curves for the simulations in figure 5.20(b), which do not follow the same trend as the theoretical ones, and both ΔU^+ and $\Delta U^+/U_{\delta_0}^+$ decrease with Re_τ . Note that in all the hierarchical-forcing simulations, the actual proportion of Reynolds shear stress removed is an order of magnitude smaller than the proportion targeted by the control. This was also observed in the block forcing simulations presented in section 5.1, and suggests that the flow in the logarithmic layer is very robust to this kind of control. We will discuss this idea further in section 5.3.

We now wish to determine if it is possible to improve the theoretical predictions by taking into account the actual proportion of the Reynolds shear stress removed in the simulations, ϕ_c , which is defined by (5.1). In figure 5.22, we compare again the measured values of ΔU^+ from the simulations at $Re_\tau \leq 950$ with the theoretical predictions, but now we set $\phi = \phi_c$. These curves are denoted by the solid and dashed lines, respectively. Note that ϕ is different in each

case, because ϕ_c varies with Re_τ , as shown in figure 5.21. We see that the theoretical predictions in figure 5.22 agree relatively well with the results of the simulations, but consistently under-predict the values of ΔU^+ . This is because the effect of the control in the hierarchical-control simulations is not confined to the forcing region, and the deficit of Reynolds shear stress, i.e. $\Delta \overline{u'v'}^+ > 0$, persists for some distance outside of the logarithmic layer before falling to zero, as shown in figure 5.19. In this sense, the forcing region spans a thicker wall-normal region of the flow in the simulations than anticipated by the theory. In order to refine further the theoretical prediction, we account for the effect of this ‘extended’ forcing region, as follows. From figure 5.19, we approximate the extended forcing region as the wall-normal distance over which $\Delta \overline{u'v'}^+ \gtrsim 0$ for the simulations of interest. When the nominal forcing region spans the whole logarithmic layer, we see that $\Delta \overline{u'v'}^+ \gtrsim 0$ for $y^+ \gtrsim 40$ and $y/\delta \lesssim 0.5$ (figure 5.19a, b). On the other hand, when the nominal forcing region is fixed in outer units, $\Delta \overline{u'v'}^+ \gtrsim 0$ for $0.1 \lesssim y/\delta \lesssim 0.5$ (figure 5.19d). We refer to the limits of the extended forcing region as $y'_{f,min}$ and $y'_{f,max}$. We then compute the average, relative decrease in Reynolds shear stress in the region $y'_{min} \leq y \leq y'_{max}$, which we refer to as ϕ'_c , using an expression similar to (5.1),

$$\phi'_c = \frac{1}{\Delta y_f'^+} \int_{y'_{f,min}}^{y'_{f,max}} -\frac{\Delta \overline{u'v'}^+(y^+)}{\overline{u'v'}_0^+(y^+)} dy^+, \quad (5.2)$$

where $\Delta y_f'^+ = y'_{f,max} - y'_{f,min}$. The values of ϕ'_c for the cases of interest are shown in figure 5.23, for reference. We then recompute the theoretical value of ΔU^+ using equations (4.8) and (4.17), assuming that the proportion of Reynolds shear stress removed is $\phi = \phi'_c$ within the extended forcing region. These values are denoted by the dotted lines in figure 5.22, and agree very well with the values measured from the simulations. This demonstrates that it is possible to account for the effect of the hierarchical-forcing simulations using the theoretical predictions of the idealised control strategy derived in chapter 4, albeit only a posteriori, by calculating the actual proportion of the Reynolds shear stress removed in the extended forcing region. In addition, since the idealised control strategy assumes that the flow outside the control region is left unaltered, figure 5.22 further suggests that the flow is left essentially unmodified far enough outside the forcing region in the hierarchical-forcing simulations, as discussed above.

5.3 Robustness of the logarithmic layer to the control

A key feature of both the block-forcing and hierarchical-forcing simulations discussed in this chapter is that the actual proportion of the total Reynolds shear stress removed in the simulations is typically an order of magnitude smaller than the proportion contained in the target length scales in the uncontrolled flow (see figures 5.13 and 5.21). In the hierarchical forcing simulations, the control is particularly intrusive, and targets at least 30% of the total Reynolds shear stress $\overline{u'v'}_0^+$ in the uncontrolled flow. Even in the most extreme case, when 50% of $\overline{u'v'}_0^+$ is targeted in

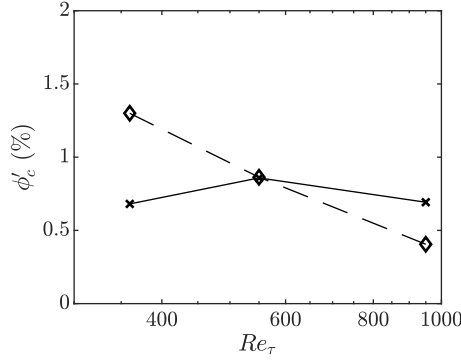


Figure 5.23 Alternative calculation of the average, relative proportion of Reynolds shear stress removed by the control compared to the uncontrolled flow, ϕ'_c , computed from the curves of $\Delta\overline{u'v'^+}$ in figure 5.19 using equation (5.2). In contrast to ϕ_c in figure 5.21, ϕ'_c is evaluated in the region where $\Delta\overline{u'v'^+} \gtrsim 0$, rather than only within the forcing region. Solid line with crosses, cases L360-30, L550-30 and L950-30, in which 30% of uv is targeted across the whole logarithmic layer; dashed line with diamonds, cases O360-30, L550-30 and O950-30, in which 30% of uv is targeted across a fixed region of the flow in outer units, $0.145 \leq y/\delta \leq 0.3$.

the logarithmic layer, i.e. case L550-50, figure 5.21 shows that the relative decrease in Reynolds shear stress, ϕ_c , is only approximately 1.5%. This suggests that the flow in the logarithmic layer is very robust, even to this kind of targeted and intrusive control strategy. We noted above that a significant part of the energy originally contained in the target length scales appears to be redistributed to larger streamwise and spanwise wavelengths of uv within the forcing region, including to scales with streamwise wavenumber $k_x = 0$ (see figure 5.17). This would account, at least to some extent, for this difference between the proportion of $\overline{u'v'_0^+}$ targeted and the total proportion removed.

We now investigate this further and aim to determine to what extent energy is redistributed to larger streamwise and spanwise wavelengths. Figure 5.24 portrays the premultiplied spectrum of uv in the centre of the logarithmic layer for the cases in which 30% of $\overline{u'v'_0^+}$ is targeted across the whole logarithmic layer, i.e. cases L360-30, L550-30, L950-30 and L2000-30. The figure shows that the distribution of energy among the smaller length scales of uv in the controlled cases is similar to that of the uncontrolled flow, except for the target length scales, which contain no energy because they are set to zero in our simulations. On the other hand, for the larger lengths scales, we observe that more energy is now concentrated in streamwise and spanwise scales of the order of the channel half height or larger, i.e. $\lambda_x/\delta \gtrsim 1$ and $\lambda_z/\delta \gtrsim 1$. These regions are denoted by the black rectangles in each panel. Note that figure 5.24 portrays the premultiplied spectrum for length scales with $k_x, k_z \geq 1$, in a discrete sense, and so the wavelengths of the largest length scales in the figure are equal to the streamwise and spanwise extent of the computational domain, respectively, i.e. $\lambda_x = L_x$ and $\lambda_z = L_z$. The premultiplied spectrum of uv is defined as $\Phi_{uv}(k_x, k_z, y) = -k_x k_z E_{uv}(k_x, k_z, y)$, where $E_{uv}(k_x, k_z, y)$ denotes the contribution to $\overline{u'v'}$ of mode (k_x, k_z) at a given height (see e.g. Jiménez, 2018). By definition,

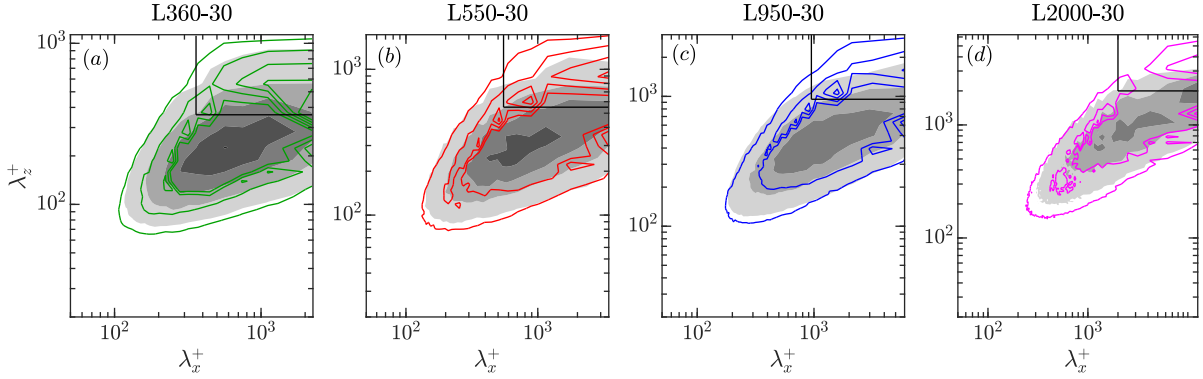


Figure 5.24 Premultiplied two-dimensional spectral density of uv normalised by u_τ^2 , i.e. $-k_x k_z E_{uv}^+$, for cases L360-30 (green lines), L550-30 (red lines), L950-30 (blue lines) and L2000-30 (magenta lines), compared to the uncontrolled case at the same Re_τ (filled contours) in the centre of the logarithmic layer, $y^+ = (80 + 0.3Re_\tau)/2$. The black rectangles enclose wavelengths that satisfy $\lambda_x/\delta \geq 1$ and $\lambda_z/\delta \geq 1$, used to compute ϕ_l (5.3), which is given in figure 5.25. Note that the controlled simulations at $Re_\tau = 2000$ are somewhat under-resolved in time ($t_s/T_E \approx 15$), and so their data should be considered tentative.

$\Phi_{uv} = 0$ when $k_x = 0$ or $k_z = 0$, but in general E_{uv} can be non-zero for those modes. This can be appreciated from figure 5.24, where we see that the spectrum of Φ_{uv} is not ‘closed’ with respect to the largest streamwise wavelengths in both the controlled and uncontrolled flows, indicating that some energy is contained in scales with $k_x = 0$, i.e. $\lambda_x = L_x/k_x = \infty$. Indeed, any energy that would be contained in scales larger than $\lambda_x = L_x$ in our simulations is stored instead in length scales with $k_x = 0$.

We now wish to quantify the amount of energy redistributed to the largest length scales in the controlled flow in the centre of the logarithmic region. The length scales of interest have $\lambda_x/\delta \gtrsim 1$ and $\lambda_z/\delta \gtrsim 1$, and are denoted by the black rectangles in figure 5.24. We compute the relative difference between the energy contained in those scales in the controlled and uncontrolled flows, normalised by the total uncontrolled Reynolds shear stress at that height $\overline{u'v'_0}^+$. This is denoted by ϕ_l and may be expressed as the integral

$$\phi_l = \iint_{k_{x,l}, k_{z,l}} \frac{\Delta E_{uv}^+(k_x, k_z)}{\overline{u'v'_0}^+} dk_x dk_z, \quad (5.3)$$

where $\Delta E_{uv}^+(k_x, k_z)$ is the difference between the energy contained in a given mode in the controlled and uncontrolled flows, and $k_{x,l}$ and $k_{z,l}$ are the wavenumbers of the largest length scales of interest. In (5.3), we integrate over $k_{x,l}, k_{z,l} \leq L_x/\delta$, i.e. $\lambda_x/\delta, \lambda_z/\delta \geq 1$, including the modes with $k_x, k_z = 0$, although we omit the wavenumbers corresponding to the target length scales, because $E_{uv} = 0$ for those modes in the controlled flow. Figure 5.25 portrays the value of ϕ_l normalised by the proportion of $\overline{u'v'_0}^+$ targeted by the control, i.e. ϕ_l/ϕ , for the four hierarchical-forcing simulations considered here. The figure demonstrates that the

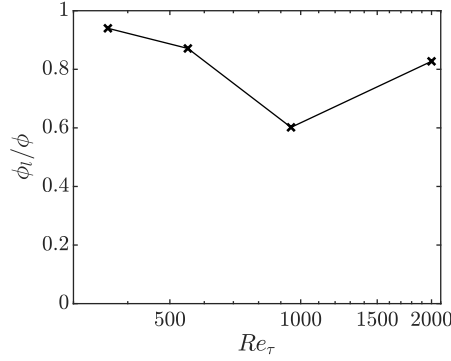


Figure 5.25 Relative proportion, ϕ_l (5.3), of $\overline{u'v'^+}$ contained in the length scales with wavelengths $\lambda_x/\delta \geq 1$ and $\lambda_z/\delta \geq 1$, denoted by the black rectangles in figure 5.24, normalised the proportion of $\overline{u'v'^+}$ targeted, $\phi = 30\%$, for cases L360-30, L550-20, L950-30 and L2000-30. Note that the controlled simulations at $Re_\tau = 2000$ are somewhat under-resolved in time ($t_s/T_E \approx 15$), and so their data should be considered tentative.

majority of the energy originally contained in the target length scales is redistributed to the largest length scales in the flow, as expected, consistent with the idea that the flow in the logarithmic region is robust to this kind of control. From a physical viewpoint, it is possible that energy is redistributed to these large scales because they are the active scales of large eddies that reach well into the outer region of the flow, and any energy that is redistributed to the very small scales would quickly be removed through viscous dissipation. As mentioned above, some of this energy is redistributed to streamwise length scales with infinite wavelength, i.e. $k_x = 0$, in our simulations. Therefore, it is difficult to build a clear picture of the specific large scales to which energy is redistributed from the target modes, which, in hindsight, is a limitation of the size of the computational domain in our simulations. However, as a crude first approximation, the spectra in figure 5.24 suggest that the spanwise length scale of the dominant $k_x = 0$ modes is approximately $\lambda_z/\delta \approx 2$. If the computational domain were longer, we would resolve larger streamwise wavelengths, and some of the energy currently contained in length scales with $k_x = 0$ would be captured by those modes, which would allow for a more rigorous analysis of the dynamics of the large scales in these cases.

To further demonstrate the effect of the control in the forcing region, figures 5.26 and 5.27 show instantaneous snapshots of u^+ , v^+ and w^+ for cases L550-30 and L950-30 in the centre of the logarithmic layer, alongside snapshots from their reference uncontrolled flows at the same height. We observed above in sections 5.1 and 5.2 that in the forcing region energy is redistributed primarily to larger streamwise and spanwise length scales of u , and hence we observe the same change in the distribution of energy in uv (see e.g. figures 5.5 and 5.17). The snapshots in figures 5.26 and 5.27 further support this. We see that the streamwise fluctuations in the controlled flows (panels *b*) appear more coherent in the streamwise direction and exhibit a clearer separation between regions of positive and negative u^+ in the spanwise direction,

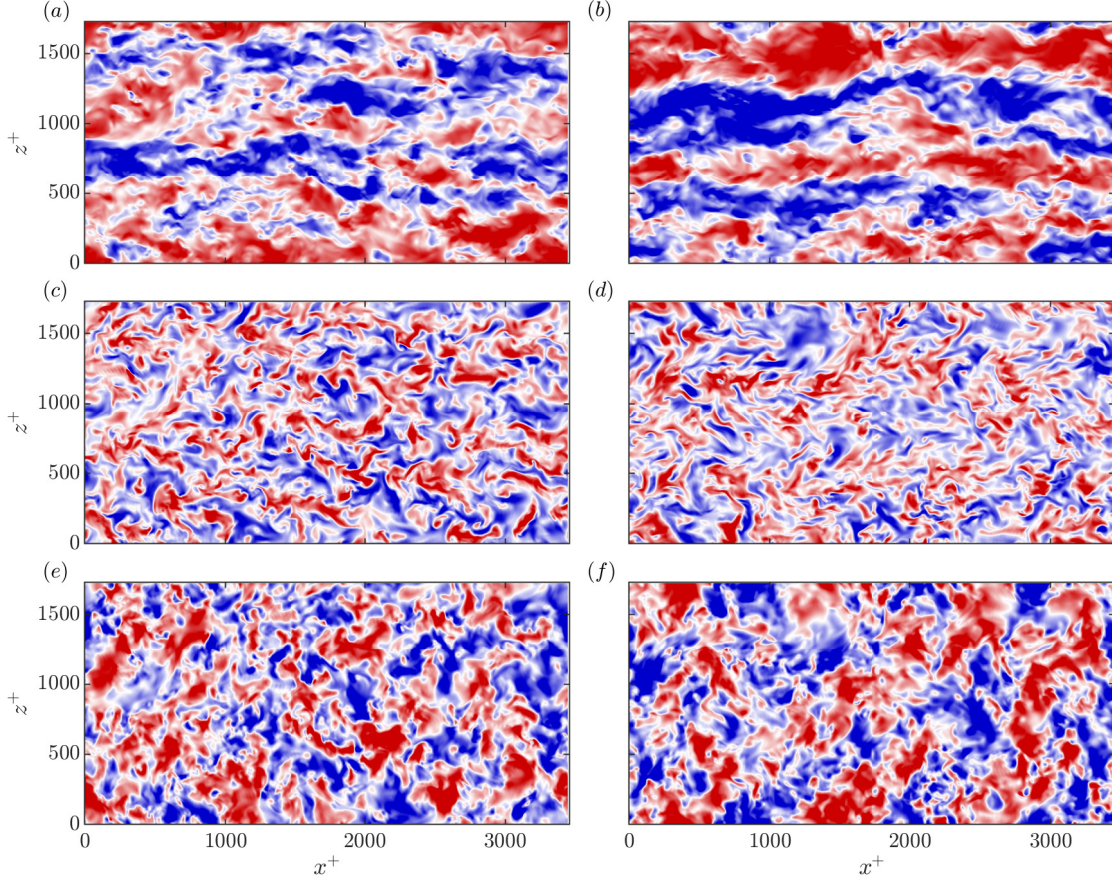


Figure 5.26 Instantaneous snapshots of (a,b) u^+ , (c,d) v^+ and (e,f) w^+ for (a,c,e) the uncontrolled flow at $Re_\tau = 550$ and (b,d,f) the controlled case L550-30 in the centre of the logarithmic layer, $y^+ = (80 + 0.3Re_\tau)/2$. This height corresponds to the plane at which the spectra are plotted in figure 5.24(b). Blue to red corresponds to $u^+ = [-3, 3]$, $v^+ = [-2, 2]$ and $w^+ = [-2, 2]$.

compared to the uncontrolled flows (panels a). This would suggest that energy is now contained in larger streamwise and spanwise wavelengths of u^+ , and is particularly clear for case L950-30 in figure 5.27(b). The absence of the removed v^+ scales in the controlled flows can also be appreciated from figures 5.26(d) and 5.27(d). Finally, the coherent regions of w^+ appear to be slightly longer in x and wider in z in the controlled flows (figures 5.26f and 5.27f), which would be consistent with the change in the spectrum of w^2 in the forcing region in figure 5.17(h).

A possible explanation for the observed redistribution is that the control results in an impermeable boundary for the target scales. Therefore, by continuity, it follows that the wall-normal energy originally contained in the target scales would be instantaneously redistributed to the streamwise and spanwise components at that height. As alluded to above, the reason

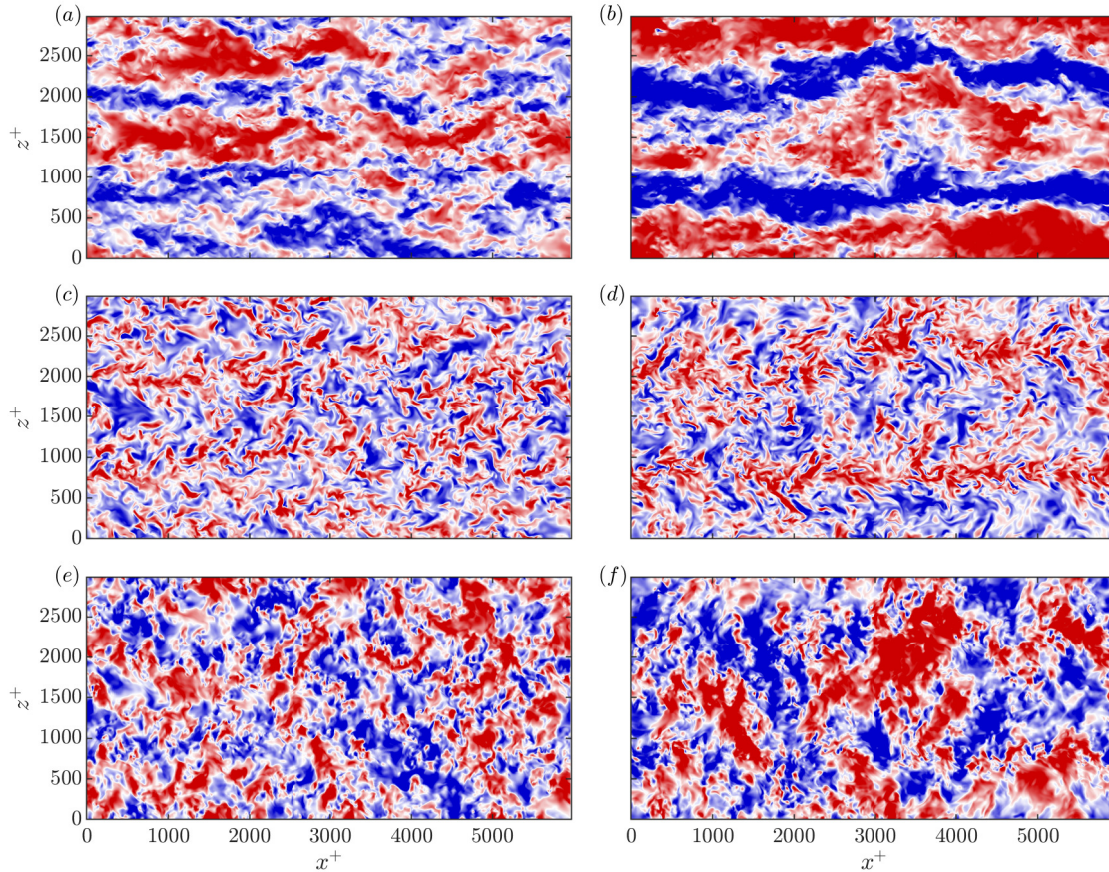


Figure 5.27 Instantaneous snapshots of (a,b) u^+ , (c,d) v^+ and (e,f) w^+ for (a,c,e) the uncontrolled flow at $Re_\tau = 950$ and (b,d,f) the controlled case L950-30 in the centre of the logarithmic layer, $y^+ = (80 + 0.3Re_\tau)/2$. This height corresponds to the plane at which the spectra are plotted in figure 5.24(c). Blue to red corresponds to $u^+ = [-3, 3]$, $v^+ = [-2, 2]$ and $w^+ = [-2, 2]$.

that this energy is transferred to larger scales is likely because they are the active scales of larger eddies that reach into the outer region of the flow, and are thus not inhibited by the impermeable boundary enforced on the target scales. This behaviour could, however, be a result of the choice to remove energy from only v directly. Had the same modes of u been targeted, for instance, we would remove energy from the same uv scales, by definition, but it is not clear whether this energy would be redistributed in the same way. This warrants further investigation in the future, and could even be extended to removing energy from certain scales of w directly, or even combinations of all three velocity components.

As a final comment on the logarithmic-layer control simulations presented in this chapter, the most promising results came from the hierarchical-forcing simulations in which the whole

logarithmic layer was controlled, i.e. cases L360-30, L550-30, L950-30 and L2000-30. These cases had the largest values of ΔU^+ and $\Delta U^+/U_{\delta_0}^+$, and figure 5.18(a) suggests that both quantities will continue to grow with further increases in Reynolds number beyond $Re_\tau = 2000$. By taking as reference the channel centreline velocity $U_{\delta_0}^+$, which allows for comparison with external flows of interest, we discussed in chapter 4 the connection between $\Delta U^+/U_{\delta_0}^+$ and the drag reduction DR (4.13), as shown in figure 4.4. When 30% of $\overline{u'v'}_0^+$ is targeted across the whole logarithmic layer at $Re_\tau = 2000$, i.e. case L2000-30, our tentative results give $\Delta U^+ \approx 3$ and $\Delta U^+/U_{\delta_0}^+ \approx 0.12$ (see figure 5.18a and table 5.2), which would correspond to $DR \approx 20\%$. If $\Delta U^+/U_{\delta_0}^+$ indeed continues to grow with Re_τ , as figure 5.18(a) suggests, then so too would DR , implying that the performance of this control strategy improves with Reynolds number. This general behaviour was predicted by the theoretical, idealised control strategy presented in chapter 4, although the theoretical values of drag reduction would be much larger than in our simulations (see section 5.2). This is in contrast to the drag reduction generated by buffer-layer control strategies, which typically degrades with Reynolds number, because ΔU^+ remains essentially constant, as discussed in chapter 1. It is interesting to note, however, that $\Delta U^+ \approx 3$ can be achieved by small-scale surface texture, such as anisotropic permeable substrates (see e.g. Gómez-de-Segura and García-Mayoral, 2019), which provides some context for the values of ΔU^+ in our logarithmic-layer control simulations. Given that the control in our simulations is very intrusive and targeted, and could not be implemented in reality, this suggests that even though controlling the logarithmic layer has significant potential in terms of drag reduction, the actual performance may be limited and not significantly better than controlling the buffer layer. As discussed in section 1.3, the thickness of the buffer layer in outer units is $\mathcal{O}(80/Re_\tau)$, which becomes vanishingly small when the Reynolds number is large. The implication of this is that it is increasingly difficult to implement buffer-layer control strategies as the Reynolds number increases, because the absolute size of this region and the structures that reside there can become prohibitively small. In light of this, one key benefit of targeting the flow in the logarithmic layer is that the thickness of this region is fixed in outer units, and thus logarithmic-layer control strategies will not suffer from the same problems when the Reynolds number is large.

Chapter 6

Conclusions and outlook

This thesis has studied the effect of controlling separately the buffer and logarithmic layers in wall-bounded turbulent flows.

In the case of buffer-layer control, we have analysed the effect on turbulence of imposing different apparent virtual origins on the three velocity components, as some small-textured surfaces do. Examples of such surfaces are passive flow-control technologies, such as riblets, superhydrophobic surfaces or anisotropic permeable substrates. Following [Gómez-de-Segura and García-Mayoral \(2020\)](#), we conduct direct simulations of turbulent channels, and impose different virtual origins on the the three velocity components using Robin, slip-like boundary conditions. Our results demonstrate that, as long as the imposed virtual origins remain relatively small compared to the characteristic length scales of the near-wall turbulence cycle, the shift in the mean velocity profile, ΔU^+ , is determined by the offset between the virtual origin experienced by the mean flow and the virtual origin experienced by turbulence, i.e. $\Delta U^+ = \ell_V^+ - \ell_T^+$. The friction velocity that provides the scaling for the flow would not necessarily be the one derived directly from the surface drag, but from the total stress at the virtual origin for turbulence, $y = -\ell_T$. In practice, however, the difference between the two is negligible. In cases where the imposed virtual origins are no deeper than approximately 5 wall units, the turbulence remains essentially smooth-wall-like, other than for a wall-normal shift by ℓ_T^+ . This verifies the original idea proposed by ([Luchini, 1996](#)) that the dynamics of turbulence would be displaced ‘rigidly’ by the texture, and therefore would be unaltered compared to the flow over smooth wall.

We argue that it is possible to predict the virtual origin for turbulence a priori, and that it lies between the virtual origins for the spanwise and wall-normal velocities. This is expressed by equation (3.6), which shows that the only relevant parameters for determining the origin for turbulence are the relative positions of the virtual origins of u and w relative to the plane where v appears to vanish. This is an extension to the original theory proposed by [Luchini et al. \(1991\)](#) where, rather than on the difference between the virtual origins perceived by the tangential velocities, ΔU^+ depends on their positions relative to that perceived by the wall-normal velocity, regardless of the plane taken as reference. We also demonstrate that this

origin-offset effect is independent of Re_τ , when the virtual origins are fixed in wall units. In our simulations, the virtual origin perceived by the streamwise velocity is essentially set by the streamwise slip length, $y = -\ell_x$. We have set this independently for the mean flow and the fluctuations, verifying that the one affecting ΔU^+ is the origin for the mean flow. The virtual origin perceived by the streamwise velocity fluctuations, which are a proxy for the near-wall streaks, appears to be essentially inactive in setting the origin for turbulence, and hence has a negligible effect on the drag, at least in the regime where the origin perceived by the streaks is deeper than the origin perceived by the turbulence.

In the opposite regime, the region occupied by the streaks eventually becomes too confined, and the near-wall turbulence no longer remains smooth-wall-like. Our results indicate that this occurs when the origin perceived by turbulence is more than 2 wall units deeper than the origin perceived by the streaks, i.e. $\ell_T^+ \lesssim \ell_u^+ + 2$. We have also discussed the eventual breakdown of the virtual-origin framework in the regime of drag reduction, once the virtual origin for turbulence is deeper than 5 wall units below the reference plane, i.e. $\ell_T^+ \gtrsim 5$. Beyond this point, we observe that the quasi-streamwise vortices of the near-wall turbulence cycle approach the reference plane $y^+ = 0$ to such an extent that they are, in fact, ingested by the domain boundary, and the whole near-wall cycle is then fundamentally disrupted, changing the nature of the flow near the wall. An important point regarding the theoretical limits of the virtual-origin framework just described is that real textured surfaces exhibit failure mechanisms that can occur before $\ell_T^+ \approx 5$. For instance, the onset of the Kelvin–Helmholtz-like instability in riblets can occur for $\ell_T^+ \gtrsim 1$ (García-Mayoral and Jiménez, 2011b). In this case, the limits imposed by the operating window of the real surface are the most restrictive, and not the theoretical limits of the virtual-origin framework.

Within the limits set by the above restrictions, it is possible to predict the shift in the mean velocity profile for a given textured surface using equations (3.1) and (3.6). These equations are valid for surfaces of small texture size, which do not alter the canonical nature of the turbulence, and we show that this result can also be predicted by introducing a virtual origin for turbulence into an a priori, eddy-viscosity model for the Reynolds shear stress. We also present exploratory results that suggest that the effect on the flow of opposition control, an active flow-control technique, can also be interpreted in terms of virtual origins.

As mentioned above, while the motivation behind this aspect of the thesis was the observation that some textures produce such a virtual-origin effect, it was beyond our scope to quantify this effect for specific textures. However, some preliminary work on this can be found in Gómez-de-Segura et al. (2018b), who discuss methods for obtaining the slip lengths, and thus virtual origins, from DNS results of various textured surfaces a posteriori. In the future, it would be interesting to study the connection between real surfaces and the apparent virtual origins they would impose on the overlying flow in more detail, and even develop methods for predicting those virtual origins a priori. The present virtual-origin framework could then provide a predictive tool for analysing the effect of small-textured surfaces on the overlying

flow, without the need to conduct texture-resolving simulations or experiments.

In the second part of this thesis, we have investigated the effect of controlling the flow within the logarithmic layer alone, without directly modifying the flow elsewhere, and assessed how this effect varies with Reynolds number. This is motivated by the idea that the drag reduction generated by buffer-layer control strategies, such as the use of surface texturing, typically degrades logarithmically with increasing Reynolds number (Spalart and McLean, 2011; García-Mayoral et al., 2019). Since the size of the eddies in the logarithmic layer is known to scale essentially with distance from the wall, by controlling them it might be possible to produce a reduction in drag that does not degrade with increasing Reynolds number.

First, we considered the effect of an idealised, hypothetical control strategy that is able to remove all of the Reynolds shear stress in all or part of the logarithmic layer, while leaving the rest of the flow unaltered. The idea is that this would serve as a theoretical prediction for the maximum turbulent drag reduction achievable by strategies that target the logarithmic layer alone. Starting from the integral mean streamwise momentum equation for fully-developed channel flow (4.1), we derived an expression for the outward shift in the mean velocity profile at the channel centre, ΔU_p^+ , in this case, as encapsulated by (4.8).

In general, ΔU_p^+ depends on the friction Reynolds number Re_τ and the minimum and maximum heights of the control region, y_{min} and y_{max} . We have analysed the behaviour of ΔU_p^+ with Re_τ for three choices of y_{min} and y_{max} : (1) when the whole logarithmic layer is controlled; (2) when a fixed region of the logarithmic layer in outer units is controlled; (3) when a fixed region of the logarithmic layer in inner units is controlled. Our results show that when either the whole logarithmic layer or a fixed region of it in outer units is controlled, ΔU_p^+ increases essentially linearly with Re_τ , when Re_τ is large. Defining $U_{\delta_0}^+$ as the centreline velocity of the uncontrolled reference case, we discussed the relationship between the ratio $\Delta U_p^+/U_{\delta_0}^+$ and the drag reduction DR , given by (4.13). In these first two cases, we showed that $\Delta U_p^+/U_{\delta_0}^+$ also increased essentially linearly with Re_τ . This suggests that the drag reduction would improve with Re_τ when the whole logarithmic layer or a fixed region of it in outer units is controlled. On the other hand, when a fixed region of the logarithmic layer in inner units is controlled, we observe that ΔU^+ becomes essentially constant with Re_τ , in the limit of large Re_τ . As a result, $\Delta U_p^+/U_{\delta_0}^+$, and thus DR , degrade with increasing Re_τ , akin to the behaviour observed for control strategies that target the buffer layer.

We noted that the values of ΔU^+ and $\Delta U_p^+/U_{\delta_0}^+$ predicted by this idealised control strategy are extremely large and are not physically realistic, particularly when the whole logarithmic layer or a fixed part of it in outer units is controlled. However, as mentioned above, these predictions can be thought of as the optimum that any logarithmic-layer control strategy could achieve, and thus provide an upper bound for the potential performance of real control strategies. We conclude, therefore, that logarithmic-layer control strategies have significant potential, in terms of generating a large reduction in drag. Further, if the whole logarithmic layer or a fixed

part of it in outer units is controlled, our results suggest that it might be possible to generate a reduction in drag that improves with Re_τ .

In the final part of this thesis, we presented the results of a series of direct numerical simulations of turbulent channels at friction Reynolds numbers in the range $360 \leq Re_\tau \leq 2000$, and investigated the effect of controlling the flow in the logarithmic layer alone. The general idea of these simulations is to target the self-similar, wall-attached sweep and ejection motions and their associated vortex clusters that reside in the logarithmic layer (del Álamo et al., 2006; Lozano-Durán et al., 2012). This was done by artificially removing certain streamwise and spanwise length scales from the wall-normal velocity v across a range of heights, primarily within the logarithmic region. We refer to the removed scales as the target length scales, and the heights over which they are removed as the forcing region. The idea is that the contribution to uv for the target length scales will be zero, with the objective of disrupting the sweep and ejection motions discussed above.

Our simulations demonstrate that it is possible to control the flow in the logarithmic layer without affecting significantly the near-wall turbulence dynamics. In all cases we observe a positive, outward shift of the mean velocity profile, ΔU^+ , above the height at which the length scales are removed. This can be explained by the balance of viscous and Reynolds shear stress in these controlled flows, compared to the uncontrolled reference case. In the vicinity of the forcing region, there is a small, but significant deficit in the Reynolds shear stress, $\overline{u'v'}^+$, compared to the uncontrolled reference case, which results in a local increase in viscous stress, dU^+/dy^+ , and thus there is a sudden relative increase in U^+ . However, far enough above the forcing region, the viscous and Reynolds shear stresses recover to uncontrolled values, as do the turbulent fluctuations. In this sense, the turbulence far from the wall is essentially unmodified except for this additional mean velocity, and eventually recovers outer-layer similarity (Townsend, 1976).

We compare results of our simulations with theoretical predictions from the idealised control strategy discussed above. We find that the values of ΔU^+ and $\Delta U_p^+/U_{\delta_0}^+$ in the simulations are an order of magnitude smaller than those of predicted by the theory. The reason for this is that the actual proportion of the total Reynolds shear stress removed in the simulations is also typically an order of magnitude smaller than the proportion contained in the target length scales in the uncontrolled flow. This suggests that the flow in the logarithmic layer is very robust, even to this kind of targeted and intrusive control strategy. We show that it is possible to account for the effect of the hierarchical-forcing simulations using the theoretical predictions of the idealised control strategy, albeit only a posteriori. Since the idealised control strategy assumed that the flow outside the control region is left unaltered, this further suggests that the flow is left essentially unmodified far enough outside the forcing region.

By analysing the distribution of energy among length scales of uv , we demonstrate that the majority of the energy originally contained in the target length scales is redistributed to length scales of the order of the channel half height or longer. We postulate that energy is redistributed to these scales because they are the active scales of large eddies that reach well into the outer

region of the flow, and any energy that is redistributed to the very small scales would quickly be removed through viscous dissipation. However, this requires further investigation, particularly because some of this redistributed energy is contained in streamwise scales with streamwise wavenumber $k_x = 0$, i.e. streamwise wavelength $\lambda_x = \infty$. In hindsight, this is an artefact of the relatively short computational domains in our simulations, $L_x/\delta \times L_z/\delta = 2\pi \times \pi$. In the future, to further investigate the change in dynamics of the large scales within the forcing region, it would be necessary to conduct simulations in domains that are larger in the streamwise direction.

We also analysed the effect of Re_τ on the control in our simulations. The most promising results, in terms of drag reduction, came from the simulations in which a specific proportion of the uncontrolled Reynolds shear stress was targeted across the whole logarithmic layer. In these cases, we observed that ΔU^+ and $\Delta U^+/U_{\delta_0}^+$ grow with Re_τ , and our results suggest that both quantities will continue to grow with further increases in Reynolds number beyond $Re_\tau = 2000$. When 30% of the uncontrolled Reynolds shear stress was targeted, we found that $\Delta U^+ \approx 3$ for $Re_\tau = 2000$, which corresponds to a drag reduction $DR \approx 20\%$. However, we noted that these values of ΔU^+ are also achievable by small-scale surface texture, such as anisotropic permeable substrates (see e.g. [Gómez-de-Segura and García-Mayoral, 2019](#)). Our results suggests, therefore, that even though controlling the logarithmic layer has significant potential in terms of drag reduction, actual performance may be limited and may not be significantly better than controlling the buffer layer alone.

References

- Abbassi, M. R., Baars, W. J., Hutchins, N., and Marusic, I. (2017). Skin-friction drag reduction in a high-Reynolds-number turbulent boundary layer via real-time control of large-scale structures. *Int. J. Heat Fluid Flow*, 67:30–41.
- Abderrahaman-Elena, N., Fairhall, C. T., and García-Mayoral, R. (2019). Modulation of near-wall turbulence in the transitionally rough regime. *J. Fluid Mech.*, 865:1042–1071.
- Adrian, R. J., Meinhart, C. D., and Tomkinds, C. D. (2000). Vortex organization in the outer region of the turbulent boundary layer. *J. Fluid Mech.*, 422:1–54.
- del Álamo, J. C., Jiménez, J., Zandonade, P., and Moser, R. D. (2006). Self-similar vortex clusters in the turbulent logarithmic region. *J. Fluid Mech.*, 561:329–358.
- Baars, W. J., Hutchins, N., and Marusic, I. (2017). Self-similarity of wall-attached turbulence in boundary layers. *J. Fluid Mech.*, 823:R2.
- Baidya, R., Philip, J., Hutchins, N., Monty, J. P., and Marusic, I. (2017). Distance-from-the-wall scaling of turbulent motions in wall-bounded flows. *Phys. Fluids*, 29:020712.
- Baidya, R., Philip, J., Hutchins, N., Monty, J. P., and Marusic, I. (2021). Spanwise velocity statistics in high-Reynolds-number turbulent boundary layers. *J. Fluid Mech.*, 913:A35.
- Bechert, D. W. and Bartenwerfer, M. (1989). The viscous flow on surfaces with longitudinal ribs. *J. Fluid Mech.*, 206:105–129.
- Blackwelder, R. F. and Eckelmann, H. (1979). Streamwise vortices associated with the bursting phenomenon. *J. Fluid Mech.*, 94:577–594.
- Bottaro, A. (2019). Flow over natural or engineered surfaces: an adjoint homogenization perspective. *J. Fluid Mech.*, 877:P1.
- Bottaro, A. and Naqvi, S. B. (2020). Effective boundary conditions at a rough wall: a high-order homogenization approach. *Meccanica*, 55:1781–1800.
- Bradshaw, P. (1967). ‘Inactive’ motion and pressure fluctuations in turbulent boundary layers. *J. Fluid Mech.*, 30:241–258.
- Busse, A. and Sandham, N. D. (2012). Influence of an anisotropic slip-length boundary condition on turbulent channel flow. *Phys. Fluids*, 24:055111.
- Cantwell, B. J. (1981). Organized motion in turbulent flow. *Annu. Rev. Fluid Mech.*, 13:457–515.
- Chernyshenko, S. and Zhang, C. (2019). Effect of large-scale motions on skin friction reduction from the viewpoint of the QSQH theory. In *European Drag Reduction and Flow Control Meeting (EDRFCM 2019)*, Bad Herrenalb, Germany.

- Choi, H., Moin, P., and Kim, J. (1993). Direct numerical simulation of turbulent flow over riblets. *J. Fluid Mech.*, 255:503–539.
- Choi, H., Moin, P., and Kim, J. (1994). Active turbulence control for drag reduction in wall-bounded flows. *J. Fluid Mech.*, 262:75–110.
- Chu, D. C. and Karniadakis, G. E. (1993). A direct numerical simulation of laminar and turbulent flow over riblet-mounted surfaces. *J. Fluid Mech.*, 250:1–42.
- Chung, D., Chan, L., MacDonald, M., Hutchins, N., and Ooi, A. (2015). A fast direct numerical simulation method for characterising hydraulic roughness. *J. Fluid Mech.*, 773:418–431.
- Clauser, F. H. (1956). The turbulent boundary layer. *Adv. Appl. Mech.*, 4:1–51.
- Davidson, P. A. and Krogstad, P.-Å. (2009). A simple model for the streamwise fluctuations in the log-law region of a boundary layer. *Phys. Fluids*, 21:055105.
- Davidson, P. A., Nickels, T. B., and Krogstad, P.-Å. (2006). The logarithmic structure function law in wall-layer turbulence. *J. Fluid Mech.*, 550:51–60.
- van Driest, E. R. (1956). On turbulent flow near a wall. *J. Aero. Sci.*, 23:1007–1011.
- El-Samni, O. A., Chun, H. H., and Yoon, H. S. (2007). Drag reduction of turbulent flow over thin rectangular riblets. *Int. J. Eng. Sci.*, 45:436–454.
- Encinar, M. P., García-Mayoral, R., and Jiménez, J. (2014). Scaling of velocity fluctuations in off-wall boundary conditions for turbulent flows. *J. Phys.: Conf. Ser.*, 506:012002.
- Fairhall, C. T., Abderrahaman-Elena, N., and García-Mayoral, R. (2019). The effect of slip and surface texture on turbulence over superhydrophobic surfaces. *J. Fluid Mech.*, 861:88–118.
- Fairhall, C. T. and García-Mayoral, R. (2018). Spectral analysis of the slip-length model for turbulence over textured superhydrophobic surfaces. *Flow Turbul. Combust.*, 100:961–978.
- Flores, O. and Jiménez, J. (2010). Hierarchy of minimal flow units in the logarithmic layer. *Phys. Fluids*, 22:071704.
- Fukagata, K., Kasagi, N., and Koumoutsakos, P. (2006). A theoretical prediction of friction drag reduction in turbulent flow by superhydrophobic surfaces. *Phys. Fluids*, 18:051703.
- García-Mayoral, R., Gómez-de-Segura, G., and Fairhall, C. T. (2019). The control of near-wall turbulence through surface texturing. *Fluid Dyn. Res.*, 51:011410.
- García-Mayoral, R. and Jiménez, J. (2011a). Drag reduction by riblets. *Phil. Trans. R. Soc. A*, 369:1412–1427.
- García-Mayoral, R. and Jiménez, J. (2011b). Hydrodynamic stability and breakdown of the viscous regime over riblets. *J. Fluid Mech.*, 678:317–347.
- Gatti, D. and Quadrio, M. (2016). Reynolds-number dependence of turbulent skin-friction drag reduction induced by spanwise forcing. *J. Fluid Mech.*, 802:553–582.
- de Giovanetti, M., Hwang, Y., and Choi, H. (2016). Skin-friction generation by attached eddies in turbulent channel flow. *J. Fluid Mech.*, 808:511–538.
- Gómez-de-Segura, G. (2019). *Turbulent drag reduction by anisotropic permeable substrates*. PhD thesis, Department of Engineering, University of Cambridge.

- Gómez-de-Segura, G., Fairhall, C. T., MacDonald, M., Chung, D., and García-Mayoral, R. (2018a). Manipulation of near-wall turbulence by surface slip and permeability. *J. Phys.: Conf. Ser.*, 1001:012011.
- Gómez-de-Segura, G. and García-Mayoral, R. (2019). Turbulent drag reduction by anisotropic permeable substrates – analysis and direct numerical simulations. *J. Fluid Mech.*, 875:124–172.
- Gómez-de-Segura, G. and García-Mayoral, R. (2020). Imposing virtual origins on the velocity components in direct numerical simulations. *Int. J. Heat Fluid Flow*, 86:108675.
- Gómez-de-Segura, G., Sharma, A., and García-Mayoral, R. (2018b). Virtual origins in turbulent flows over complex surfaces. In *Proceedings of the 2018 Summer Program*, pages 277–286. Centre for Turbulence Research, Stanford University.
- Guseva, A., Encinar, M., and Jiménez, J. (2019). Active flow control of the logarithmic layer. In *Proc. Div. Fluid Dyn.*, page B26.4. American Physical Society.
- Hamilton, J. M., Kim, J., and Waleffe, F. (1995). Regeneration mechanisms of near-wall turbulence structures. *J. Fluid Mech.*, 287:317–348.
- Hammond, E. P., Bewley, T. R., and Moin, P. (1998). Observed mechanisms for turbulence attenuation and enhancement in opposition-controlled wall-bounded flows. *Phys. Fluids*, 10:2421.
- Hoyas, S. and Jiménez, J. (2006). Scaling of the velocity fluctuations in turbulent channels up to $Re_\tau = 2003$. *Phys. Fluids*, 18:011702.
- Hutchins, N. (2015). Large-scale structures in wall-bounded turbulence: (implications to control strategies). In *Ninth International Symposium on Turbulence and Shear Flow Phenomena (TSFP-9)*, Melbourne, Australia.
- Hutchins, N. and Marusic, I. (2007). Large-scale influences in near-wall turbulence. *Phil. Trans. R. Soc. A*, 365:647–664.
- Hwang, Y. and Bengana, Y. (2016). Self-sustaining process of minimal attached eddies in turbulent channel flow. *J. Fluid Mech.*, 795:708–738.
- Ibrahim, J. I., Guseva, A., and García-Mayoral, R. (2020). Selective opposition-like control of large-scale structures in wall-bounded turbulence. *J. Phys.: Conf. Ser.*, 1522:012015.
- Ibrahim, J. I., de Segura, G. G., Chung, D., and García-Mayoral, R. (2021). The smooth-wall-like behaviour of turbulence over drag-altering surfaces: a unifying virtual-origin framework. *J. Fluid Mech.*, 915:A56.
- Jelly, T. O., Jung, S. Y., and Zaki, T. A. (2014). Turbulence and skin friction modification in channel flow with streamwise-aligned superhydrophobic surface texture. *Phys. Fluids*, 26:095102.
- Jeong, J., Hussain, F., Schoppa, W., and Kim, J. (1997). Coherent structures near the wall in a turbulent channel flow. *J. Fluid Mech.*, 332:185–214.
- Jiménez, J. (1994). On the structure and control of near wall turbulence. *Phys. Fluids*, 6:944.
- Jiménez, J. (2004). Turbulent flows over rough walls. *Annu. Rev. Fluid Mech.*, 36:173–196.
- Jiménez, J. (2012). Cascades in wall-bounded turbulence. *Annu. Rev. Fluid Mech.*, 44:27–45.

- Jiménez, J. (2013). Near-wall turbulence. *Phys. Fluids*, 25:101302.
- Jiménez, J. (2018). Coherent structures in wall-bounded turbulence javier. *J. Fluid Mech.*, 842:P1.
- Jiménez, J. and Moin, P. (1991). Minimal flow unit in near-wall turbulence. *J. Fluid Mech.*, 225:213–240.
- Jiménez, J. and Pinelli, A. (1999). The autonomous cycle of near-wall turbulence. *J. Fluid Mech.*, 389:335–359.
- Kamrin, K., Bazant, M. Z., and Stone, H. A. (2010). Effective slip boundary conditions for arbitrary periodic surfaces: the surface mobility tensor. *J. Fluid Mech.*, 658:409–437.
- Kim, H. T., Kline, S. J., and Reynolds, W. C. (1971). The production of turbulence near a smooth wall in a turbulent boundary layer. *J. Fluid Mech.*, 50:133–160.
- Kim, J. and Moin, P. (1985). Application of a fractional-step method to incompressible Navier-Stokes equations. *J. Comput. Phys.*, 59:308–323.
- Kim, J., Moin, P., and Moser, R. (1987). Turbulence statistics in fully developed channel flow at low Reynolds number. *J. Fluid Mech.*, 177:133–166.
- Kline, S. J., Reynolds, W. C., Schraub, F. A., and Runstadler, P. W. (1967). The structure of turbulent boundary layers. *J. Fluid Mech.*, 30:741–773.
- Kwon, Y. and Jiménez, J. (2021). An isolated logarithmic layer. *J. Fluid Mech.*, 916:A13.
- Lācis, U. and Bagheri, S. (2017). A framework for computing effective boundary conditions at the interface between free fluid and a porous medium. *J. Fluid Mech.*, 812:866–889.
- Lācis, U., Sudhakar, Y., Pasche, S., and Bagheri, S. (2020). Transfer of mass and momentum at rough and porous surfaces. *J. Fluid Mech.*, 884:A21.
- Lauga, E. and Stone, H. A. (2003). Effective slip in pressure-driven stokes flow. *J. Fluid Mech.*, 489:55–77.
- Le, H. and Moin, P. (1991). An improvement of fractional-step methods for the incompressible Navier-Stokes equations. *J. Comput. Phys.*, 92:369–379.
- Lee, M. and Moser, R. D. (2015). Direct numerical simulation of turbulent channel flow up to $Re_\tau \approx 5200$. *J. Fluid Mech.*, 774:395–415.
- Lozano-Durán, A. and Bae, H. J. (2019). Cracteristic scales of townsend’s wall-attached eddies. *J. Fluid Mech.*, 868:698–725.
- Lozano-Durán, A., Flores, O., and Jiménez, J. (2012). The three-dimensional structure of momentum transfer in turbulent channels. *J. Fluid Mech.*, 694:100–130.
- Lozano-Durán, A. and Jiménez, J. (2014). Effect of the computational domain on direct simulations of turbulent channels up to $Re_\tau = 4200$. *Phys. Fluids*, 26:011702.
- Luchini, P. (1995). Asymptotic analysis of laminar boundary-layer flow over finely grooved surfaces. *Eur. J. Mech. B/Fluids*, 14:169–195.
- Luchini, P. (1996). Reducing the turbulent skin friction. In *Computational Methods in Applied Sciences '96*, pages 466–470. John Wiley & Sons Ltd.

- Luchini, P. (2013). Linearized no-slip boundary conditions at a rough surface. *J. Fluid Mech.*, 737:349–367.
- Luchini, P., Manzo, F., and Pozzi, A. (1991). Resistance of a grooved surface to parallel flow and cross-flow. *J. Fluid Mech.*, 228:87–109.
- MacDonald, M., Chan, L., Chung, D., Hutchins, N., and A. Ooi, A. (2016). Turbulent flow over transitionally rough surfaces with varying roughness densities. *J. Fluid Mech.*, 804:130–161.
- Marusic, I., Mathis, R., and Hutchins, N. (2010). High Reynolds number effects in wall turbulence. *Int. J. Heat Fluid Flow*, 31:418–428.
- Marusic, I. and Monty, J. P. (2019). Attached eddy model of wall turbulence. *Annu. Rev. Fluid Mech.*, 51:49–74.
- Mathis, R., Hutchins, N., and Marusic, I. (2009). Large-scale amplitude modulation of the small-scale structures in turbulent boundary layers. *J. Fluid Mech.*, 628:311–337.
- McKeon, B. J. (2019). Self-similar hierarchies and attached eddies. *Phys. Rev. Fluids*, 4:082601.
- Min, T. and Kim, J. (2004). Effects of hydrophobic surface on skin-friction drag. *Phys. Fluids*, 16:L55.
- Mizuno, Y. and Jiménez, J. (2013). Wall turbulence without walls. *J. Fluid Mech.*, 723:429–455.
- Moser, R. D., Kim, J., and Mansour, N. N. (1999). Direct numerical simulation of turbulent channel flow up to $Re_\tau = 590$. *Phys. Fluids*, 11:943.
- Orlandi, P. and Jiménez, J. (1994). On the generation of turbulent wall friction. *Phys. Fluids*, 6:634.
- Park, H., Park, H., and Kim, J. (2013). A numerical study of the effects of superhydrophobic surface on skin-friction drag in turbulent channel flow. *Phys. Fluids*, 25:110815.
- Perot, J. B. (1993). An analysis of the fractional step method. *J. Comput. Phys.*, 108:51–58.
- Perry, A. E. and Chong, M. S. (1982). On the mechanism of wall turbulence. *J. Fluid Mech.*, 119:173–219.
- Pope, S. B. (2000). *Turbulent Flows*. Cambridge University Press.
- Reynolds, W. C. and Tiederman, W. G. (1967). Stability of turbulent channel flow, with application to Malkus’s theory. *J. Fluid Mech.*, 27:253–272.
- Robinson, S. K. (1991). Coherent motions in the turbulent boundary layer. *Annu. Rev. Fluid Mech.*, 23:601–639.
- Rothstein, J. P. (2010). Slip on superhydrophobic surfaces. *Annu. Rev. Fluid Mech.*, 42:89–109.
- Ruan, Z., Baars, J., Abbassi, M. R., Hutchins, N., and Marusic, I. (2018). Active control of large-scales in a high-Reynolds-number turbulent boundary layer. In *Proc. 21st Australasian Fluid Mech. Conf., AFMC 2018*, Adelaide, Australia.
- Ruan, Z., de Silva, C., Marusic, I., and Hutchins, N. (2019). Active control of large-scale structures in turbulent boundary layers using wall-normal jets. In *Proc. Div. Fluid Dyn.*, page L26.4. American Physical Society.

- Schoppa, W. and Hussain, F. (2002). Coherent structure generation in near-wall turbulence. *J. Fluid Mech.*, 453:57–108.
- Seo, J., García-Mayoral, R., and Mani, A. (2018). Turbulent flows over superhydrophobic surfaces: Flow-induced capillary waves, and robustness of air-water interfaces. *J. Fluid Mech.*, 835:45–85.
- Seo, J. and Mani, A. (2016). On the scaling of the slip velocity in turbulent flows over superhydrophobic surfaces. *Phys. Fluids*, 28:025110.
- Sillero, J. A., Jiménez, J., and Moser, R. D. (2013). One-point statistics for turbulent wall-bounded flows at Reynolds numbers up to $\delta^+ \approx 2000$. *Phys. Fluids*, 25:105102.
- Smith, C. R. and Metzler, S. P. M. (1983). The characteristics of low-speed streaks in the near-wall region of a turbulent boundary layer. *J. Fluid Mech.*, 129:27–54.
- Spalart, P. R. and McLean, J. D. (2011). Drag reduction: enticing turbulence, and then an industry. *Philos. Trans. Royal Soc. A*, 369:1556–1569.
- Theodorsen, T. (1952). Mechanism of turbulence. In *Proc. Second Midwestern Conf. on Fluid Mechanics*, pages 1–18, Ohio State University, Columbus, Ohio.
- Toedtli, S., Yu, C., and McKeon, B. (2020). On the origin of drag increase in varying-phase opposition control. *Int. J. Heat Fluid Flow*, 85:108651.
- Townsend, A. A. (1961). Equilibrium layers and wall turbulence. *J. Fluid Mech.*, 11(1):97–120.
- Townsend, A. A. (1976). *The Structure of Turbulent Shear Flow*. Cambridge University Press, second edition.
- Waleffe, F. (1997). On a self-sustaining process in shear flows. *Phys. Fluids*, 9:883.
- Walsh, M. J. and Lindemann, A. M. (1984). Optimization and application of riblets for turbulent drag reduction. *AIAA Paper* 84-0347.
- Yang, Q., Willis, A. P., and Hwang, Y. (2019). Exact coherent states of attached eddies in channel flow. *J. Fluid Mech.*, 862:1029–1059.
- Zhang, C. and Chernyshenko, S. I. (2016). Quasisteady quasihomogeneous description of the scale interactions in near-wall turbulence. *Phys. Rev. Fluids*, 1:014401.

Appendix A

Additional results

A.1 Results of Choi et al. (1994) interpreted in the virtual-origin framework

Here, we present a brief analysis of the opposition control simulations of Choi et al. (1994) within the virtual-origin framework of the present thesis. In that study, there are two cases of interest, one with opposition controlled applied to v and the other with opposition control applied to w . In both cases, the detection plane is $y_d^+ \approx 10$. In contrast, in our opposition control simulations presented in section 3.6, the detection plane was $y_d^+ = 7.8$. Figure A.1(a) shows the mean velocity profiles for the two controlled flows, compared with that of the uncontrolled case. Following the method of chapter 3, we find the shift ℓ_T^+ required to collapse the controlled mean velocity profiles with the uncontrolled one. The shifted and rescaled profiles are shown in figure A.1(b). In these cases the virtual origin perceived by the mean flow is at $y^+ = 0$, and so $\Delta_{\bar{U}}^- - \ell_T^+$, with $\ell_T^+ < 0$. We see that the shifted and rescaled mean profiles collapsed to the uncontrolled case, suggesting that the effect of the control can be reduced to a simple offset of the virtual origin perceived by turbulence with respect to the origin perceived by the mean flow. The measured values of ΔU^+ are included in table A.1, along with the predicted virtual origin for turbulence, assuming that the control establishes a virtual origin at $y^+ = y_d^+/2$ for the controlled velocities. As discussed at length in section 3.6, the predicted shift in the mean velocity profile, $\ell_U^+ - \ell_{T,pred}^+$, provides a reasonable estimate for the measured ΔU^+ in the case of v control, but not for the case of w . The reason for this discrepancy is discussed in detail in section 3.6.

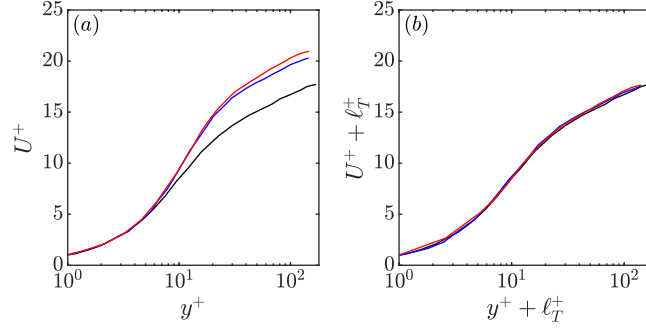


Figure A.1 Mean velocity profiles for simulations with opposition control on v and w from Choi et al. (1994). In these cases the sensing plane is at $y_d^+ \approx 10$. (a) scaled with the friction velocity at the reference plane, $y^+ = 0$; (b) shifted in y^+ by ℓ_T^+ and scaled with the friction velocity at the origin for turbulence, $y^+ = -\ell_T^+$. Note that in these cases, $\ell_T^+ < 0$ and therefore the origin for turbulence is above the plane $y^+ = 0$. Black lines, smooth-wall reference data; blue lines, v control; red lines w control.

| Case | $y_d^+/2$ | ℓ_U^+ | ℓ_w^+ | ℓ_v^+ | $\ell_{T,pred}^+$ | $\ell_U^+ - \ell_{T,pred}^+$ | ΔU^+ |
|-------------|-----------|------------|------------|------------|-------------------|------------------------------|--------------|
| v control | 5.0 | 0.0 | 0.0 | -5.0 | -2.5 | 2.5 | 3.0 |
| w control | 5.0 | 0.0 | -5.0 | 0.0 | -5.0 | 5.0 | 3.6 |

Table A.1 Analysis of opposition control simulations from Choi et al. (1994). For each case, the notional virtual origins are given with respect to the reference plane $y^+ = 0$, assuming that the control establishes a virtual origin for the opposed velocity components at $y^+ = y_d^+/2$, where y_d^+ is the detection plane height. The predicted virtual origin for turbulence, $\ell_{T,pred}^+$, is given, which is calculated from (3.6). The difference $\ell_U^+ - \ell_{T,pred}^+$ represents the predicted shift in the mean velocity profile, and ΔU^+ is the measured shift in the mean velocity profile from figure A.1.